The Petrology and Geochemistry of a Suite of Intrusive Igneous Rocks from the Southern Kermadec Arc-Havre Trough, SW Pacific

Brenton Rex Tozer

A thesis submitted to Victoria University of Wellington in partial fulfilment of the requirements of the degree of Master of Science in Geology

Victoria University of Wellington

School of Geography, Environment and Earth Science

Wellington, New Zealand

2021

Abstract

The study of intrusive igneous rocks can provide insights into deep crustal processes. In active intraoceanic arc environments, the opportunity to study of these intrusive igneous rocks usually comes from xenoliths entrained within eruptive products, as accessibility to *in situ* intrusive rocks is limited. This thesis documents a suite of the first intrusive samples dredged from the Havre Trough, which provide insights into deep magmatic processes in this intraoceanic back-arc system. The suite of ten intrusive igneous rocks were dredged from Basin E, a back-arc basin (BAB) in the Kermadec Arc-Havre Trough (KAHT) and consist of *in situ* gabbroic meso- to orthocumulates. Four representative samples were selected from the suite of ten on the basis of grainsize, and from them a petrogenetic model was built to determine the associations of the samples within the magmatic system of the region. The four samples all exhibit comparable mineral assemblages of plagioclase, clinopyroxene, and magnetite, with olivine and orthopyroxene absent. Texturally the samples appear to have formed in (a) magma chamber(s) where the minerals cooled slowly and formed relatively large, euhedral crystals that trapped interstitial melt between them. The interstitial melts crystallised forming more evolved intercumulus material (plagioclase + quartz ± amphibole ± apatite). Three of the four samples have coarser grainsizes (1-2 mm), and exhibit similar magnetite temperature estimates, indicating that they formed from similar melts. The other sample has a finer grainsize (<1 mm), and exhibits lower temperature estimates, indicating that this sample formed from a lower temperature, faster cooling melt. Plagioclase compositions follow a similar trend to plagioclase phenocrysts from modern back-arc volcanoes which indicates that these samples have an association with the modern magmatic system rather than the now extinct Miocene (Colville) Arc. Clinopyroxene trace element data are also consistent with these samples being associated with the modern subduction system. The magma chamber(s) that the samples formed in, comes from a mid-lower crustal depth, 3-6 km based on pressure estimates from amphibole crystal chemistry. The exposure of rocks from this depth would have been facilitated by normal faulting associated with rifting and opening of the Havre Trough. Petrologic and geochemical analyses of these cumulates suggest that the deep, back-arc basins consist of entirely new magmatic material formed from BAB volcanism, with no evidence for pre-existing crust.

Acknowledgments

My thesis is finally complete and after such an odd year in the world I owe a big thank you to everyone who helped support and guide me through the challenges of research.

Firstly, I owe a big thank you to all three of my supervisors. Thank you for all your assistance and support that allowed me to undertake this project. To my primary supervisor, Monica Handler, for all your help with discussing all aspects of the project and having the time to listen to my progress and helping me to stay on track throughout the year. Ian Schipper, for all your assistance with EPMA operation and analysis, and for looking over my ideas and providing feedback that helped clarify some ideas and processes. Sally Watson, for jumping on as a supervisor and providing valuable feedback into the mechanisms of the rifting. To my two previous supervisors before everything went weird, Richard Wysoczanski, for providing the samples and critical unpublished data, the welcoming visits to NIWA, and the valuable feedback on my abstract. Christian Timm, for your brief but insightfully couple of months being my supervisor and helping to get this project on the go.

NIWA is thanked for providing funding for this project.

My lab work and data collection would not have been nearly as successful without the expertise and assistance of Fiona Tuckett, who through trial and error and many attempts produced wonderful block mounts from some incredibly difficult samples and without whom I would not have anything to have done research on. Luisa Ashworth, a big thank you to your assistance and expertise on the LA-ICP-MS and data processing, and for not letting the machine get the best of you when it was misbehaving.

To my parents, Peter and Renee, thank you for all your support throughout my entire university career, whether it be providing meals and a warm place to stay when I visited home and in the final few months of writing this thesis. To my sister, Caitlin, for keeping me relatively sane in all of this and supporting me.

Finally, I want to thank all my friends I have made over the course of my studies. Thank you to my office buddies, Sam, Emily, and Josh, without the banter, laughs, and numerous cups of coffee I do not think I would have ever gotten through this thesis. To everyone in the Cotton office, thank you. To the Rodney Street Flat, thank you for making that place a second home for me and helping to make the lockdown that much more bearable.

Table of Contents

List of Figures

List of Tables

Chapter 1 Introduction

1.1 Introduction

Subduction zones are areas in which a cold, dense plate of oceanic lithosphere is transported into the mantle where it undergoes heating and other metamorphic changes that lead to a large-scale transferal of material between the Earth's surface and interior (e.g., Gamble et al., 1996, Gill, 1981). Subduction zone magmatism is represented by long linear or arcuate chains of arc-front volcanoes (Gill, 1981, Wilson, 1989). These volcanic arcs span some ~22,000 km around the planet and a majority are found along the convergent Pacific Plate margins (e.g., De Ronde et al., 2001, Leat and Larter, 2003, Timm et al., 2019). The study of magmatism at volcanic arcs and subduction zones is a critical part in furthering our understanding of element transfer and recycling among the crust, mantle, hydrosphere, and atmosphere (e.g., Haase et al., 2002, McCulloch and Gamble, 1991, Timm et al., 2016). Insights into modern arc magmatism typically come from the examination of the eruptive products of arc volcanoes as these products are more readily exposed on the surface/seafloor and are therefore more accessible. Plutonic samples, which represent deeper components of arc magmatism (e.g., Haraguchi et al., 2003, Kawate and Arima, 1998, Turnbull et al., 2010), are more difficult to access. Plutonic xenoliths included in eruptive products have provided insights into processes of magma mixing and evolution of the magmatic system over time or may represent portions of the lower crust or mantle that are usually inaccessible (Barker, 2010, Barker et al., 2013, Klaver et al., 2017, Timm et al., 2016). The study of plutonic rocks from oceanic arc settings, therefore, can help us to understand the overall evolution of the tectonomagmatic system but are sparsely sampled.

This thesis presents the first petrographic and geochemical data for a suite of plutonic rocks dredged from a back-arc basin of the modern Kermadec Arc-Havre Trough (KAHT) subduction system, to evaluate their petrogenesis and provide insights into magmatic processes occurring at depth.

1.2 Subduction Zones: An Overview

Subduction zones where oceanic lithosphere sinks into the mantle, are integral components of plate tectonics and are considered the primary driver of plate tectonics on Earth (e.g., Reagan et al., 2019). In addition, subduction zones form key regions where material is transferred and cycled between the mantle and the surface in probably one of the most important geochemical cycles on Earth (e.g., Haase et al., 2002, McCulloch and Gamble, 1991). A subduction zone has various components to its anatomy, shown schematically in Figure 1-1 and briefly described below.

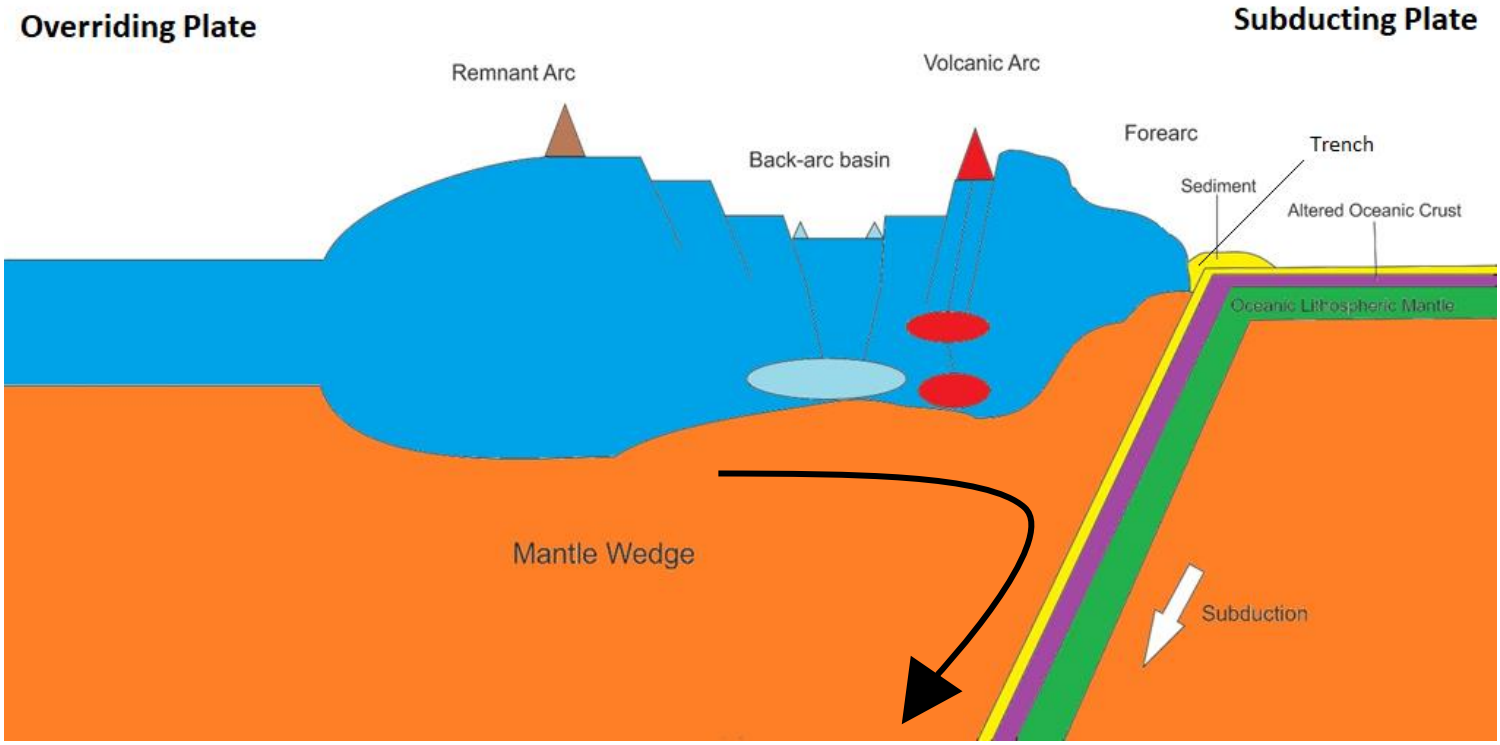

Figure 1-1: Schematic diagram of a subduction zone based on the southern Kermadec Arc-Havre Trough configuration. Not to scale. Black arrow indicates Mantle flow.

1.2.1 Anatomy of a Subduction Zone

The subducting plate or "slab" is composed of oceanic crust, formed at a mid-ocean ridge, and altered through hydrothermal and seawater interaction, oceanic sediment that has been deposited over the lifetime of the crust, and underlying oceanic lithospheric mantle. The overriding plate can be comprised of either continental or oceanic lithosphere

with each type forming different surficial expressions of volcanism, active continental margins and oceanic arcs, respectively (Wilson, 1989).

Both forms of surficial volcanism share major characteristics (Wilson, 1989):

1) Linear or arcuate chains of volcanoes that can reach lengths in the hundreds to thousands of kilometres but are narrow in width (200-300 km).
2) A deep ocean trench (6000- 11,000 m deep).
3) Active volcanism with an abrupt boundary to the volcanic zone, which is usually parallel to the trench.
4) A Wadati-Benioff zone marking the plane of subducting slab.
5) Volcanic association termed 'orogenic andesite' (Gill, 1981).

Although both types of volcanism share similarities there are key differences between the two. The most obvious being the thickness of the upper plate and a greater abundance of more silica-rich magmas in the continental setting (e.g., Gamble et al., 1990). Along with the greater proportion of felsic magmas, continental-margin volcanism typically has higher concentrations of K, Sr, Rb, Ba, Zr, Th and U, as well as a wider range of isotopic compositions, all of which can be explained by interactions between the continental crust and the ascending magmas (Wilson, 1989). The samples for this study come from the simpler oceanic arc setting where crustal interaction in the upper plate is more limited in its ability to modify magmas, the ascending magmas are less likely to be stalled in the upper crust and therefore less likely to undergo fractionation or melt the surrounding crustal rocks (e.g., Barker et al., 2013).

The fore arc is the region of the subduction zone between an oceanic trench and the volcanic arc. The fore-arc consists of the oceanic trench, accretionary wedge composed of sediment that has been scraped off the subducting slab and fore-arc sedimentary basin (Kearey et al., 2009, Wilson, 1989).

The region of the subduction zone located behind the active volcanic arc in an oceanic arc setting may include a back-arc basin. These back-arc basins are zones of crustal extension that range from rifting (e.g., Havre Trough, Wysoczanki et al., 2010) to sea floor spreading (e.g., Lau Basin, Ruellan et al., 2003).

Proposed driving mechanisms for the formation of back-arc basins can be grouped into three types (Heuret and Lallemand, 2005, Nakakuki and Mura, 2013):

1) Slab rollback driven by pressure from mantle flow or asthenosphere injection (e.g., Flower et al., 2001, Tatsumi et al., 1990).
2) Rollback of a gravitationally unstable slab (e.g., Garfunkel et al., 1986).
3) The overriding plate moving away from the trench with the deep mantle anchoring the slab (e.g., Uyeda and Kanamori, 1979).

Previous studies have suggested that deformation in the back-arc is influenced by the absolute motion of the overriding plate with respect to the trench and that this motion is what drives back-arc extension (Heuret and Lallemand, 2005). However, it has been shown that active back-arc basins are often accompanied by a fast retreating slab which suggests that slab rollback is a major driving mechanism of back-arc basin development with mantle flow exerting pressure on the slab surface from the arc side (Heuret and Lallemand, 2005, Nakakuki and Mura, 2013, Sdrolias and Müller, 2006).

A remnant arc, such as shown in the schematic based on the southern Kermadec Arc-Havre Trough (Figure 1-1) is represented by a ridge that is found behind the active arc front. These remnant arcs are formed from the rifting and opening of back-arc basins. As these basins widen, the remnant arc is left behind (Karig, 1972).

1.2.2 Magmatism in Oceanic Arc Settings

The generation of magma beneath an oceanic arc occurs as a result of partial melting in the mantle wedge after components that have been derived from the subducting slab hydrate and lower the solidus of the mantle peridotite (e.g., McCulloch and Gamble, 1991). The lowering of the solidus has an effect on the mineral formation that occurs in the magmas, the fluid released suppresses the formation of plagioclase until later in the sequence (Greene et al., 2006, Plank et al., 2004).

Aqueous fluids and silicate melts are regarded as the most important slab-derived components that drive partial melting and magma generation in oceanic arc settings. As the

slab descends to greater depths the release of these components initially form a layer of serpentinite, which then gets dragged further down, dehydrates, and releases the slab-derived components into the mantle wedge at depth (e.g., Wysoczanski et al., 2006). Arc magmas are characterised by enrichments in large ion lithophile elements (LILE), these elements are highly soluble in aqueous fluid and therefore indicate an enrichment of aqueous fluids in the mantle wedge, at relatively shallow depths (e.g., Brenan et al., 1998, Pearce and Stern, 2006). Arc magmas are also enriched in light rare earth elements (LREE) however these elements are less soluble in aqueous fluids so the enrichment in the magmas is interpreted to come from the addition of sediment derived silicate melt into the mantle wedge (e.g., Hawkesworth et al., 1997, Johnson and Plank, 2000). High field strength elements (HFSE) in sediments are found in mineral phases that are refractory at subduction settings beneath the arc front and are generally depleted in arc front magmas (Gill, 1981, Pearce and Stern, 2006).

1.3 Nomenclature

Consistent and appropriate classification schemes for igneous rocks and minerals help to prevent confusion and misinterpretation when comparing across different studies. Igneous rocks can be classified based on chemistry, modal mineralogy, and texture. In this section the terms and nomenclature used throughout this study are defined.

1.3.1 Mineralogical Classification

The samples in the study are plutonic rocks with phaneritic textures, meaning the mineral grains are large enough to be visible to the naked eye, and can therefore be classified based upon modal mineral assemblages (Streckeisen, 1976). The classification of Streckeisen (1976) is primarily based on the proportion of mafic minerals to felsic minerals, normalised to 100%. The proportion of mafic minerals, which includes olivine, pyroxene, amphibole, mica, opaque minerals, apatite, and other accessory minerals, is referred to as the ‘M’ content. If the M content is <90% then the rocks are classified based on the

proportion of the felsic minerals (Figure 1-2). This classification is dependent on their Q (quartz), A (alkali feldspar), P (plagioclase), and F (feldspathoid/foid) component.

The most abundant mineral phases in the samples are feldspar, pyroxene, and Fe-Ti oxides. These minerals are furthered classified based on relative proportions of major element endmember components.

Feldspars are classified based on the relative proportions of their endmember components on a ternary diagram (Figure 1-3):

- Anorthite (An) is the calcium endmember of feldspar.
- Albite (Ab) is the sodium endmember of feldspar.
- Orthoclase (Or) is the potassium endmember of feldspar.

Ca-Mg-Fe pyroxenes are classified on a quadrilateral (Figure 1-4) based on the relative proportions of the endmember components:

- Wollastonite (Wo) is the calcium component.
- Enstatite (En) is the magnesium component.
- Ferrosilite (Fs) is the iron component.

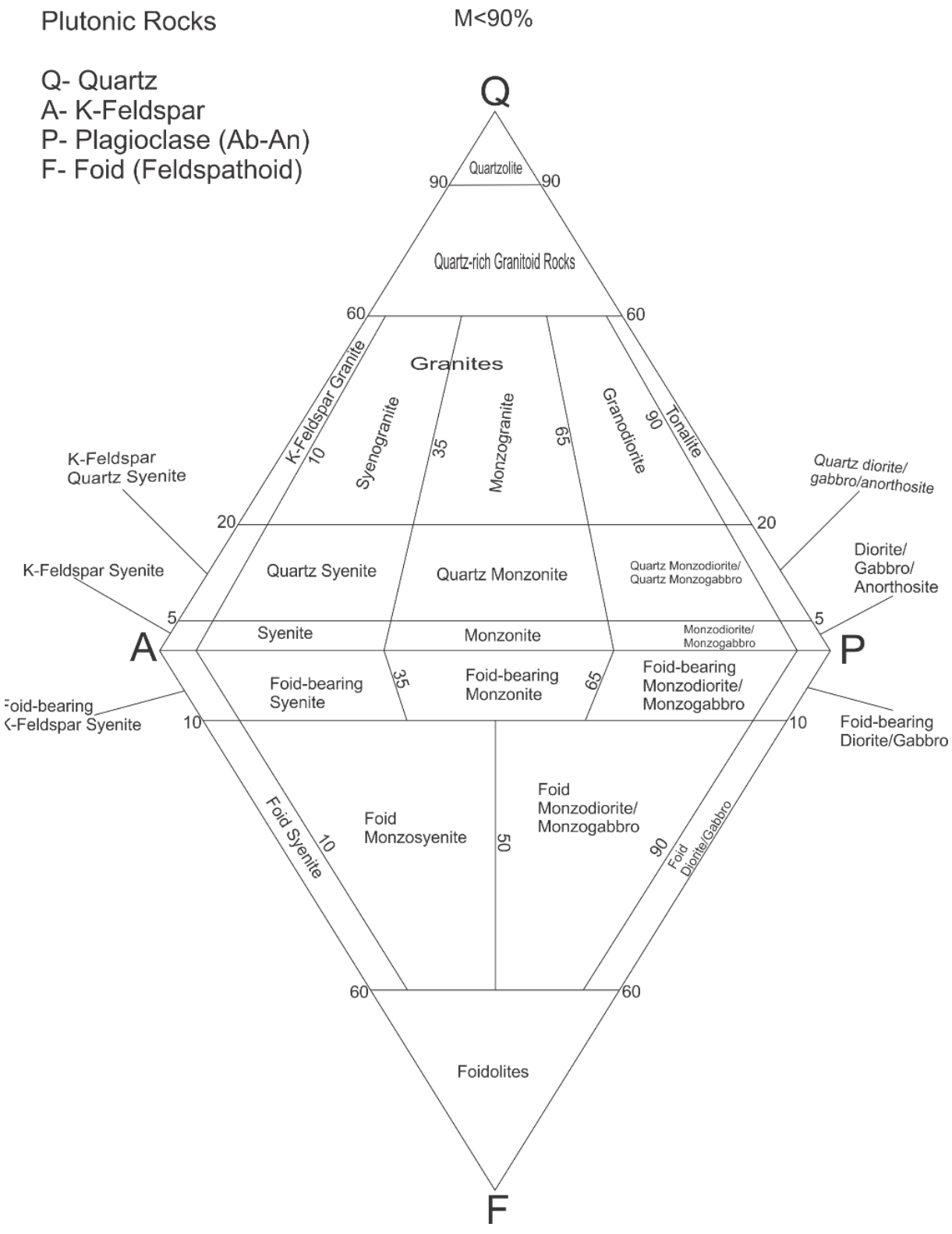

Figure 1-2: QAPF diagram for classification of igneous rocks with mafic minerals <90%. Modified from Streckeisen (1976).

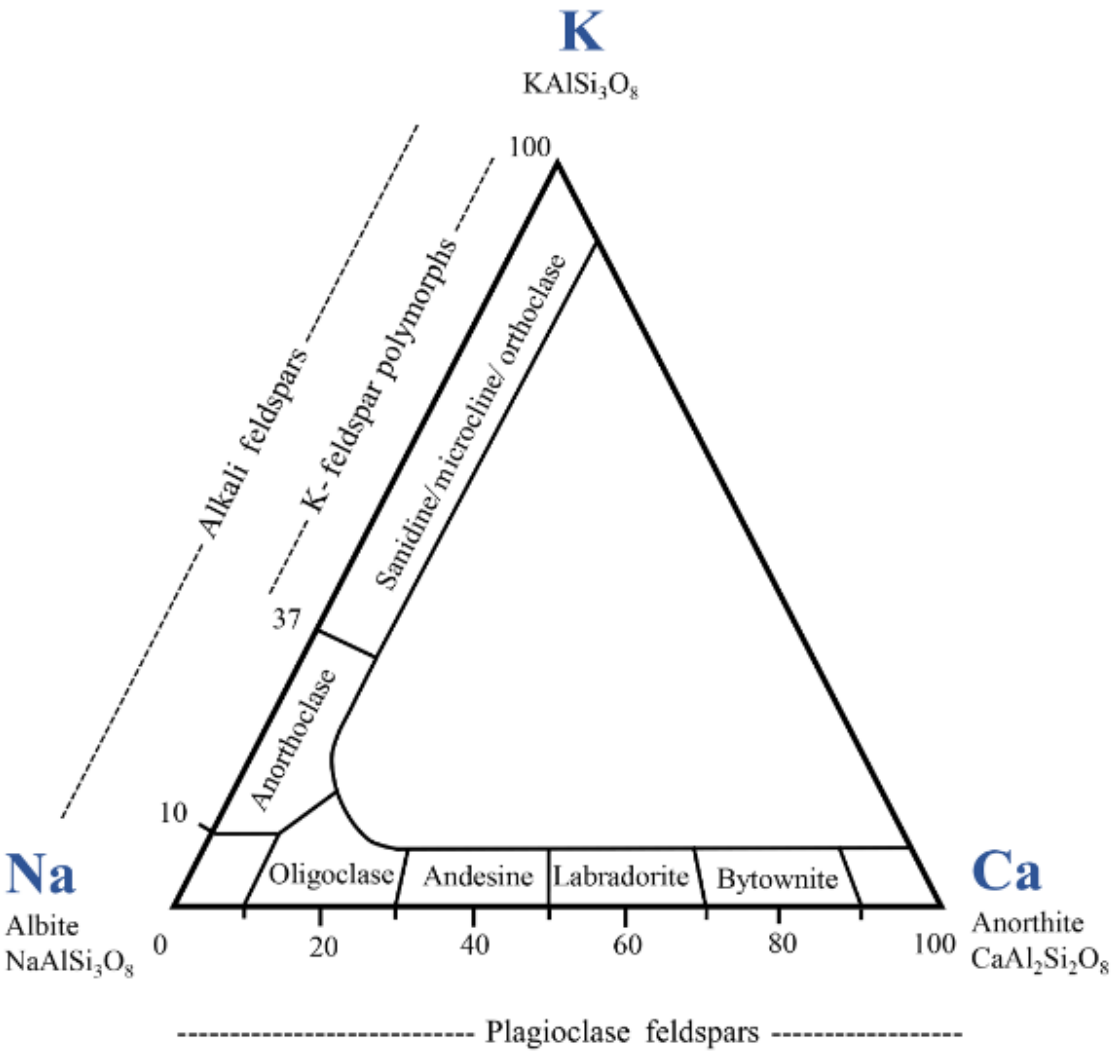

Figure 1-3: Feldspar classification ternary diagram.
Adapted from Kumar et al., (2019).

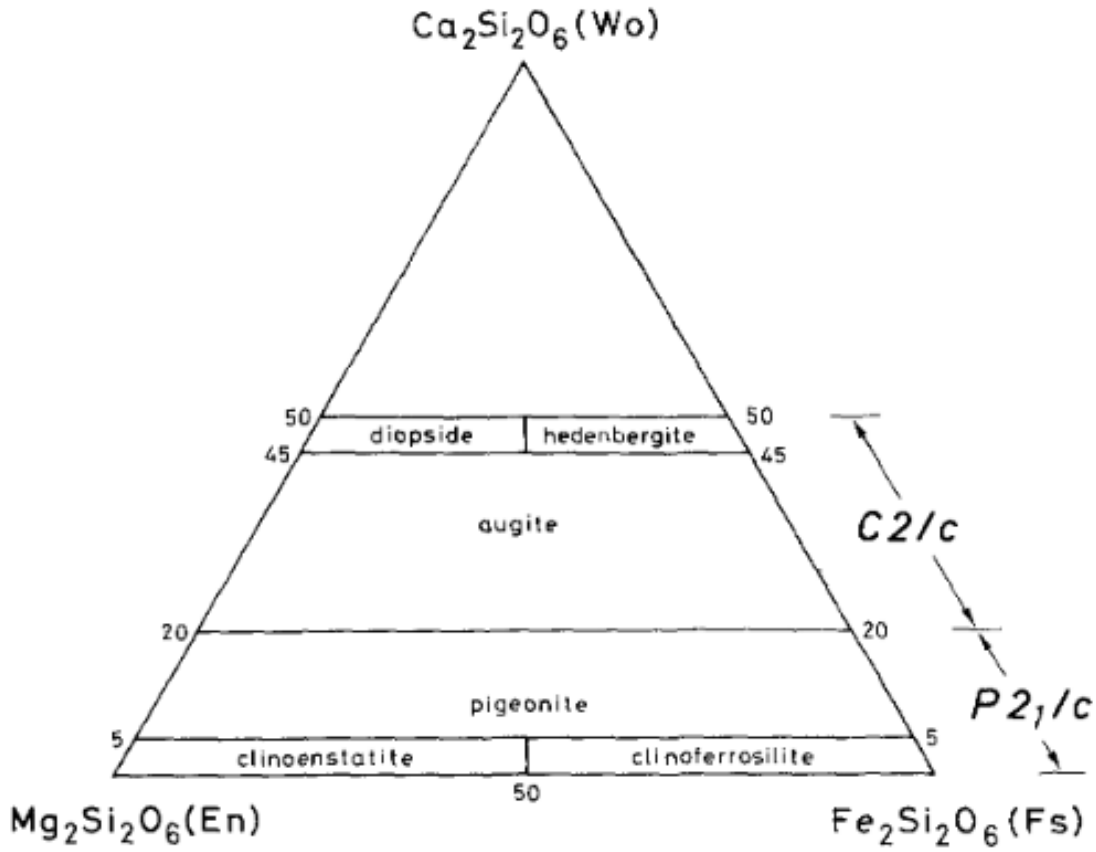

Figure 1-4: Ca-Mg-Fe pyroxene classification diagram. Adapted from Morimoto (1988)

1.3.2 Cumulate Textures

The textures present within the sample suite, together with mineralogy and geochemical characteristics provide insights into the petrogenesis of the suite. As noted, the samples are all phaneritic in texture, and further show key characteristics of cumulate textures (Chapter 4). The classification and associated interpretations of cumulate textures as discussed in Wager et al., (1960) and Irvine (1982) and only a brief summary is presented here (Figure 1-5).

Cumulate refers to rocks formed by the crystallisation of cumulus crystals that settle out from a fractionating melt (e.g., Emeleus and Troll, 2014, Wager et al., 1960). The liquid that cumulus crystals are enclosed in is the intercumulus liquid. The intercumulus liquid can interact with the cumulus crystals through either diffusion or by forming overgrowths on the crystals. The liquid can also crystallise separately and form intercumulus crystals.

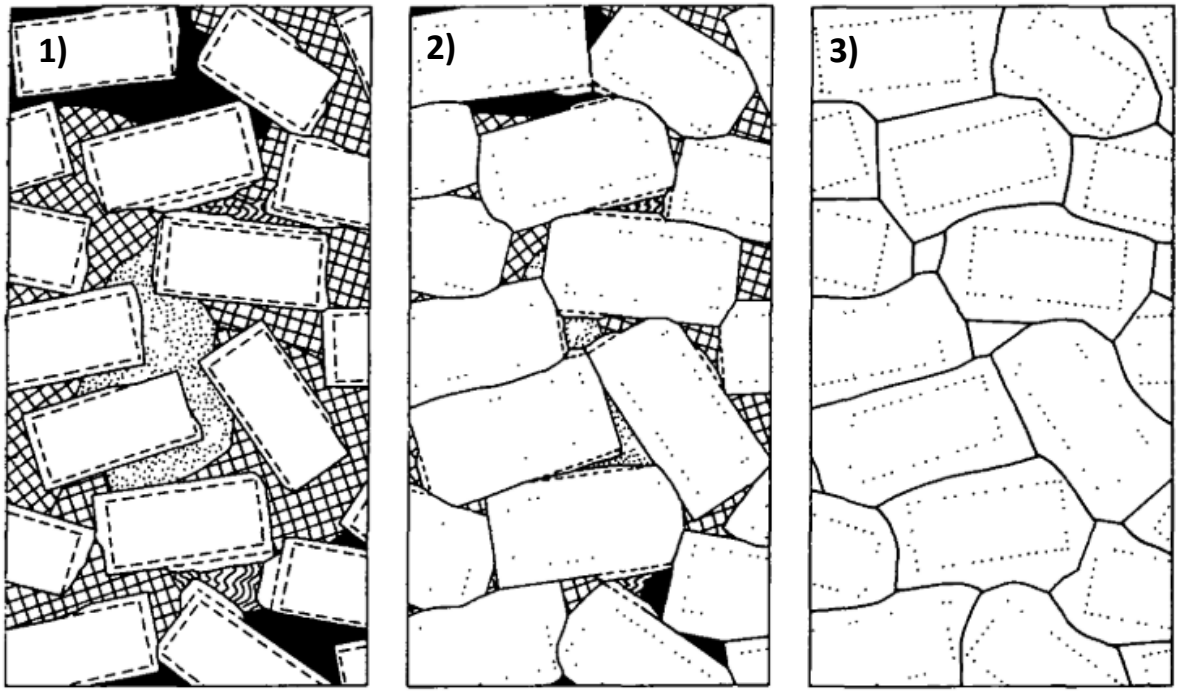

Figure 1-5: Schematic diagram of the different cumulate textures. 1) Orthocumulate, 2) Mesocumulate, 3) Adcumulate. White rectangles are plagioclase with other patterns indicating intercumulus material.
Schematic modified from Brown et al., (1960).

i) Orthocumulates consist of 75-85% cumulus crystals and the intercumulus liquid has solidified between the crystals. The crystals here rapidly accumulate on the base of the magma chamber which traps the liquid between the crystals (Wager et al., 1960).
ii) Adcumulates consist of 93-100% cumulus crystals and the intercumulus liquid has been squeezed out of the spaces between these crystals and leaves unzoned cumulus crystals. These rocks have formed through slow accumulation of the crystals at the base allowing time for them to become enlarged at expel liquid between the crystals (Wager et al., 1960).
iii) Mesocumulates are the intermediate between the two extremes and consists of 85-93% cumulus crystals with varying amounts of intercumulus liquid.

1.4 Thesis Objective and Outline

The primary aim of this thesis is to evaluate the petrogenesis and the tectonomagmatic association of a suite of cumulate rocks dredged from a basin associated with the modern Kermadec Arc-Havre Trough (KAHT). Although cumulate xenoliths have been reported from Kermadec arc magmas (Barker, 2010), this study involves the first petrographic and geochemical study of non-xenolithic *cumulate* rocks that have been found in the KAHT.

The nature of the samples, specifically their crystalline texture combined with seawater alteration, led to a mineral-specific analytical approach. The main analytical techniques used are:

- Petrographic study using back-scatter electron (BSE) images produced using an electron probe micro analyser (EPMA)
- *In situ* mineral major element analysis using EPMA
- *In situ* trace element analysis of clinopyroxene grains using Laser Ablation Inductively Coupled Plasma Mass Spectrometry (LA-ICP-MS).

This research will seek to answer the following questions:

1) Do the samples represent a single, related magmatic suite or a range of different magmas?
2) Under what conditions did the samples crystallise?
3) What part of the wider subduction system do these samples represent? Three tectonomagmatic associations are proposed:
    i) Modern Kermadec Arc-Havre Trough magmatism.
    ii) Magmatism associated with the now rifted Miocene (Colville) arc crust
    iii) Pre-arc oceanic crust

Addressing these questions allows a testable petrogenetic model for the samples to be developed and lays the foundations for future studies to build on.

1.5 Thesis Structure

Chapter 1. *Introduction:*

An overview of subduction zones including their anatomy and geochemical aspects relating to magmatism and arc volcanism, nomenclature used throughout the thesis, as well as the objectives of the thesis.

Chapter 2. *Sample Location and Geological Setting:*

A background to the Kermadec Arc-Havre Trough and the subduction setting, the chemical and physical properties of magmatism and previous intrusive rocks found in the arc. Description of the sample site is also given.

Chapter 3. *Analytical Methods:*

A description of the methods used to obtain element data used in this thesis.

Chapter 4. *Results:*

The key results of this research, including textures, and compositional trends of mineral major and trace elements.

Chapter 5. *Discussion:*

Interpretation of the results, how they relate to the subduction-arc setting.

Chapter 6. *Conclusions:*

A summary of key findings and recommendations of future work.

References:

A list of all reference sources cited in this thesis.

Appendices: A series of appendices (A-1-A-4) are attached, that contain mineral chemical data, and analytical standards used during this study.

Chapter 2 Geological Setting and Sample Location

2.1 Overview of the Kermadec Arc-Havre Trough Subduction System

The Tonga-Kermadec oceanic arc magmatic system has formed in response to the westward subduction of the relatively cold and old (>80 Ma) Pacific plate beneath the Australian plate. It extends ~2500 km to north of New Zealand and is one of the longest and most volcanically active intra-oceanic arc systems on the planet (e.g., De Ronde et al., 2005, Gamble et al., 1994, Smith and Price, 2006). The Kermadec Arc-Havre Trough (KAHT) makes up the southern portion of this active oceanic arc system, extending for ~1300 km, from the intersection of the remnant Louisville Seamount Chain with the Tonga-Kermadec Trench in the north, at 25°S (Ballance et al., 1999, Ruellan et al., 2003, Timm et al., 2013), to continental New Zealand in the south, where magmatism transitions from an oceanic to continental arc, that is associated with the Taupo Volcanic Zone (TVZ) (Gamble et al., 1993a, Gamble et al., 1993b, Wilson et al., 1995)(Figure 2-1).

Relative plate convergence rates increase northward as the distance from the Pacific-Australian pole of rotation increases, with a rate of ~5 cm/yr in the southern Kermadec Arc, to ~24 cm/yr in the northern Tonga Arc (Demets et al., 1994). Back-arc extension occurs behind the Tonga-Kermadec arc front due to slab rollback of the Pacific plate, and has formed the associated back-arc basins, the Lau Basin to the north and the Havre Trough to the south (Figure 2-1). The rates of extension increase northward with rates ranging from ~15mm/yr in the Havre Trough to ~85 mm/yr in the Lau Basin (Demets et al., 1994, Gamble et al., 1996, Gamble et al., 1994). Extension is largely accommodated by spreading in the Lau Basin and possible extensional rifting in the Havre Trough (Wright et al., 1996). However, it has been suggested that the Havre Trough is a site of new crustal growth which has been described as ‘disorganised’ spreading evident by the >4000 m deep basins with axial ridges that represent magmatic activity (Tontini et al., 2019, Wysoczanski et al., 2010).

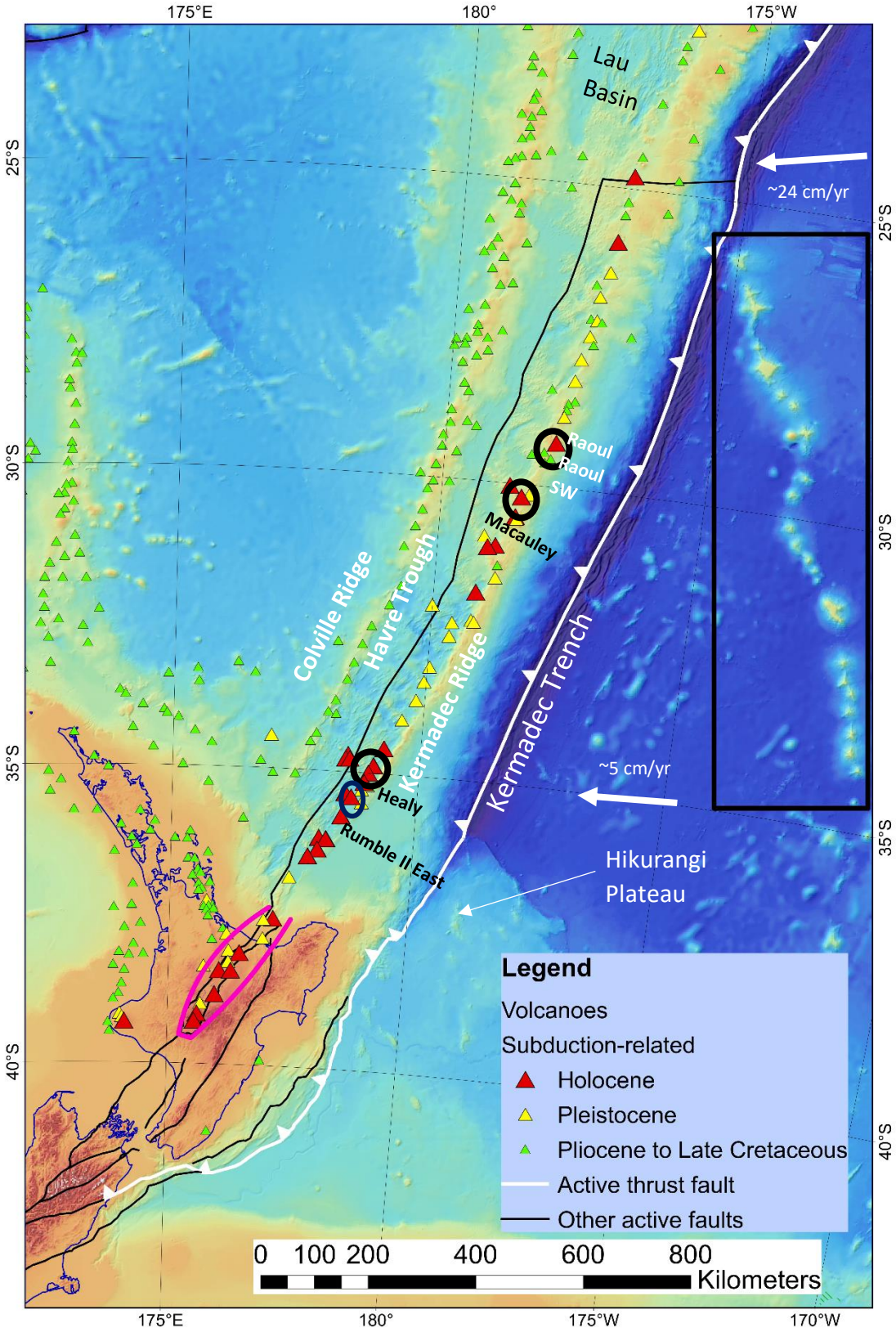

Figure 2-1: Regional setting of the Kermadec Arc-Havre Trough (KAHT)

The white line indicates the location of the subduction boundary of the Pacific and the Australian plates. Black box shows the remnant Louisville Seamount Chain. Pink lines indicate extent of the Taupo Volcanic Zone (TVZ) from Wilson et al., 1995. Black circles indicate approximate locations of Healy, Macauley, Raoul and Raoul SW from Barker 2010. Dark blue circle indicates location of Rumble II East volcano. Base map and volcano locations modified from (Mortimer N, 2020).

In addition to changes in the convergence rates along the arc the incoming sediment on the subducting Pacific plate changes systematically in composition and thickness with latitude, ranging from ~200 m of pelagic sediment found at ~25°S (Turner et al., 1997) to ~1 km thick terrigenous sediment in the southern Kermadec Arc, associated with Hikurangi fan drift and being located closer to continental New Zealand (Carter et al., 1996).

Subduction angles vary with latitude along the Kermadec subduction front and with depth. The angle of subduction beneath the southern Tonga/northern Kermadec Arcs changes from ~28° at 60 km depth to ~47° at 100 km depth (Bassett et al., 2016, Isacks and Barazangi, 1977). There is also a similar increase in angle that occurs in the southern Kermadec Arc from ~20° at 60 km depth to ~56° at 100 km depth (Bassett et al., 2016, Bassett et al., 2010). The upper portion of the subducting slab becomes steeper to the north which corresponds to a decrease in the distance from the Kermadec Ridge to the trench, from ~300 km at 37°S to ~185 km at 32°S (Wright, 1997).

The Colville Ridge, and the sub-parallel Kermadec Ridge (Figure 2-1) represent remnants of the once contiguous Colville volcanic arc (e.g. Timm et al., 2019) Limited dating of volcanic samples suggest that the Colville arc was active from ca. 17 Ma (Mortimer et al., 2010) to ca. 2.6 Ma (Timm et al., 2019). Trench roll-back and a clockwise rotation of the trench (Gamble and Wright, 1995) split the remnant arc into two ridges and formed the Havre Trough. The timing of the rifting is still contentious with some authors suggesting it commenced at ca. 5 Ma (e.g., Parson and Wright, 1996, Wright, 1993) and others suggesting ca. 2 Ma and even as recent as ca. 1 Ma (e.g., Malahoff et al., 1982, Wysoczanski et al., 2019).

The morphology, location of the arc front relative to the Kermadec Ridge, and the dip of the subducting plate of the Kermadec Arc-Havre Trough also changes with latitude, with a distinct boundary of these changes being ~32˚S, between the southern and northern KAHT (Wright, 1997). North of 32˚S the Havre Trough is relatively shallow (<2500 m), sediment-rich, and structurally simple with the Kermadec volcanic arc located on the Kermadec Ridge. South of ~32˚S the Havre Trough region is deeper (3000-3750 m), relatively sediment free, and structurally more complex with the active arc front located within the Havre Trough, ~15 km west of the Kermadec Ridge, also in this region the Kermadec and Colville Ridges narrow in width by almost half (Wright, 1997) (Figure 2-1). This variation in

morphology and structure may be related to the subduction of the Hikurangi Plateau, which is currently being subducted underneath the southernmost Kermadec Arc (south of ~35˚S) and the North Island of New Zealand (e.g., Timm et al., 2014, Timm et al., 2016).

The Havre Trough has a complex structural history and interpretations have varied over time regarding its formation. Initial interpretations of aeromagnetic survey data of the region was that active ocean spreading was occurring (Malahoff et al., 1982). However, the discovery of short, deep en-echelon rifts, from studies using airborne magnetics, gravity, and bathymetric mapping (e.g., Caress, 1991), in the southern Havre Trough and the absence of an axial spreading centre prompted Wright et al. (1996) to interpret the morphology of the southern Havre Trough as a contiguous system of en-echelon rifts with magmatic intrusives between rift blocks comprised of arc basement material. This interpretation has resulted in the Havre Trough being regarded as associated with back-arc rifting. These previous studies presented limited representation of the structure and morphology of the Havre Trough it was not until the *R/V Yokosuka* YK-06 voyage the entire width of the southern Havre Trough was surveyed in detail, using high resolution multibeam data, submersible observation and sample collection, and deep tow cameras (e.g., Wysoczanski et al., 2010). The data acquired during the *R/V Yokosuka* YK-06 voyage showed that the southern Havre Trough is comprised of regions of basal plateaux that have an average of 2500-3000 mbsl and are topped by ridges and volcanic seamounts, and regions of short-segment, deep rifts that have depths that exceed 4000 mbsl. These two regions have been defined as representing different regimes in the region, the plateaux, ridges and seamounts represent a constructional 'arc regime' and the deep rifts represent a basinal 'rift regime' (Wysoczanski et al., 2010). The southern Havre Trough deep rifts morphology is similar to that found in the southern Valu Fa Ridge and the Western Lau Basin, which are both considered to be in a phase of nascent 'disorganised' spreading before developing into an oceanic spreading centre as exemplified by the Lau Basin (Martinez and Taylor, 2006, Wysoczanski et al., 2010).

2.2 Kermadec Arc-Havre Trough Magmatism and Volcanism

A majority of the volcanoes found along the KAHT are submarine, with Raoul, Macauley, Curtis and L'Esperance being the only edifices found above the sea-level. Multi-

beam mapping shows that south of 30°S, the Kermadec Arc consists of at least 35 stratovolcanoes or silicic calderas (Wright et al., 2006, Wysoczanski et al., 2010).

Volcanism in the KAHT is primarily basaltic-andesitic in composition (~48-53 wt.% SiO_2; Gamble et al., 1993a, Gamble et al., 1993b, Gamble et al., 1990; Figure 2-2). However, a wider range of lavas compositions and the associated edifice types are observed along the volcanic front and has been linked to the thickness of the underlying crust (Wright et al., 2006). Stratovolcanoes that are associated with basement depths of >3200 mbsl and thinner crust the lavas erupted are dominated by low-K basalt-basaltic andesite whereas those stratovolcanoes and calderas that are associated with higher basement depths (<2500 mbsl) and therefore thicker crust appear to have erupted lavas in sub-equal proportions of dacite and basalt-basaltic andesite (Wright et al., 2006). Wright et al. (2006) suggest that the formation of dacitic magma is influenced by thickness of the crust, where rising basaltic magma can stall and undergo differentiation and crustal anatexis. Most basaltic-basaltic andesite volcanoes found of the southern Kermadec Arc rise to water depths of <1000 mbsl and display similar textual transitions, such as effusive pillow basalts, massive flows, pillow and talus breccia to fragmented/scoriaceous hyaloclastite-pyroclastic deposits (Wright et al., 1996, Wright et al., 2006). The back-arc samples from the Havre Trough range from basalt to andesite, similar to the Kermadec Arc but have higher alkali contents (<4.2 wt.% K_2O+Na_2O at 50 wt.% SiO_2; compared with <3 wt.% K_2O+Na_2O at 50 wt.% SiO_2 Gamble et al., 1993b; Figure 2-2).

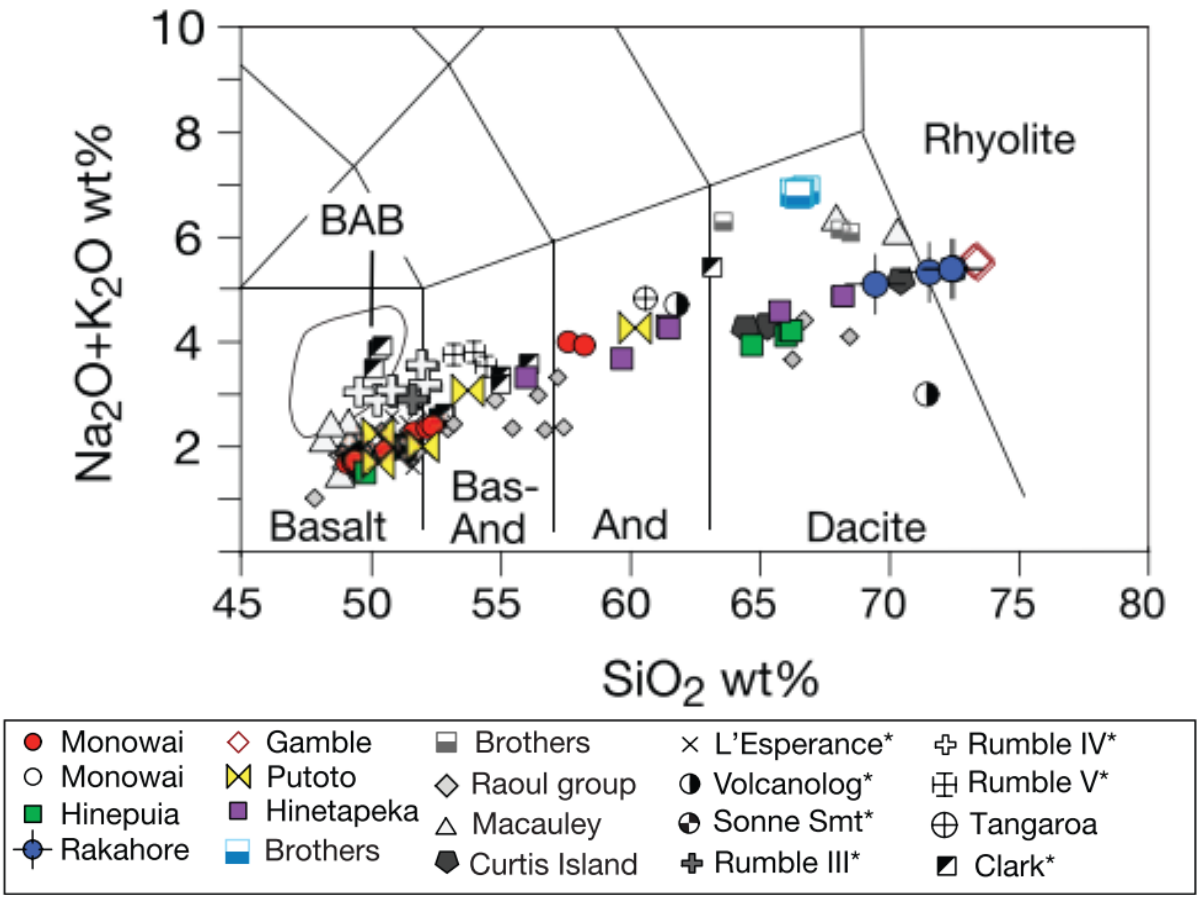

Figure 2-2: Silica vs. total alkalis for Kermadec Arc lavas. Classification fields from Le Maître et al. (2002).
Sourced from Timm et al. (2012). BAB field represents southern Lau Basin and Havre Trough basalts. Data collected partly from (marked by asterisk in legend) Turner et al. (1997); Ewart et al. (1998); Haase et al. (2002, 2006); Smith et al. (2009); Todd et al. (2011). For Monowai and Brothers, coloured white/grey symbols represent data from Timm et al. (2012) and previous literature data, respectively.

The composition of Kermadec Arc magmas is influenced by variable contributions from aqueous fluids and sediment melt slab-derived components in the mantle wedge source (e.g., Haase et al., 2002). Along the length of the Kermadec Arc there are variations in the relative contributions of slab derived components to magma. Northern Kermadec Arc lavas typically showing enrichments in LILE (e.g. Rb=2.27-4.41 ppm, Sr=114-194 ppm, Ba=34.7-77.3 ppm, Haase et al., 2002) which indicate aqueous fluid enrichment but limited sediment melt flux (Haase et al., 2002). Whereas southern Kermadec Arc lavas show a greater enrichments in LILE (Rb=0.54-43.3 ppm, Sr= 151-234 ppm, Ba=119-1030 ppm Haase et al., 2002) and LREE (La/Yb=0.86-3.33 vs. La/Yb=0.82-0.99 for northern samples, Haase et

al., 2002) interpreted as a greater contribution from sediment melt to the slab-derived component (e.g., Haase et al., 2002). Mixing of subducting sediment components into the ambient mantle wedge is also supported by isotopic compositions of lavas from the southern Kermadec Arc and back-arc (Gamble et al., 1996, Haase et al., 2002).

The composition of the ambient mantle prior to the addition of subduction-derived components is believed to be similar to 'Pacific' MORB mantle (Gill et al., 2020, Haase et al., 2002). The isotopic compositions of back-arc lavas are consistent with Pacific-type MORB ($^{87}Sr/^{86}Sr$ ~0.7026, $^{143}Nd/^{144}Nd$ ~0.51311, $^{206}Pb/^{204}Pb$ ~18.7; Haase et al., 2002). These isotopic compositions vary with latitude along the KAHT system (Gill et al., 2020, Haase et al., 2002, Timm et al., 2014). Source depletion, as traced by ratios of fluid immobile elements (e.g. Nb/Yb), also varies with latitude, with broadly increasing depletion northwards along the arc, southern Kermadec Arc, Nb/Yb=0.23-0.70 compared to northern Kermadec Arc, Nb/Yb=0.075-0.17 (e.g., Haase et al., 2002). This latitudinal variation has been correlated to the decrease in back-arc spreading rates and propagating back-arc basin opening southward (Gamble et al., 1993a, Turner et al., 1997). Alternative explanations for this variation however, include that the shallower dip of subduction, north of 30°S, may inhibit sub-arc mantle replenishment to the north (Gamble et al., 1993a, Haase et al., 2002), or the subduction of the Hikurangi Plateau south of ~32°S may introduce a distinct compositional component to the subduction system (Timm et al., 2016). As well as variations along arc there are also variations across-arc, with the mantle underlying the Kermadec Arc front being more depleted than the mantle beneath the adjacent Havre Trough back-arc (e.g., Wysoczanski et al., 2012a).

2.3 Intrusive Igneous Rocks of the KAHT

There have been very limited studies of intrusive igneous rocks from the KAHT owing to the rarity of samples. The few studies that have been conducted on intrusive rocks, however, are on xenoliths that are associated with extrusive material (e.g., Barker, 2010, Barker et al., 2013, Timm et al., 2016). The documentation of the xenoliths from the eruptive products in these studies have provided insights into the processes occurring at depth and how these are linked to the material that has been erupted. In the KAHT, it was

previously thought that silicic magmatism was formed by the melting crustal mafic amphibolite (e.g., Smith et al., 2010). Mafic xenoliths found within some pumices and associated eruptive deposits from Kermadec silicic volcanoes, Raoul, Raoul SW, Macauley, and Healy (Figure 2-1) provide evidence suggesting that the Kermadec Arc silicic magmas form from a dominantly fractional crystallisation of mafic magmas in addition to open source magma mixing as opposed to the melting of the lower crust and that the magmatic system that underlies the KAHT is more complex than previously thought (Barker, 2010, Barker et al., 2013).

Two intrusive rocks, a pyroxenite and gabbro, that were associated with mafic lavas from Rumble II East volcano (Figure 2-1) were analysed as part of a larger study into the subduction of the Hikurangi Plateau (Timm et al., 2016). The pyroxenite was determined to be from the Moho transition zone and was proposed to represent evidence of a mantle rock that shows a geochemical imprint of the subduction of the Hikurangi Plateau (Timm et al., 2016). The gabbro was suggested to have come from a mid-crustal region. The isotopic compositions that the gabbro exhibited were suggested to be that either the parental melt of the gabbro stagnated at the Moho transition zone and incorporated a Hikurangi isotopic signal, or the melt did not spend long enough in place to melt mélange fragments to change the isotopic signature (Timm et al., 2016).

2.4 Sample Location

The intrusive samples examined in this thesis come from a single seafloor dredge along the northwest wall of a basin in the Havre Trough, Basin E, located ~ 8 km north of Rumble II West volcano (Figure 2-3).

2.4.1 Basin E

Compared to the Kermadec arc front volcanoes, magmatism in Basin E, has had been the subject of very limited study, with only four lava samples analysed petrographically and geochemically (whole rock major and trace element data) as part of a MSc thesis examining the geomorphology and geochemistry of Southern Havre Trough basins (Pullan, 2018).

Basin E is located ~8 km north of Rumble II West and ~28 km from the Kermadec Ridge and is 20 km wide and 30 km long with a depth of ~2500-3000 mbsl (Figure 2-3). It contains a large continuous ridge that is ~500 m-1 km wide and ~10-15 km long, which is near where samples were collected by dredge during the 2012 *R/V Tangaroa-NIRVANA* voyage (Wysoczanski et al., 2012b) (Figure 2-4). Also present within the basin are several large cones, 2-4 km wide and 3-5 km long, located to the northwest of the sample site (Pullan, 2018) (Figure 2-4).

The sampled back-arc lavas are generally basalts (~51-52 wt.% SiO_2) with a porphyritic texture and the dominant phenocryst phases are plagioclase + olivine + pyroxene (~10-25 vol.% phenocrysts) (Pullan, 2018). The Basin E basalts are less evolved (~51-52 wt.% SiO_2, Pullan, 2018) than basalts from the nearby arc volcano, Rumble II West (~51-55 wt.% SiO_2, Timm et al., 2016). The Basin E basalts also exhibit slightly higher Na_2O+K_2O content when compared to Rumble II West, ~3.1-3.7 wt.% (Pullan, 2018) vs. ~2.6-3.1 wt.% (Timm et al., 2016). The aqueous fluid component, measured using Ba/Th ratios, in the sampled back-arc lavas is lower than the arc front volcanoes, <60-124, Basin E (Pullan, 2018) vs. 47-233 (e.g., Gamble et al., 1990, Haase et al., 2002, Timm et al., 2016). This indicates that the mantle source for the back-arc has undergone less flux from aqueous fluid from subduction-derived components than the Kermadec Arc front mantle source (e.g. Haase et al., 2002, Pullan, 2018, Todd et al., 2010, Todd et al., 2011). La_N/Sm_N ratios, which is a measure of the sediment melt component, for the back-arc basins indicates that there is greater modification of the mantle wedge from sediment melt subduction component the further from the volcanic front (Pullan, 2018).

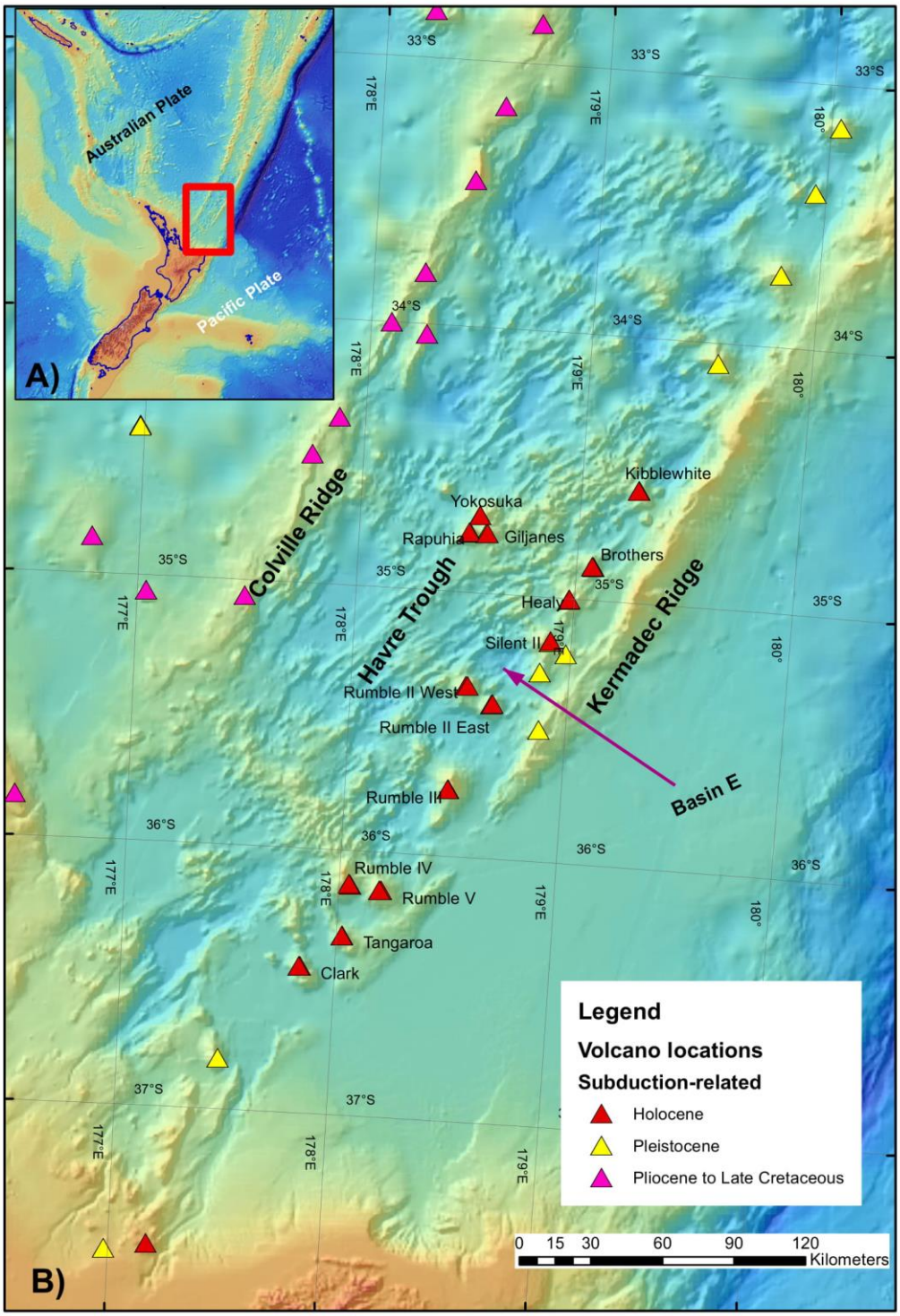

Figure 2-3: A) Shows regional location in relation to New Zealand and B) Shows an extent of the southern portion of the Kermadec Arc-Havre Trough

Sample site, Basin E, shown by purple arrow and the volcanoes present in the arc shown by coloured triangles. Base map and volcano locations modified from Mortimer N, (2020)

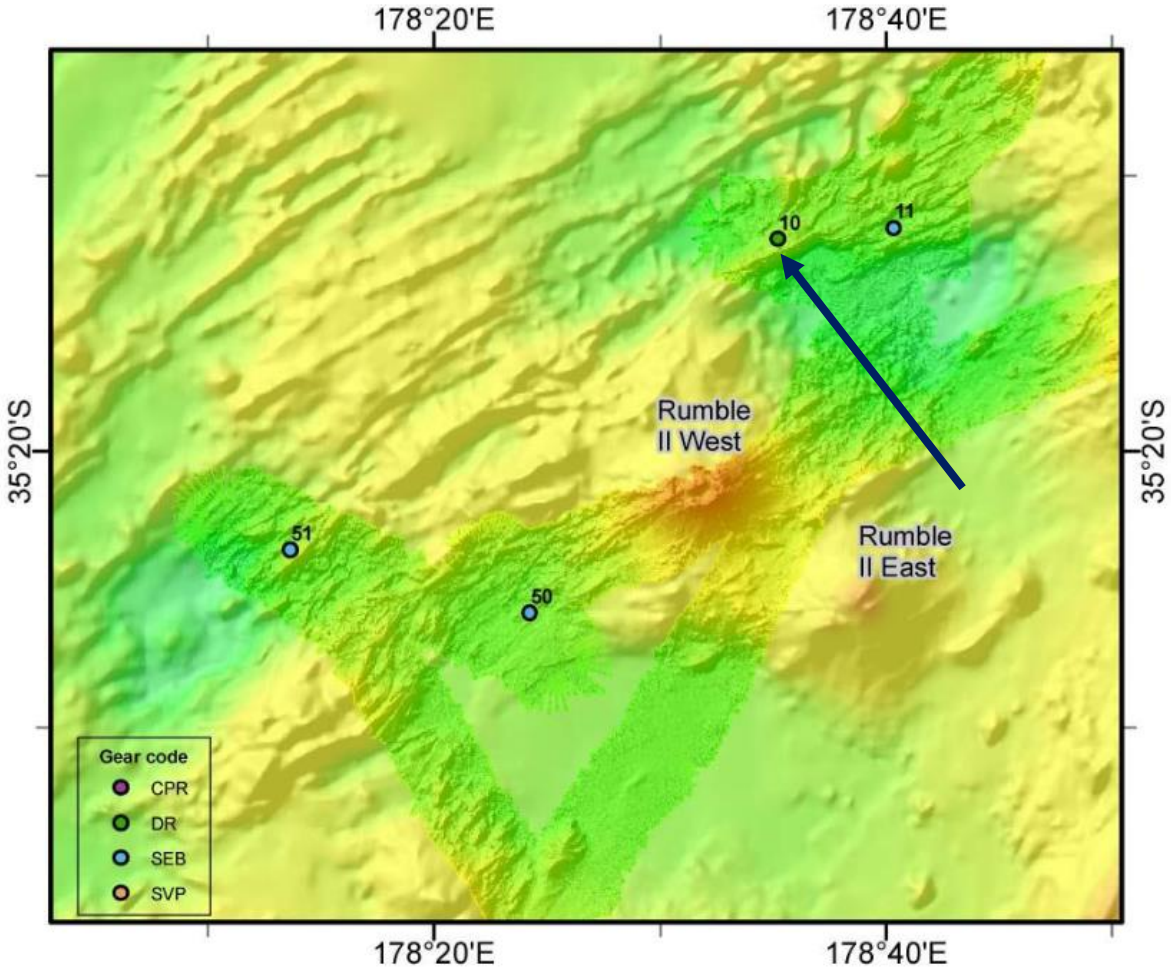

Figure 2-4: Multibeam data and location of dredge (blue arrow, Stn 10) in Basin E north of Rumble II West.
Modified from Wysoczanski et al. (2012b).
Gear Code: CPR (Continuous Plankton Recorder), DR (Rock Dredge), SEB (Epibenthic Sled), SVP (Sound Velocity Profile).

2.5 Sample Suite

The sample suite in this study comes from a single dredge from the northwest wall of Basin E (Figure 2-4) during the October 2012 *R/V Tangaroa-NIRVANA* voyage. Previous on-board identification of the samples was the first step in identifying appropriate samples for further analysis. 10 samples from the dredge were identified on-board as cumulates and the sample characteristics are shown in Table 2-1. Most of the samples that were identified as cumulates on-board had rims of alteration that varied in thickness.

Table 2-1; TAN1213 On-board Sample Log with descriptions of cumulates. Alt=alteration.
Modified from Wysoczanski et al., (2012b)

Sample No.	**Colour**	**Weight (kg)**	**Alteration**	**Texture**	**Notes**
TAN1213 10-1	Brown-green	4	Alt-rind, fresh interior	Cumulate	Gabbro
TAN1213 10-3	Brown-green	2.5	Slight rim alteration	Cumulate	Gabbro, 5 mm alt rim
TAN1213 10-5	Brown-grey	3.5	Alt rind, fresh interior	Cumulate	Gabbro, 1 cm alt rim
TAN1213 10-7	Green-grey	4.5	Alt rind, fresh interior	Cumulate	Gabbro, up to 7 cm alt rim
TAN1213 10-8	Green-grey	1	Alt rind, fresh interior	Cumulate	Gabbro, 1 cm alt rim
TAN1213 10-9	Brown-green	3	Alt rind, fresh interior	Cumulate	Gabbro, 1 cm alt rim
TAN1213 10-10	Dark grey	1.5	Alt rind, fresh interior	Cumulate	Gabbro, 1 cm alt rim
TAN1213 10-15	Dark grey	0.25	fresh	Cumulate	Gabbro
TAN1213 10-16	Brown grey	2.75	Alt rind, fresh interior	Cumulate	Gabbro, 2 cm alt rim
TAN1213 10-17	Dark green-grey	2	Alt rind, fresh intereior	Cumulate	Gabbro, 1 cm alt rim

Chapter 3 Analytical Methods

3.1 Sample Selection

Out of the ten samples that were identified as cumulates on-board, four were selected, TAN1213 10-1, 10-7, 10-8, 10-10, for detailed analysis and prepared into block mounts. The four samples were selected on the basis of grainsize following visual inspection of fresh cut surfaces of all ten samples. They each represent a different grainsize range that encompasses the range of the overall cumulate suite.

3.2 Sample Preparation

Due to the effects of variable alteration on even the freshest cores of the samples, 25 mm block mounts were made for analysis and to maximise the amount of material that remained for analysis: attempts to make thin sections resulted in substantial plucking, loss of cohesion of material, and a reasonable polish could not be obtained. Chips or blocks were selected rather than mineral grain mounts to preserve textural information. The block mounts comprised 20-30 mm sized chips that were placed on a glass slide prepared with double-sided sticky tape over which a 25 mm round mould was placed and filled with Struers Epofix resin and hardener. The mount was then placed on a hotplate set at 50°C to harden for 24 hours. The mounts were ground to expose the chip surface, which was then polished using successively finer sandpaper and silicon carbide (SiC) grit.

3.3 *In Situ* Mineral Major Element Analysis

In situ major element analysis was undertaken using electron probe microanalysis (EPMA). Each block mount was coated with a ~25nm film of carbon prior to analysis. Major element analysis of minerals was undertaken using a JEOL JXA 8230 SuperProbe electron probe microanalyser at VUW. The JEOL JXA 8230 SuperProbe is equipped with five wavelength dispersive spectrometers (WDS) that allow for quantitative analysis on the selected minerals. The JXA 8230 is also equipped with an energy dispersive X-ray spectrometer (EDS), and detectors that allow for the collection of backscattered electron (BSE) and secondary electron (SEI) image. The EDS was used for quick qualitative mineral phase identification to determine representative minerals for further quantitative analysis using WDS.

To reduce matrix effects, the EPMA was calibrated for quantitative measurements using primary mineral standards of similar composition to the material being analysed. For elements that were present in low abundances (e.g., ≤2 wt. %) calibration of the EPMA was carried out on synthetic oxide primary standards. A list of all the standards used for each mineral calibration is shown in Table 3-1. The calibration was carried out by a 30 s peak-search on each element, and a 15 s background measurement. All major element concentrations were calculated using the ZAF correction method, which corrects for the matrix effects of mass number (Z), absorbance (A), and fluorescence (F) that lead to incorrect element concentration calculations. The mineral standards, Kakanui Augite, Plagioclase NMNH 115900, Hornblende, Engels Amphibole, and Magnetite NMNH 115900 were run as secondary standards at the beginning, end, and after every 10 samples throughout the relevant mineral analytical run to monitor instrument drift. Uncertainties for most elements in the mineral standards were within 5-10% (see Appendix 3 for standard data).

Table 3-1 Matrix-matched and Synthetic Oxide standards used to calibrate the EPMA for mineral analysis.

Material	**Matrix-matched standards***	**Synthetic oxides**
Clinopyroxene	Kakanui Augite (Si, Al, Mg, Na, Ca, Fe, Ti)	MnO, Cr_2O_3
Plagioclase	Plagioclase NMNH 115900 (Si, Al, Mg, Na, Ca) Orthoclase Or-1A (K)	MnO, Cr_2O_3, TiO_2, Fe_2O_3
Amphibole	Hornblende (Si, Al, Mg, Na, Ca, Fe)	TiO_2, MnO, Cr_2O_3
Fe-Ti Oxides	Magnetite (Fe, Ti)	TiO_2, MgO, Al_2O_3, Cr_2O_3, V_2O_3 (Vanadinite), MnO

***Reference values for standard are presented in Appendix 3**

All quantitative analyses on minerals were undertaken using WDS with a focused beam of 1-2 µm spot diameter, an accelerating voltage of 15kV, and a beam current of 20nA. For all minerals, samples were measured for a total time of 30 s, and background

levels for a total of 15 s. Single analysis of minerals were focused on the cores of minerals such as clinopyroxenes and amphiboles due to no evidence from BSE of compositional zoning. Plagioclase cores were the main focus with only some rim measurements of minerals undertaken where there was evidence of compositional zoning at the rims of some of the larger crystals. Mineral proportions were determined through BSE imaging on the EPMA using spot counting of 40 random points on each sample.

Analytical data was then normalised and Fe_2O_3 calculated through charge balance calculations. Endmember calculations were also performed for plagioclase (An, Ab, Or) and clinopyroxene (Wo, En, Fs), using the following equations and elements from the respective minerals.

$$An = \frac{Ca}{Ca + Na + K}$$

$$Ab = \frac{Na}{Ca + Na + K}$$

$$Or = \frac{K}{Ca + Na + K}$$

$$Wo = \frac{Ca}{Ca + Mg + FeT}$$

$$En = \frac{Mg}{Ca + Mg + FeT}$$

$$Fs = \frac{FeT}{Ca + Mg + FeT}$$

3.4 Clinopyroxene Trace Element Analysis

A sub-set of clinopyroxene grains were selected for *in situ* trace element analysis using a Resonetics S155-SE (193nm) Excimer laser coupled with an Agilent ICP-MS at Victoria University of Wellington. The EPMA carbon coating was removed from the epoxy mounts using 3µm Al_2O_3 suspended solution and cleaned using Milli-Q. The sample mounts were then loaded together with standard glass mounts; BHVO-2G, BCR-2G, and NIST612, which were used for calibration and monitoring drift throughout the analytical run. All data were

acquired as static spot analyses on the same spot locations analysed using the EPMA. Two spot sizes were used during the analytical run, determined by the size of the grain analysed, 30 µm for small grains and 50 µm for larger grains. Both spot sizes were analysed for 30 seconds. Samples were ablated with He gas (400 mL/min) in the sample chamber, and with Ar (910 mL/min) and N_2 (2.5 mL/min) added as carrier gasses to the ICP-MS. The laser energy was set to 5 mJ, with attenuation of 25% transmission, and a repetition rate of 10 Hz. Standards for both spot sizes, 30 µm and 50 µm were analysed every 5 samples to monitor instrument drift.

Trace element abundances were derived using IOLITE software with BHVO-2G as the primary calibration standard and Ca as the reference mass to calibrate trace element data with CaO measured by EPMA. In total 39 trace elements were measured. BHVO-2G was used as calibration as it has the closest bulk chemistry to the clinopyroxene grains that were analysed. BCR-2G was measured as a secondary standard to check accuracy with most elements within 5-10% of reference values (Table 3-2). NIST612, an artificial glass standard was also analysed multiple times throughout the analytical run (Appendix 3).

Table 3-2: List of measured and preferred values for trace element abundances of glass standard BCR-2G.
Reference values were obtained from Jochum and Enzweiler (2013).

	Reference			Large spot size (50 um)				Small spot size (30 um)			
	values	SD		n	Average	SD	% diff	n	Average	SD	% diff
SiO2 (wt%)	54.4	0.4		36	50.9	5.1	-6	36	51.4	4.5	-6
TiO2	2.27	0.04		36	2.30	0.32	1	36	2.23	0.35	-2
Al2O3	13.4	0.4		36	13.1	1.2	-3	36	13.1	1.2	-2
FeO(T)	12.4	0.3		36	12.1	1.0	-2	36	12.1	1.1	-2
MgO	3.56	0.09		36	3.26	0.41	-9	36	3.33	0.41	-7
CaO	7.06	0.11		36	7.06	0.53	0	36	7.07	0.54	0
Na2O3	3.23	0.07		36	3.16	0.51	-2	36	3.18	0.45	-2
Li (ppm)	9	1		36	8.7	1.3	-3	36	8.58	1.38	-5
Sc	33	2		36	35	4	5	36	33.77	4.62	2
V	425	18		36	379	57	-11	36	381.53	53.58	-10
Cr	17	2		36	14	4	-17	36	15.23	2.19	-10
Co	38	2		36	36	2	-6	36	35.98	1.99	-5
Ni	13	2		36	11	1	-12	36	11.05	1.36	-15
Cu	21	5		36	17	2	-20	36	16.67	2.58	-21
Zn	125	5		36	125	17	0	36	128.37	17.26	3
Ga	23	1		36	22	2	-5	36	22.34	0.95	-3
Rb	47	0.5		36	46	6	-2	36	44.47	6.20	-5
Sr	342	4		36	316	46	-8				
Sr								36	331.50	34.61	-3
Y	35	3		36	33.6	2.9	-4	36	35.35	1.36	1
Zr	184	15		36	184	17	0	36	184.96	15.12	1
Nb	12.5	1		36	11.8	1.8	-6	36	12.13	1.74	-3
Mo	270	30		36	226	21	-16	36	232.70	8.75	-14
Cs*	1.16	0.07		36	1.1	0.1	-8	14	1.01	0.11	-13
Ba	683	7		36	673	97	-1	36	657.47	99.33	-4
La	24.7	0.3		36	23.2	3.1	-6	36	24.54	1.57	-1
Ce	53.3	0.5		36	52.0	4.5	-2	36	53.28	2.80	0
Pr	6.7	0.4		36	6.9	1.0	3	36	6.76	0.96	1
Nd	28.9	0.3		36	28.0	3.9	-3	36	27.95	4.20	-3
Sm	6.59	0.07		36	6.22	0.85	-6	36	6.34	0.90	-4
Eu	1.97	0.02		36	1.96	0.21	0	36	1.98	0.19	0
Gd	6.71	0.07		36	6.61	1.01	-2	36	6.54	1.01	-3
Tb	1.02	0.08		36	0.95	0.24	-7	36	1.00	0.14	-2
Dy	6.44	0.06		36	6.28	1.68	-2	36	6.21	0.61	-4
Ho	1.27	0.08		36	1.26	0.09	-1	36	1.29	0.07	1
Er	3.7	0.04		36	3.67	0.46	-1	36	3.64	0.50	-2
Tm	0.51	0.04		36	0.52	0.08	3	36	0.53	0.09	3
Yb	3.39	0.03		36	3.23	0.47	-5	36	3.33	0.50	-2
Lu	0.503	0.005		36	0.49	0.05	-3	36	0.49	0.04	-3
Hf	4.84	0.28		36	4.73	0.48	-2	36	4.78	0.43	-1
Ta	0.78	0.06		36	0.77	0.11	-1	36	0.76	0.12	-3
W	0.5	0.07		36	0.48	0.10	-4	36	0.51	0.13	2
Pb*	11	1		27	9.2	1.2	-16	36	9.83	1.02	-11
Th	5.9	0.3		36	5.73	0.44	-3	36	5.92	0.25	0
U	1.69	0.12		36	1.60	0.21	-6	36	1.59	0.18	-6

** an individual session returned poor data for these elements; those sessions are excluded from the average and SD calculations for BCR-2G, and these elements not reported for cpx samples analysed in the excluded session(s) .*

Chapter 4 Results

4.1 Sample Descriptions

Ten samples identified as cumulate were recovered from dredge at Station 10 (Section 2.5 and Table 2-1). These ranged from 0.25 to 4 kg in size with alteration rims identified by brown staining extending up to 7 cm into the samples. On a hand specimen scale, the relatively fresh cores of the retrieved samples varied predominantly by grainsize (Table 4-1). A representative sample from each grainsize category was selected for detailed analysis and are described in more detail below (Figures 4-1 to 4-15).

4.1.1 TAN1213 10-1

In hand sample TAN1213 10-1 is fine grained, with a ~2-4 cm brown alteration rim and the fresh core material is grey-green in colour (Figure 4-1). Grainsize ranges from ≤0.5-~1 mm and the sample has a mesocumulate to orthocumulate texture (Section 1-3 and Figures 4-2 to 4-4). The crystal assemblage consists of ~60% plagioclase, ~25% clinopyroxene, ~5% magnetite, and ~10% intercumulus material.

The plagioclase crystals are euhedral to subhedral, tabular in shape and range in size from ~0.1-0.5 mm (Figures 4-2 to 4-4). No signs of compositional zoning or disequilibrium textures such as sieve textures and oscillatory zoning are observed.

The clinopyroxene crystals present as subhedral to euhedral crystals that are long and tabular in shape, and range in size from ~0.3-1 mm (Figures 4-2 to 4-4). No compositional zoning is observed.

The magnetite crystals are subhedral to euhedral, tabular in shape, and range in size from ~0.1-0.5 mm (Figures 4-5 and 4-6).

The intercumulus material is mostly comprised of anhedral quartz that fills the spaces between other crystals (Figures 4-2 to 4-4). No other minerals were identified in the intercumulus material from this sample.

Table 4-1: All 10 samples identified as cumulates with grainsizes. Fine= ~0.5-1mm, Medium= ~1-1.5mm, Coarse= ~1.5-2mm.

Sample No.	**Grainsize**
TAN1213 10-1*	Fine
TAN1213 10-3	Fine
TAN1213 10-5	Medium
TAN1213 10-7*	Coarse
TAN1213 10-8*	Medium/Coarse
TAN1213 10-9	Coarse
TAN1213 10-10*	Medium
TAN1213 10-15	Coarse
TAN1213 10-16	Fine/Medium
TAN1213 10-17	Fine

***Samples selected for detailed analysis.**

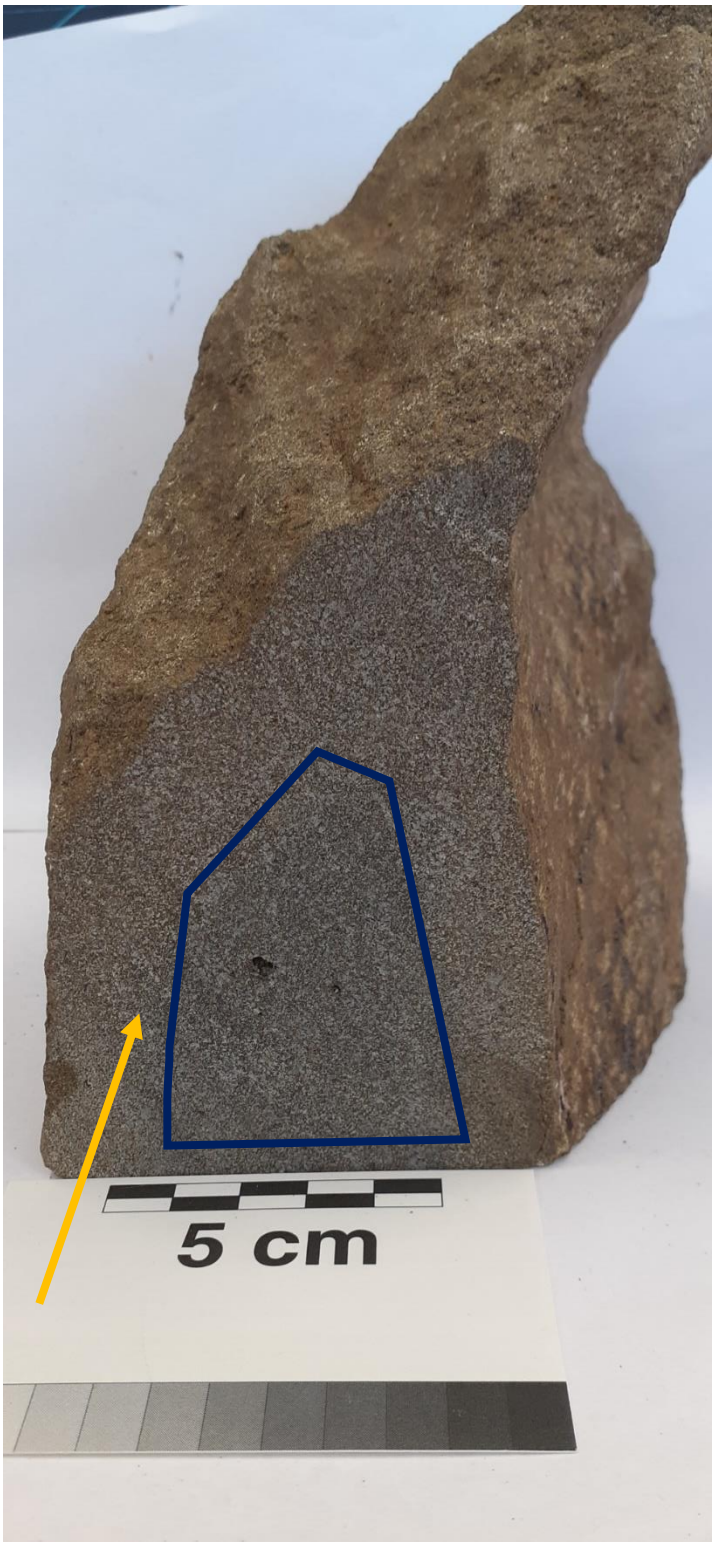

Figure 4-1: Hand sample photo of TAN1213 10-1 showing texture and grainsize

Dark blue shape shows the extent of fresh material while yellow arrow shows alteration rim

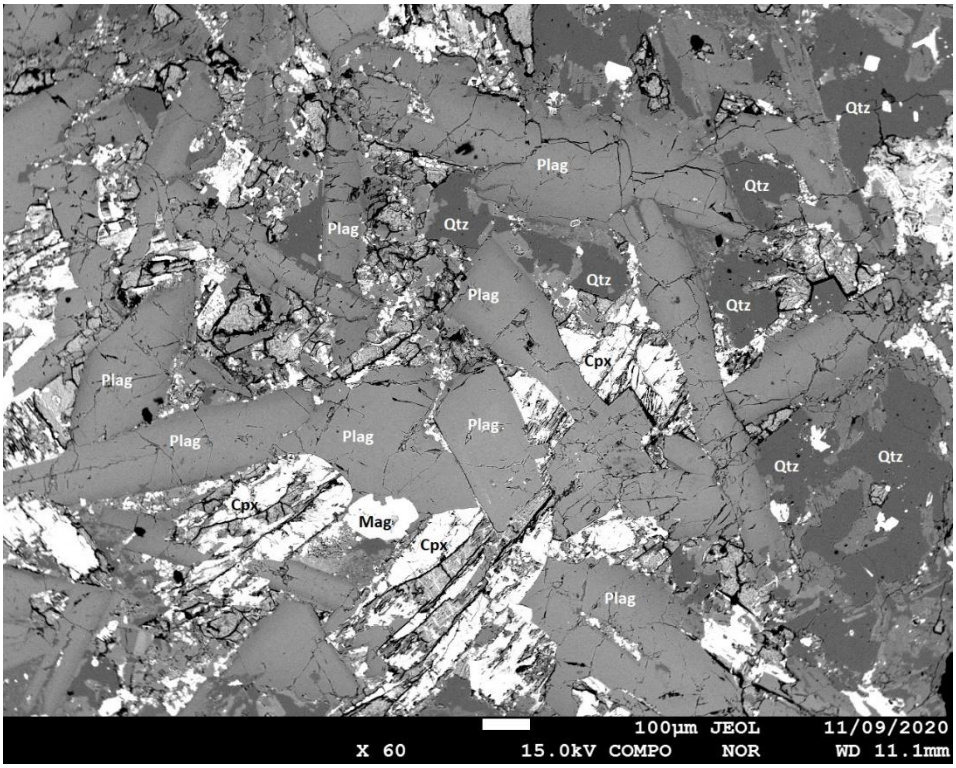

Figure 4-2: Backscatter electron image from TAN1213 10-1 showing grainsize, texture, and crystal shapes of clinopyroxene (Cpx), plagioclase (Plag), Magnetite (Mag), and Quartz (Qtz)

Mineral abbreviations from Whitney and Evans (2010).

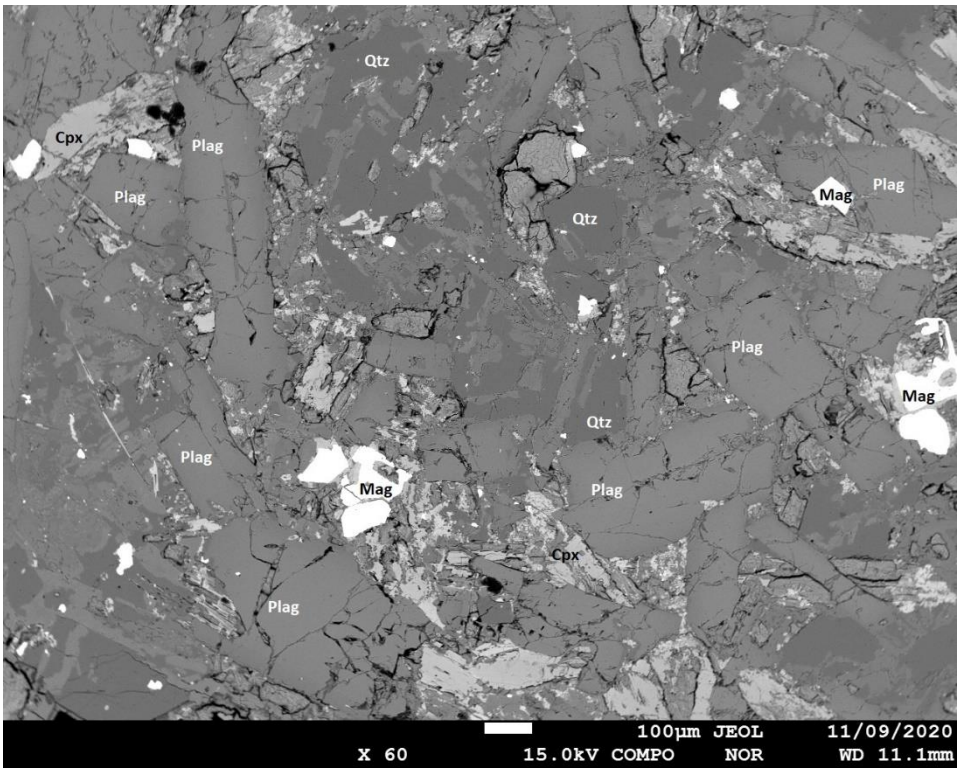

Figure 4-3: Backscatter electron image from TAN1213 10-1 showing grainsize, texture, and crystal shapes of clinopyroxene (Cpx), plagioclase (Plag), Magnetite (Mag), and Quartz (Qtz)

Mineral abbreviations from Whitney and Evans (2010).

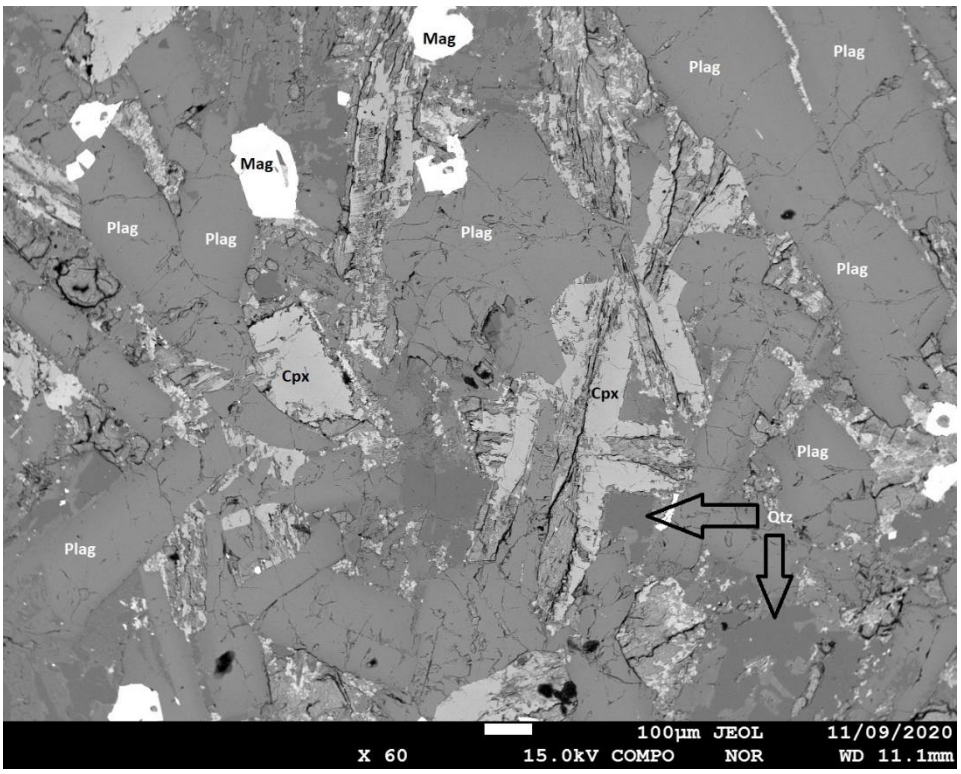

Figure 4-4: Backscatter electron image from TAN1213 10-1 showing grainsize, texture, and crystal shapes of clinopyroxene (Cpx), plagioclase (Plag), Magnetite (Mag), and Quartz (Qtz)

Mineral abbreviations from Whitney and Evans (2010).

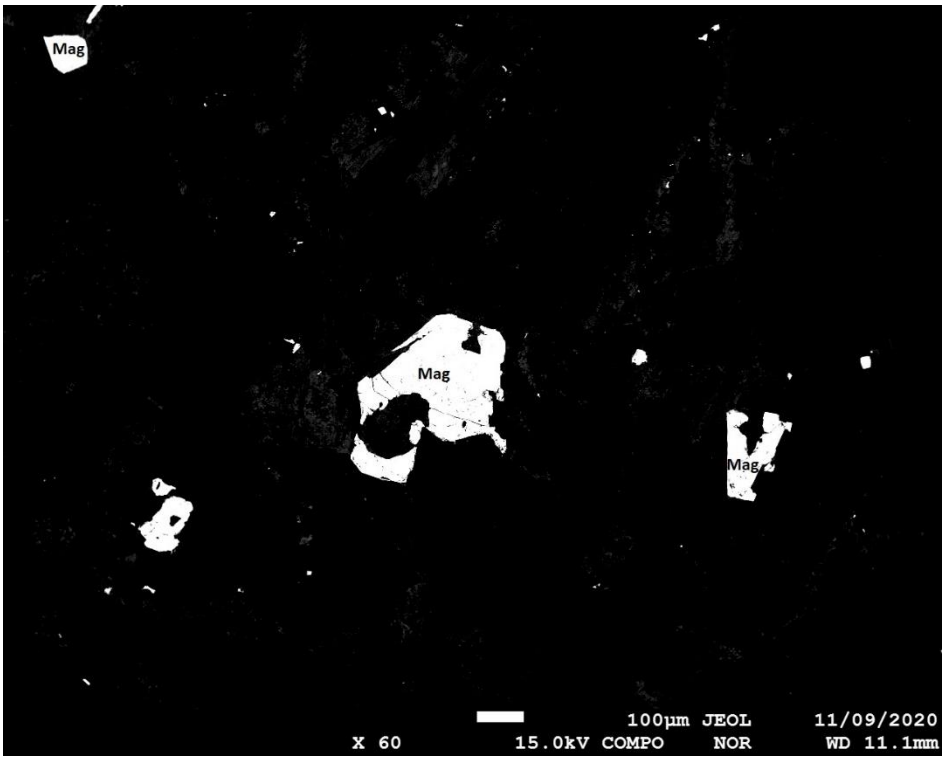

Figure 4-5: Backscatter electron images of magnetite (Mag) from TAN1213 10-1

Mineral abbreviations from Whitney and Evans (2010)

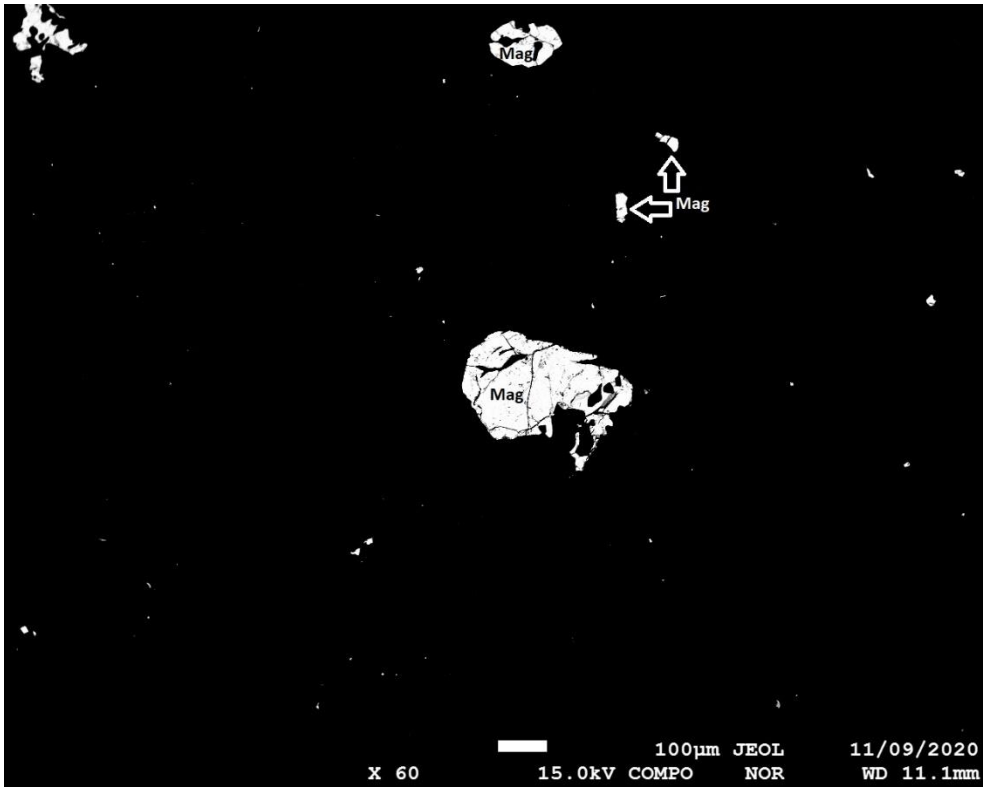

Figure 4-6: Backscatter electron image of magnetite (Mag) from TAN1213 10-1

Mineral abbreviations from Whitney and Evans (2010)

4.1.2 TAN1213 10-7

In hand sample TAN1213 10-7 is coarse grained and green in colour (Figure 4-7). Grainsizes ranges from ~0.5-2 mm and the sample has a relatively distinct orthocumulate texture (Figures 4-8 and 4-9). The crystal assemblage consists of ~50% plagioclase, ~20% clinopyroxene, ~3% magnetite, and ~27% intercumulus material. TAN1213 10-7 provides the best example of the orthocumulate texture as shown in Figure 4-8.

The plagioclase crystals are euhedral to subhedral, tabular, and range in size from ~0.5-2 mm (Figures 4-8 and 4-9). Most plagioclase crystals show no signs of compositional zoning or disequilibrium textures such as sieve textures and oscillatory zoning. However, some crystals have narrow rims of diffuse boundaries where they border the intercumulus material (Figure 4-8).

The clinopyroxene crystals present as subhedral to euhedral crystals that are long and tabular in shape, and range in size from ~0.3-0.5 mm (Figures 4-7 to 4-8). No compositional zoning is observed.

The magnetite crystals are subhedral to euhedral, tabular, and range in size from ~0.1-0.5 mm (Figure 4-10).

The intercumulus material is comprised of quartz, K-feldspar, more sodium rich plagioclase than the surrounding cumulus crystals, and amphibole. All the minerals are subhedral to anhedral in shape and range in size from ~0.1-0.4 mm (Figures 4-8 and 4.9).

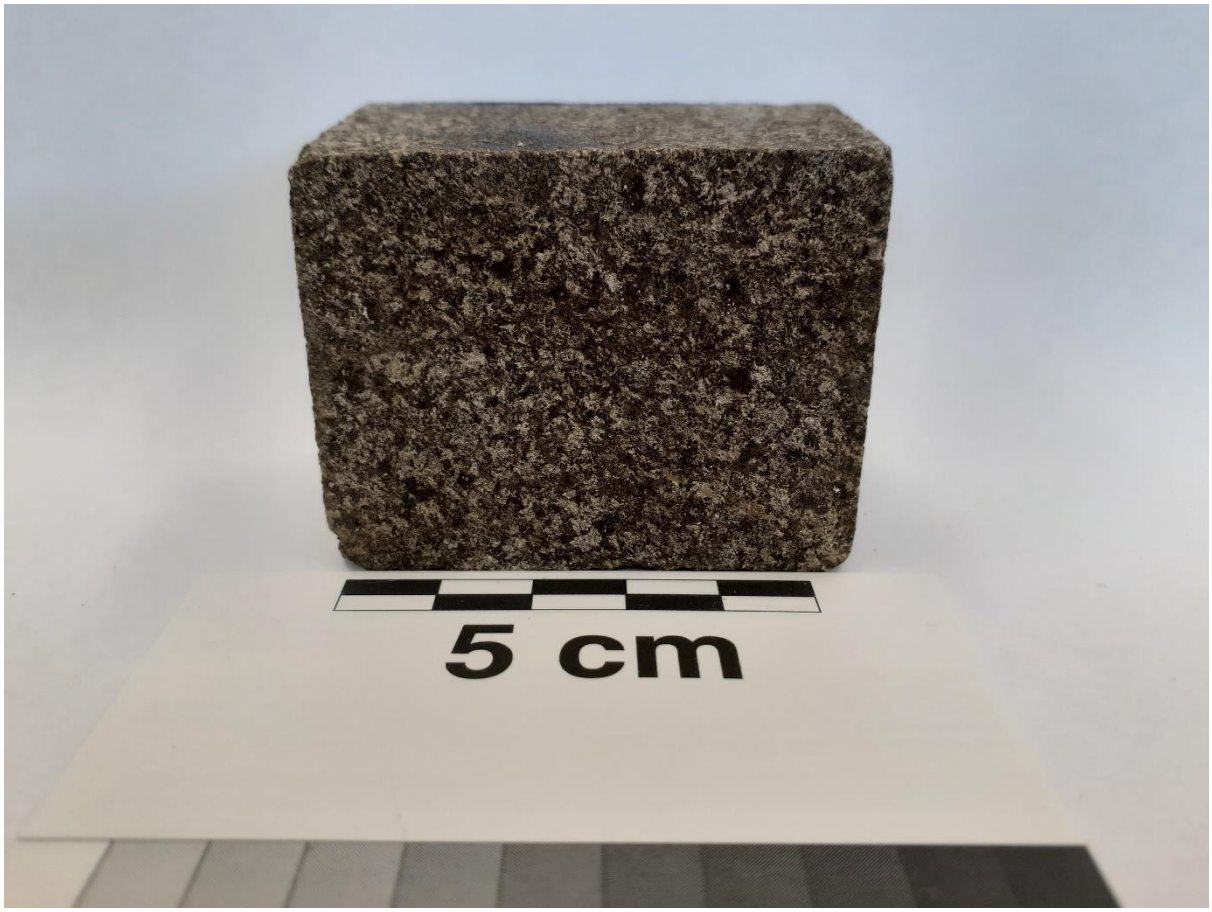

Figure 4-7: Cut block of TAN1213 10-7 which shows the texture, colour and grainsize present

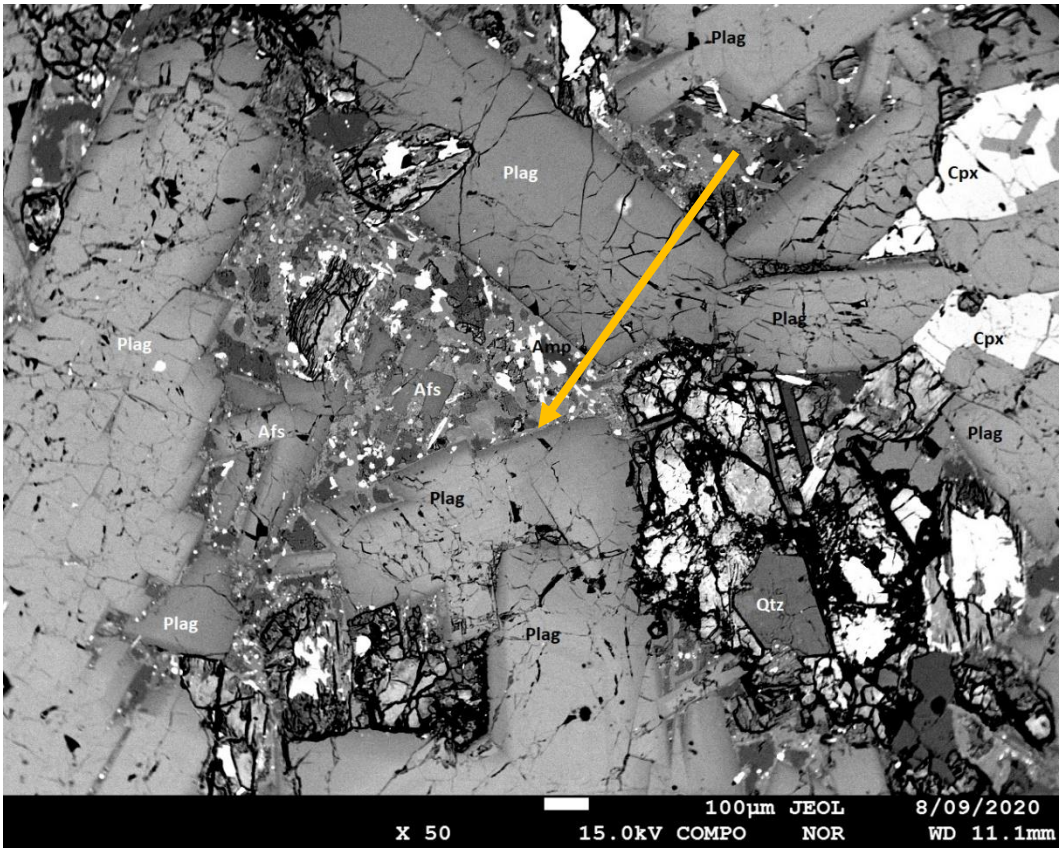

Figure 4-8: Backscatter electron image of TAN1213 10-7 which shows texture, grainsize, and minerals that are present. Yellow arrow indicates rim of plagioclase.

Mineral abbreviations from Whitney and Evans (2010)

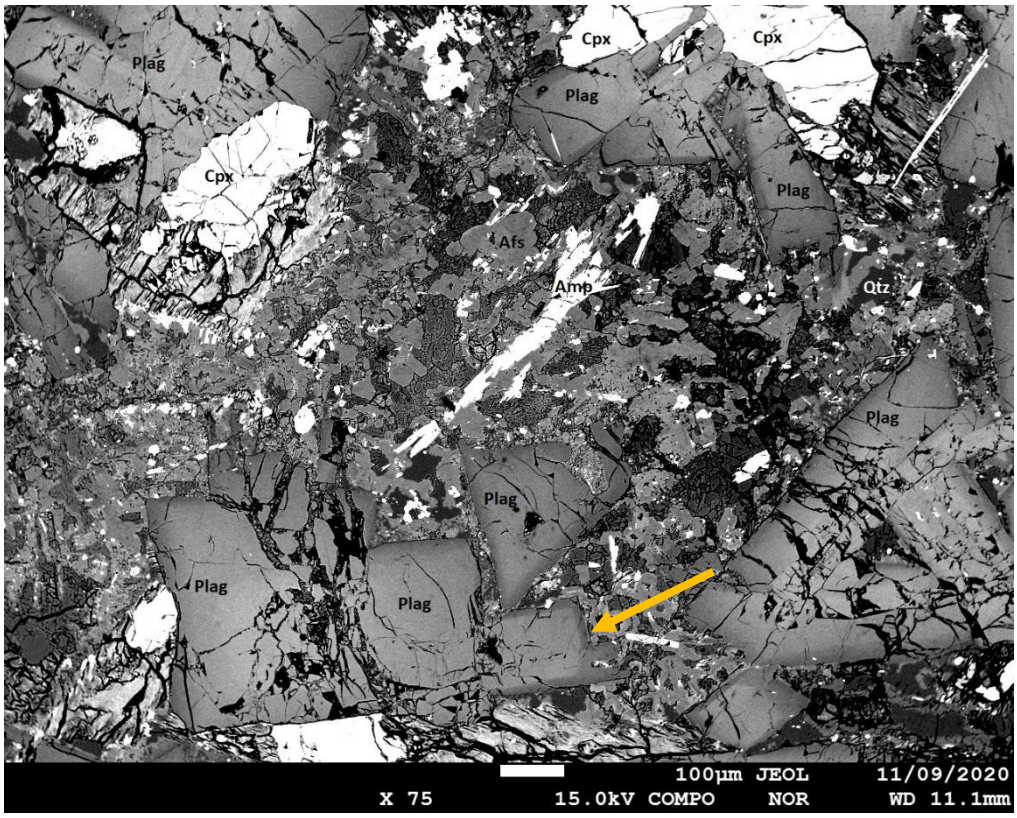

Figure 4-9: Backscatter electron image of TAN1213 10-7 which shows texture, grainsize, and minerals that are present. Yellow arrow indicates rim of plagioclase.

Mineral abbreviations from Whitney and Evans (2010)

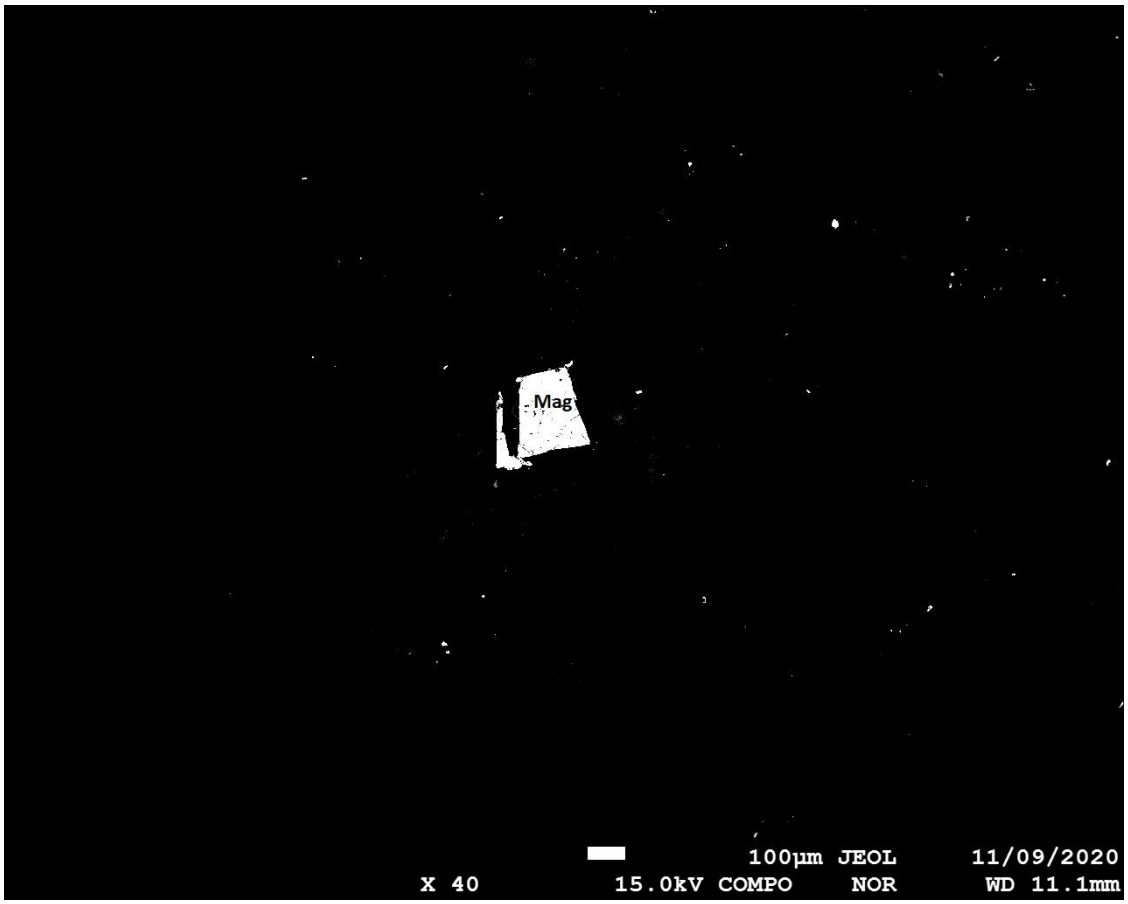

Figure 4-10: Backscatter electron image of a magnetite crystal from TAN1213 10-7

4.1.3 TAN1213 10-8

In hand sample TAN1213 10-8 is medium to coarse grained and is a green-brown in colour (Figure 4-11). Grainsize ranges from ~0.5-2 mm and the sample has a mesocumulate to orthocumulate texture (Figure 4-12). The crystal assemblage consists of ~60% plagioclase, ~20% clinopyroxene, ~3% magnetite, and ~17% intercumulus material.

The plagioclase crystals are euhedral to subhedral, tabular and range in size from ~0.5-2 mm (Figure 4-12). No signs of compositional zoning or disequilibrium textures such as sieve textures and oscillatory zoning were observed.

The clinopyroxene crystals are subhedral to euhedral, long, and tabular in shape, and range in size from ~0.3-0.5 mm (Figure 4-12). No compositional zoning is observed.

The magnetite crystals are subhedral to euhedral, tabular, and range in size from ~0.1-0.2 mm (Figure 4-12).

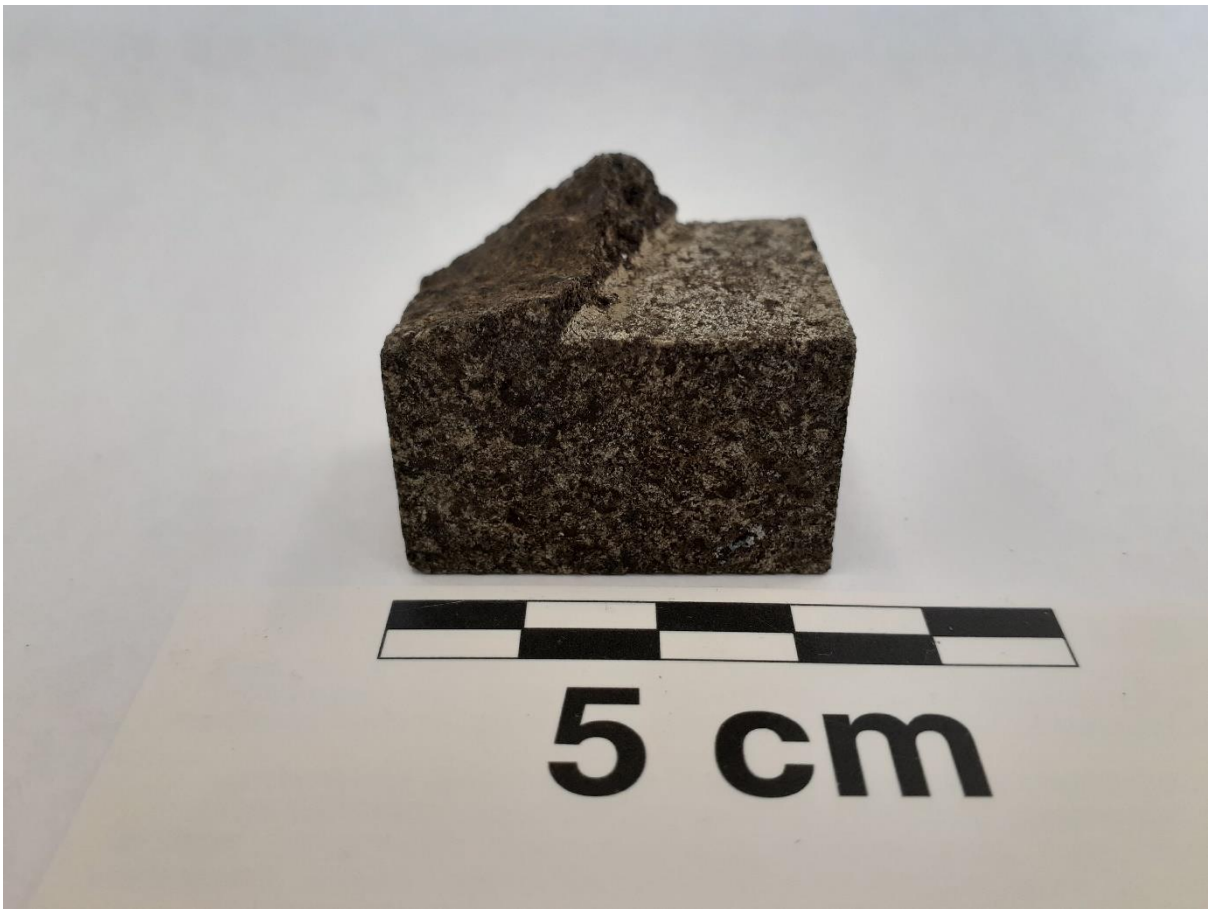

Figure 4-11: Cut block hand sample of TAN1213 10-8 showing texture, colour, and grainsize

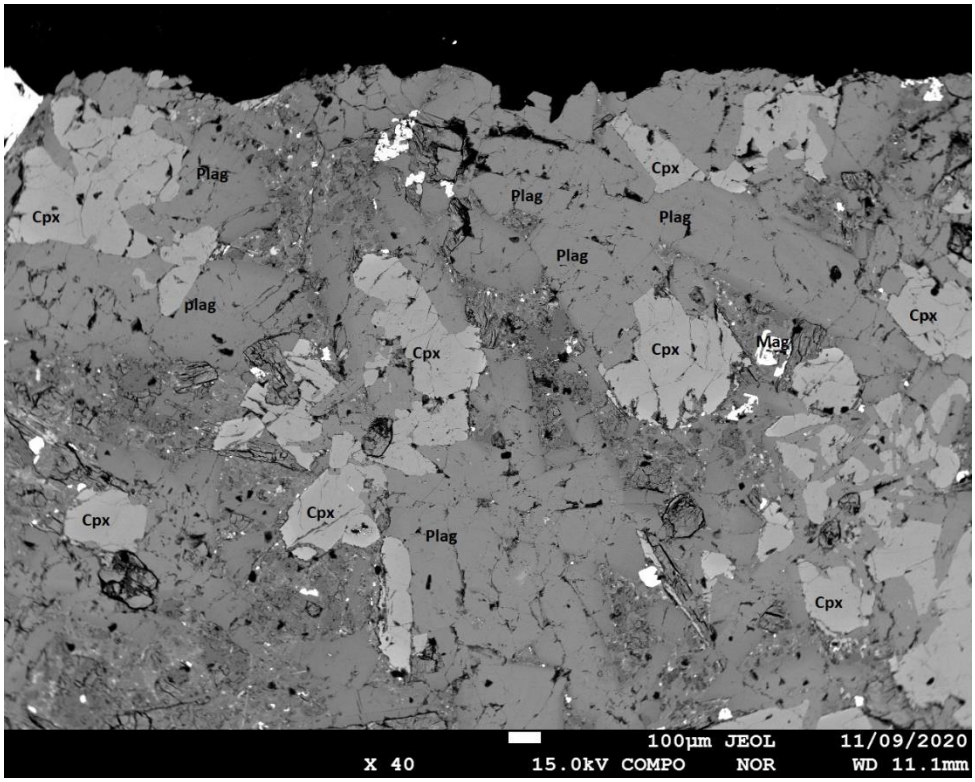

Figure 4-12: Backscatter electron image of TAN1213 10-8 showing texture, grainsize, and minerals present

Mineral abbreviations from Whitney and Evans (2010)

4.1.4 TAN1213 10-10

In hand sample TAN1213 10-10 is medium to coarse grained and is a grey-brown in colour (Figure 4-13). Grainsize ranges from ~0.5-2 mm and the sample has a mesocumulate to orthocumulate texture (Figure 4-14). The crystal assemblage consists of ~60% plagioclase, ~25% clinopyroxene, ~3% magnetite, and ~12% intercumulus material. TAN1213 10-10 was the most poorly preserved sample of the study and consequently the observations and geochemical data gathered are limited compared to the other three samples.

The plagioclase crystals are euhedral to subhedral, tabular, and range in size from ~0.5-1mm (Figure 4-14). As with the other samples no signs of compositional zoning or disequilibrium textures such as sieve textures and oscillatory zoning were observed.

The clinopyroxene crystals are subhedral to euhedral, long, and tabular in shape, and range in size from ~0.3-0.5 mm (Figure 4-14). No compositional zoning was observed.

The magnetite crystals are subhedral to euhedral, tabular, and range in size from ~0.2-0.5 mm (Figure 4-15)

Figure 4-13: Cut block hand sample of TAN1213 10-10 showing colour, texture, and grainsize

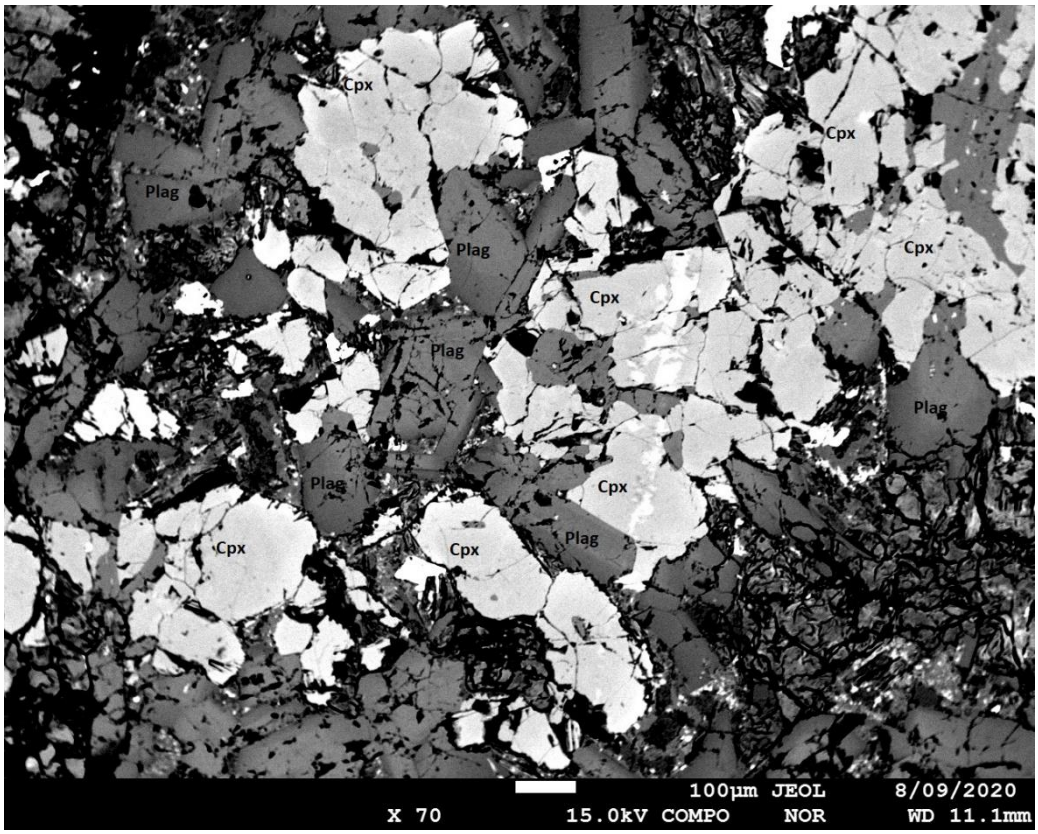

Figure 4-15: Backscatter electron image of TAN1213 10-10 showing texture, grainsize, and minerals present

Mineral abbreviations from Whitney and Evans (2010)

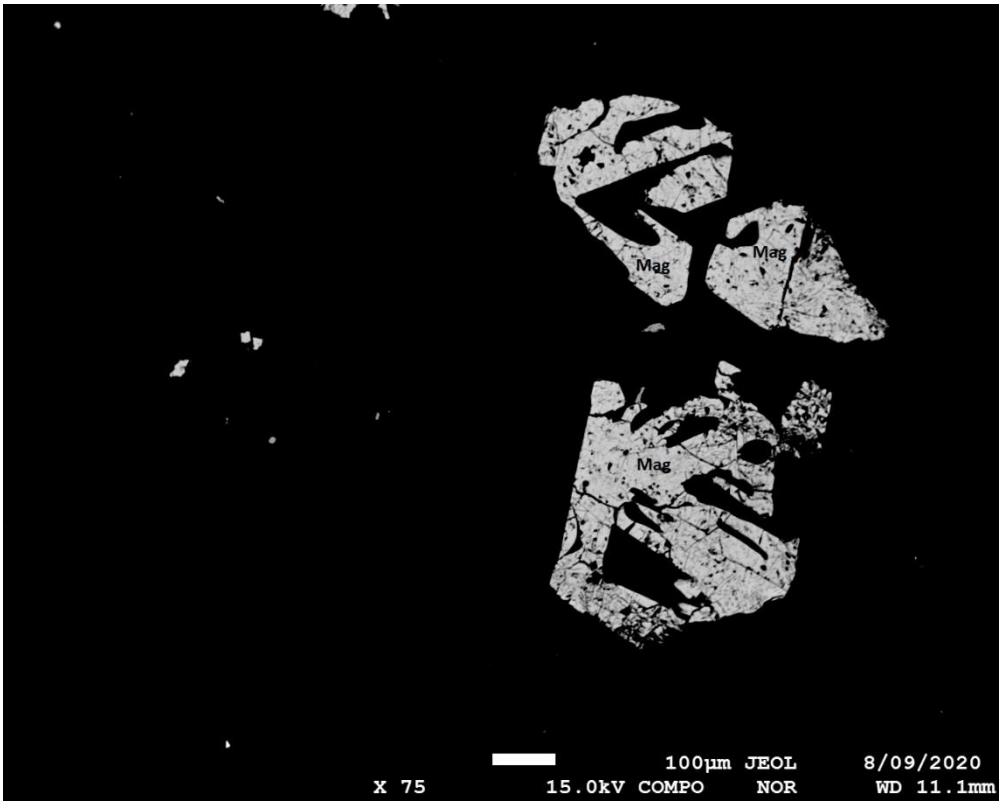

Figure 4-14: Backscatter electron image of magnetite from TAN1213 10-10

In summary all four samples are crystalline granular and have mesocumulate to orthocumulate textures with grainsize ranging from ≤0.5 mm to ≤2 mm. The major mineral assemblage is clinopyroxene + plagioclase + magnetite with these minerals having euhedral to subhedral crystals. The intercumulus material consists of more evolved minerals and is composed of varying proportions of quartz ± plagioclase ± amphibole ± orthoclase. Also present in the samples is trace amounts of ilmenite, apatite, and chalcopyrite. Both intercumulus material and the trace minerals have anhedral crystals (e.g. Figures 4-8 and 4-9).

Table 4-2: Summary of mineral parameters used to classify the selected samples.

Sample#	**Grainsize**	**Plag vol%**	**Qtz+Af vol%**	**Mafic Minerals***	**Lithology****
TAN1213 10-1	Fine (<1mm)	55-60%	10%	Cpx and Mag	Gabbro
TAN1213 10-7	Coarse (≤2mm)	55-60%	10%	Cpx, Mag, (Ap and Amp)	Gabbro
TAN1213 10-8	Medium/Coarse (1-2mm)	55-60%	10%	Cpx and Mag	Gabbro
TAN1213 10-10	Medium/Coarse (1-2mm)	50-60%	10%	Cpx and Mag	Gabbro

**Trace minerals are in brackets*

***based on Streckeisen QAPF classification (Figure 1-2)*

4.2 Mineralogy

Plagioclase, clinopyroxene, Fe-Ti oxides, and amphibole were analysed for major element compositions and the data are presented in Appendix 1 with representative analyses summarised in Tables 4-3 to 4-10. All the analyses are of cumulus crystals, apart from amphibole, which only occurred as an intercumulus mineral.

4.2.1 Plagioclase

Plagioclase is the most abundant mineral phase of the samples making up 50-60 vol% of minerals that are present in the samples. The anorthite (An) content of the plagioclase in the samples range from andesine to bytownite (Figures 4-16 to 4-19), An_{31}-An_{88}, and have orthoclase (Or) contents ranging from $Or_{0.1}$-Or_5. Table 4-3 presents the average composition of cores and rims from plagioclase samples. A majority of individual plagioclase crystals are relatively unzoned, with An content difference of ≤10 mol% from core-rim, however 4 crystals do show variations in An content greater than 10 mol% from core-rim with rims being more sodic. One crystal from 10-8 does exhibits higher An content on the rim compared to the core (~75 vs. ~67 mol%) (See Appendix 1).

Table 4-3: Average plagioclase core and rim major element measurements from each sample

TAN1213 10-1	Average Core (n=5)	2SD	Average Rim (n=5)	2SD
SiO2	53.50	3.1	54.70	2.7
TiO2	0.02	0.021	0.02	0.019
Al2O3	29.00	1.9	28.20	1.6
FeO	0.90	0.27	0.85	0.11
MnO	0.01	0.016	0.01	0.011
MgO	0.09	0.064	0.07	0.051
CaO	12.10	2.5	11.00	2.2
Na2O	4.41	1.3	4.99	1.1
K2O	0.13	0.092	0.17	0.066
Cr2O3	0.01	0.013		
Total	100.00	0.59	100.00	0.56
An	59.80	12	54.40	10
Ab	39.50	12	44.60	9.8
Or	0.78	0.55	0.98	0.39
TAN1213 10-7	Average Core (n=5)	2SD	Average Rim (n=5)	2SD
SiO2	49.60	3.2	54.70	6.3
TiO2	0.02	0.012	0.03	0.0099
Al2O3	29.50	9.7	28.40	4.1
FeO	2.03	4.4	0.86	0.44
MnO	0.01	0.049	0.01	0.012
MgO	0.70	2.3	0.06	0.058
CaO	13.70	7.3	11.00	4.9
Na2O	3.00	1.7	4.88	2.4
K2O	0.09	0.094	0.19	0.17
Cr2O3	0.01	0.018	0.01	0.015
Total	98.60	8.3	100.00	0.73
An	70.00	25	54.80	24
Ab	29.40	24	44.00	23
Or	0.59	0.86	1.11	1

TAN1213 10-8	Average Core (n=6)	2SD	Average Rim (n=6)	2SD
SiO2	51.70	6.3	53.30	9.7
TiO2	0.02	0.018	0.02	0.02
Al2O3	30.40	4.2	29.40	6.3
FeO	0.83	0.24	0.79	0.26
MnO	0.01	0.017	0.01	0.018
MgO	0.09	0.054	0.09	0.098
CaO	13.50	4.9	12.30	7.6
Na2O	3.68	2.5	4.28	3.9
K2O	0.11	0.096	0.14	0.19
Cr2O3	0.01	0.017		
Total	100.00	0.79	100.00	0.67
An	66.50	23	60.80	37
Ab	32.90	23	38.40	36
Or	0.62	0.57	0.84	1.1
TAN1213 10-10	Average Core (n=4)	2SD	Average Rim (n=3)	2SD
SiO2	52.30	9.1	51.50	9.6
TiO2	0.02	0.031	0.03	0.054
Al2O3	30.10	6.1	30.70	6.9
FeO	0.86	0.47	0.98	0.29
MnO	0.00	0.012	0.02	0.026
MgO	0.08	0.073	0.07	0.071
CaO	13.00	7.5	13.80	7.9
Na2O	3.95	4	3.58	4.1
K2O	0.13	0.18	0.12	0.18
Cr2O3				
Total	100.00	0.6	101.00	1.2
An	64.00	37	67.40	37
Ab	35.30	36	31.80	36
Or	0.76	1.1	0.73	1

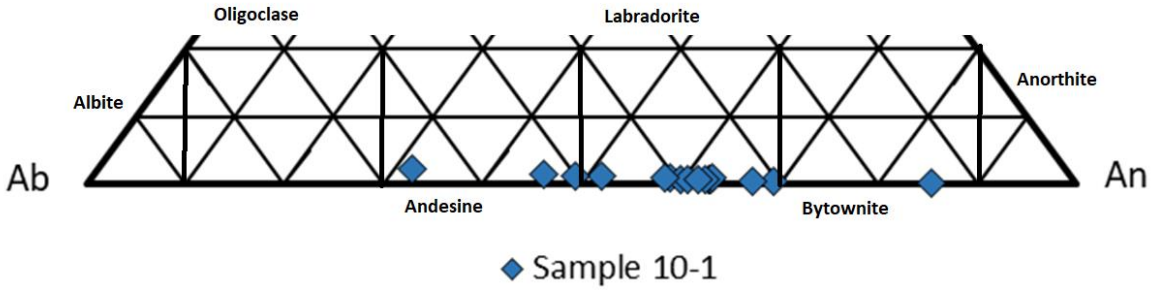

Figure 4-16: Plagioclase compositions for sample TAN1213 10-1

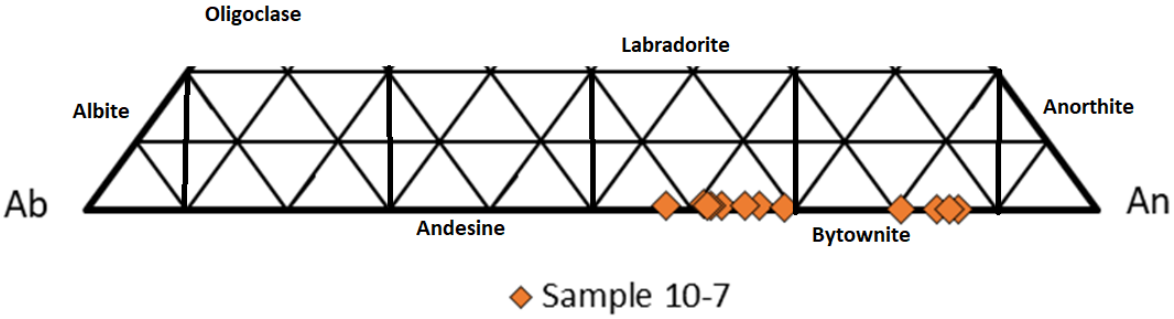

Figure 4-17: Plagioclase compositions for sample TAN1213 10-7

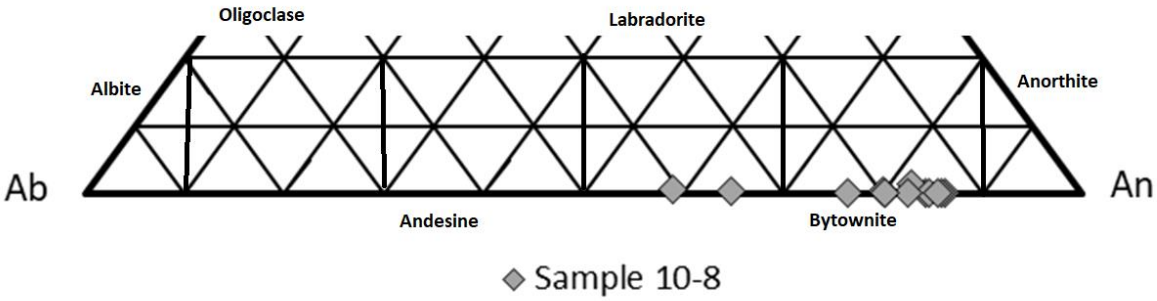

Figure 4-18: Plagioclase compositions for sample TAN1213 10-8

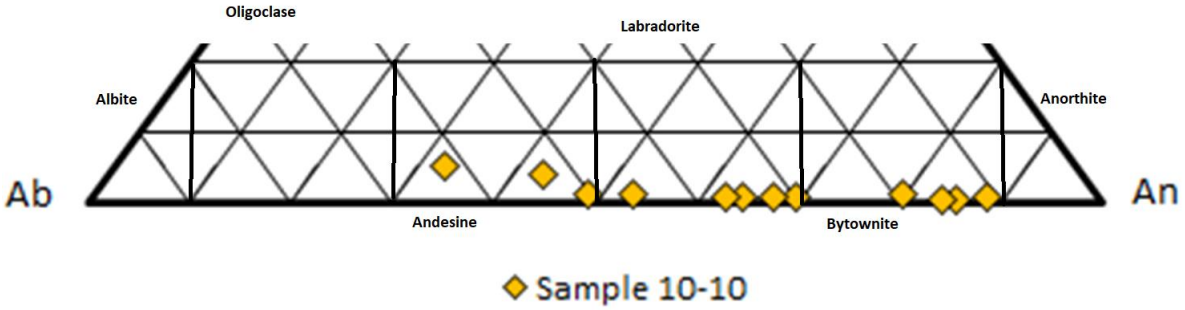

Figure 4-19: Plagioclase compositions for sample TAN11213 10-10

4.2.2 Clinopyroxene

Clinopyroxene comprises ~20 vol% of the crystals present in the samples. The clinopyroxene crystals within the samples have compositions that fall in the ranges of $En_{30-47}Wo_{29-44}Fs_{9-30}$ and are all within the augite classification field (Figure 4-20). Table 4-4 presents the average major element compositions for the clinopyroxene crystals from all samples. The clinopyroxene Mg#s range from 53-81 with most of the lower Mg# clinopyroxenes (Mg# 53-70) and hence more evolved crystals being found in Sample 10-1 (see Figure 4-20 and Appendix A.1 Table A-3 and A-4).

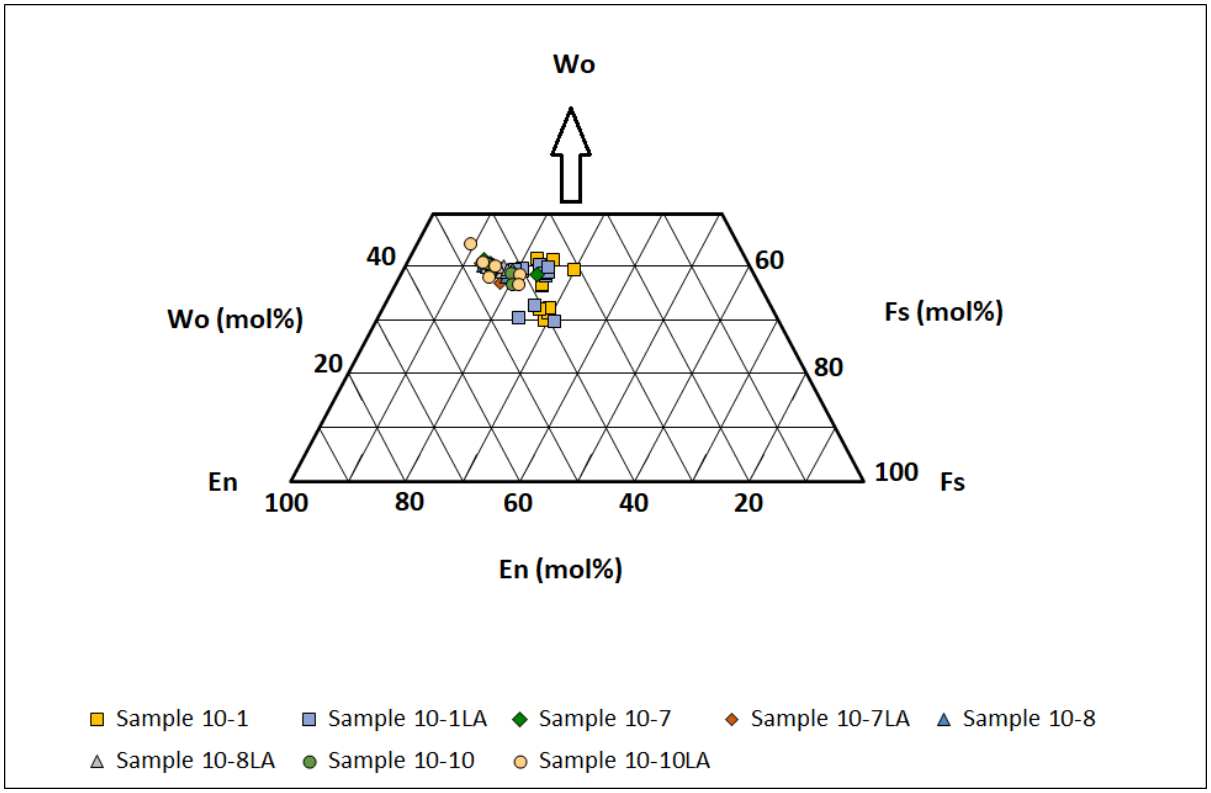

Figure 4-20: Plot of clinopyroxene analyses

Wo, En, and Fs represent Wollastonite, Enstatite, and Ferrosilite. The LA after sample name indicates clinopyroxenes samples that were selected for further trace element analysis using Laser Ablation

Table 4-4: Average major element compositions of clinopyroxene crystals from all samples

TAN1213 10-1	Average (n=10)	2SD		**TAN1213 10-7**	Average (n=9)	2SD
SiO2	51.00	0.58		**SiO2**	52.40	1.20
TiO2	0.47	0.17		**TiO2**	0.35	0.10
Al2O3	1.98	1.00		**Al2O3**	2.14	0.46
Fe2O3	2.05	0.86		**Fe2O3**	2.02	0.87
FeO	14.60	4.20		**FeO**	8.66	3.90
MnO	0.46	0.16		**MnO**	0.28	0.12
MgO	13.10	2.30		**MgO**	15.60	2.20
CaO	17.30	4.10		**CaO**	19.60	1.30
Na2O	0.19	0.05		**Na2O**	0.21	0.07
K2O				**K2O**		
Cr2O3				**Cr2O3**	0.02	0.05
Total	101.00	0.77		**Total**	101.00	1.10
Wo	35.90	8.60		**Wo**	39.50	1.90
En	37.60	6.30		**En**	43.90	5.10
Fs	26.50	6.20		**Fs**	16.50	6.50
TAN1213 10-8	Average (n=7)	2SD		**TAN1213 10-10**	Average (n=5)	2SD
SiO2	52.50	1.20		**SiO2**	52.50	1.20
TiO2	0.35	0.11		**TiO2**	0.35	0.12
Al2O3	2.09	0.58		**Al2O3**	2.07	0.60
Fe2O3	1.92	0.76		**Fe2O3**	1.99	1.00
FeO	8.38	2.10		**FeO**	8.91	2.90
MnO	0.28	0.07		**MnO**	0.30	0.16
MgO	15.90	1.10		**MgO**	15.80	1.20
CaO	19.60	1.10		**CaO**	19.30	1.70
Na2O	0.20	0.04		**Na2O**	0.22	0.05
K2O				**K2O**		
Cr2O3	0.02	0.04		**Cr2O3**	0.02	0.03
Total	101.00	1.00		**Total**	101.00	0.39
Wo	39.40	2.00		**Wo**	38.90	3.00
En	44.70	2.60		**En**	44.20	2.90
Fs	15.90	4.20		**Fs**	16.90	5.60

*Total values may exceed 100 wt% due to rounding of data for presentation.

4.2.3 Fe-Ti Oxides

The Fe-Ti oxides range in size up to 0.5 mm and are randomly distributed throughout the samples. Most samples had ~3% oxides, except TAN1213 10-1 with ~5%. All analysed grains were magnetite. The magnetite crystals are characterised by 45-48 wt.% FeO, 25-33 wt.% Fe_2O_3 (determined by charge balance), and 16-20 wt.% TiO_2. Table 4-5 presents average Fe-Ti oxide compositions from all samples.

4.2.4 Amphiboles

Amphiboles were only observed in one sample, TAN1213 10-7, where they were a minor component of the intercumulus material. Three amphibole crystals were identified and sufficiently large to be analysed using EPMA. The amphibole compositions were classified using the Excel spreadsheet of Locock (2014), following the 2012 classification scheme of Hawthorne et al. (2012). All three amphiboles are hastingsite, with the core of one crystal being classified as Ti-rich hastingsite (see Appendix 1).

Table 4-5: Average major element compositions for Fe-Ti oxides from all samples

TAN1213 10-1	Average (n=20)	2SD		**TAN1213 10-7**	Average (n=6)	2SD
TiO2	18.00	0.61		**TiO2**	18.30	3.11
Al2O3	1.89	0.25		**Al2O3**	1.35	1.34
FeO	46.30	1.04		**FeO**	46.30	1.40
Fe2O3	28.30	1.33		**Fe2O3**	29.20	6.29
MnO	1.08	0.91		**MnO**	1.15	1.98
MgO	0.13	0.06		**MgO**	0.39	0.46
Cr2O3	0.03	0.02		**Cr2O3**	0.02	0.02
V2O3	2.44	0.12		**V2O3**	2.39	0.29
Total	98.20	0.93		**Total**	99.10	2.55
TAN1213 10-8	Average (n=4)	2SD		**TAN1213 10-10**	Average (n=6)	2SD
TiO2	19.00	1.47		**TiO2**	18.60	2.43
Al2O3	1.78	0.30		**Al2O3**	1.06	0.71
FeO	47.90	1.67		**FeO**	46.50	1.16
Fe2O3	27.10	3.26		**Fe2O3**	28.70	5.29
MnO	0.46	0.10		**MnO**	1.22	1.88
MgO	0.33	0.22		**MgO**	0.29	0.13
Cr2O3	0.03	0.03		**Cr2O3**	0.02	0.02
V2O3	2.50	0.11		**V2O3**	2.42	0.19
Total	99.20	2.00		**Total**	98.80	2.64

4.3 Clinopyroxene Trace Elements Compositions

Trace element data for 30 clinopyroxenes are presented in Appendix 2. Trace element profiles reflect a combination of the trace element composition of the liquid they crystallised from and the relative compatibility or incompatibility of each element in the clinopyroxene lattice.

NMORB normalised trace element patterns of clinopyroxenes from all four samples are generally subparallel and show variable depletions in high field strength elements (HFSE) (Nb, Ti, Zr, and Hf), and Sr and Pb (Figures 4-21 to 4-24). Uranium and Ba, however, are significantly more variable with some samples showing enrichments in these elements while others show depletions (Figures 4-21 to 4-24). The relative Sr depletion can be measured as a Sr anomaly, Sr/Sr* which is quantified by the equation:

$$\text{Sr/Sr*}=SrN/\sqrt{(PrN \times NdN)}$$

where *N=NMORB normalised concentration of element.*

The Sr/Sr* decreases systematically with clinopyroxene Mg# (Figure 4-25).

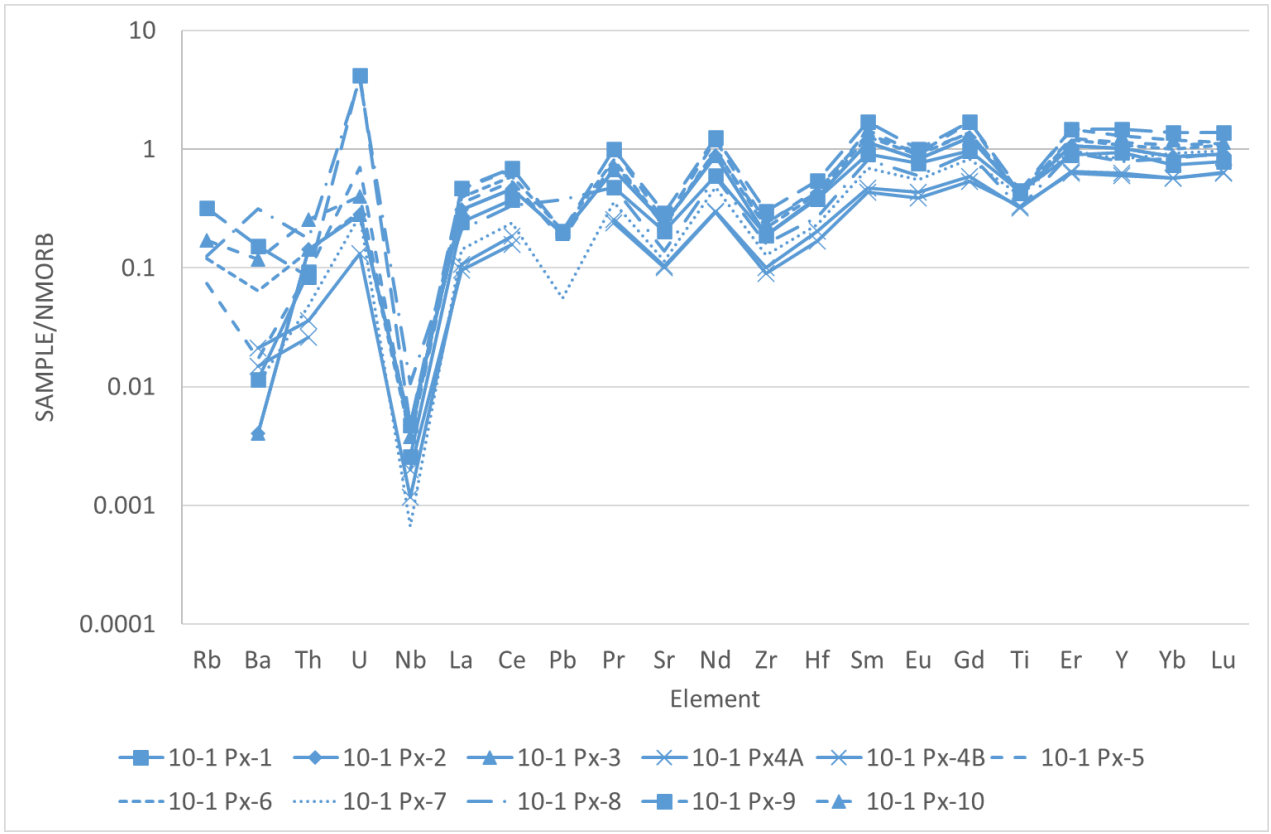

Figure 4-21: NMORB normalised trace element patterns from clinopyroxenes in sample TAN1213 10-1 NMORB values from Sun and McDonough (1989)

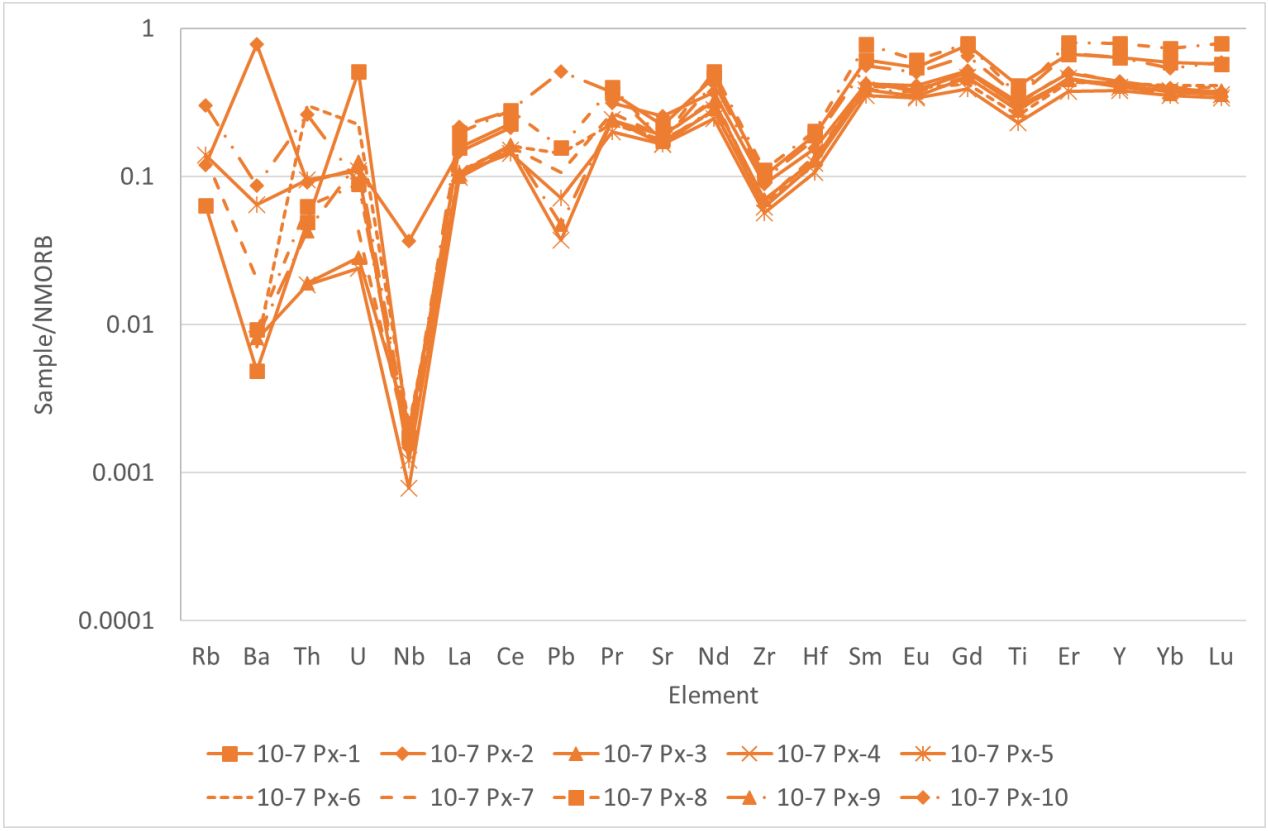

Figure 4-22: NMORB normalised trace element patterns from clinopyroxenes in sample TAN1213 10-7. NMORB values from Sun and McDonough (1989)

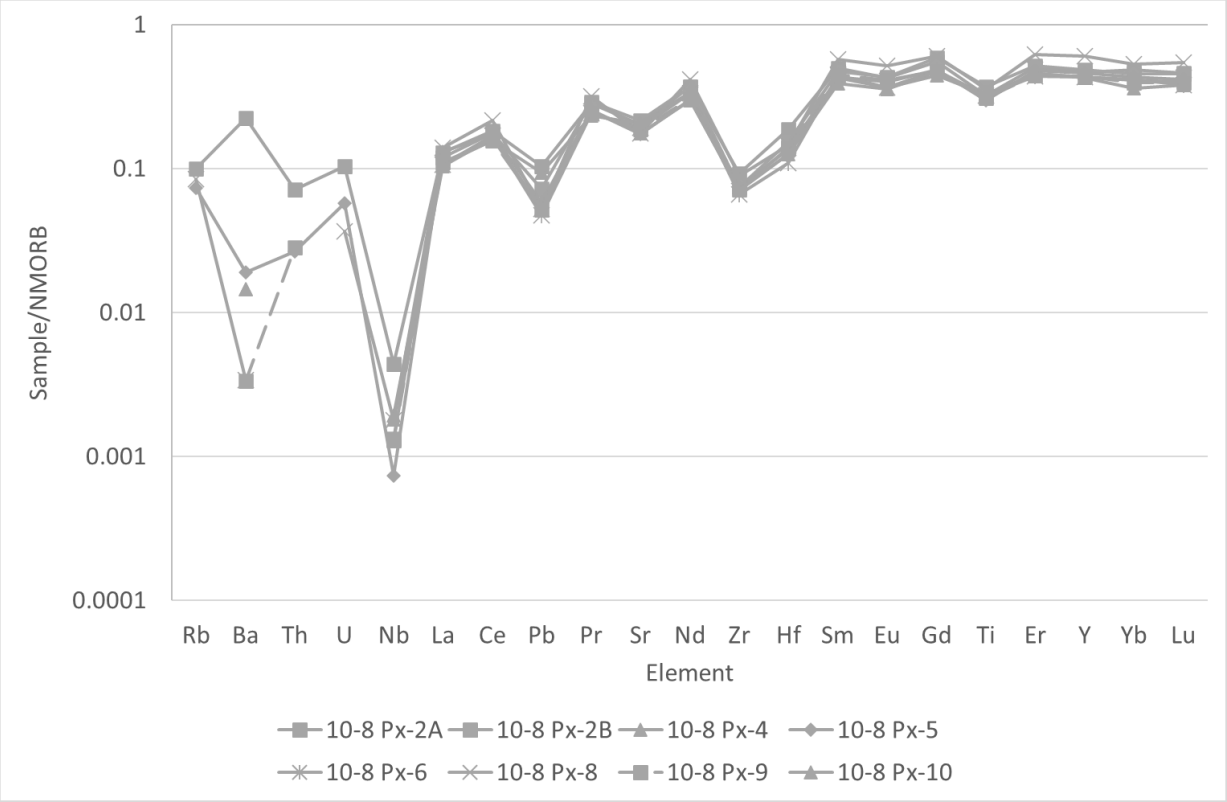

Figure 4-23: NMORB normalised trace element patterns from clinopyroxenes in sample TAN1213 10-8 NMORB values from Sun and McDonough (1989)

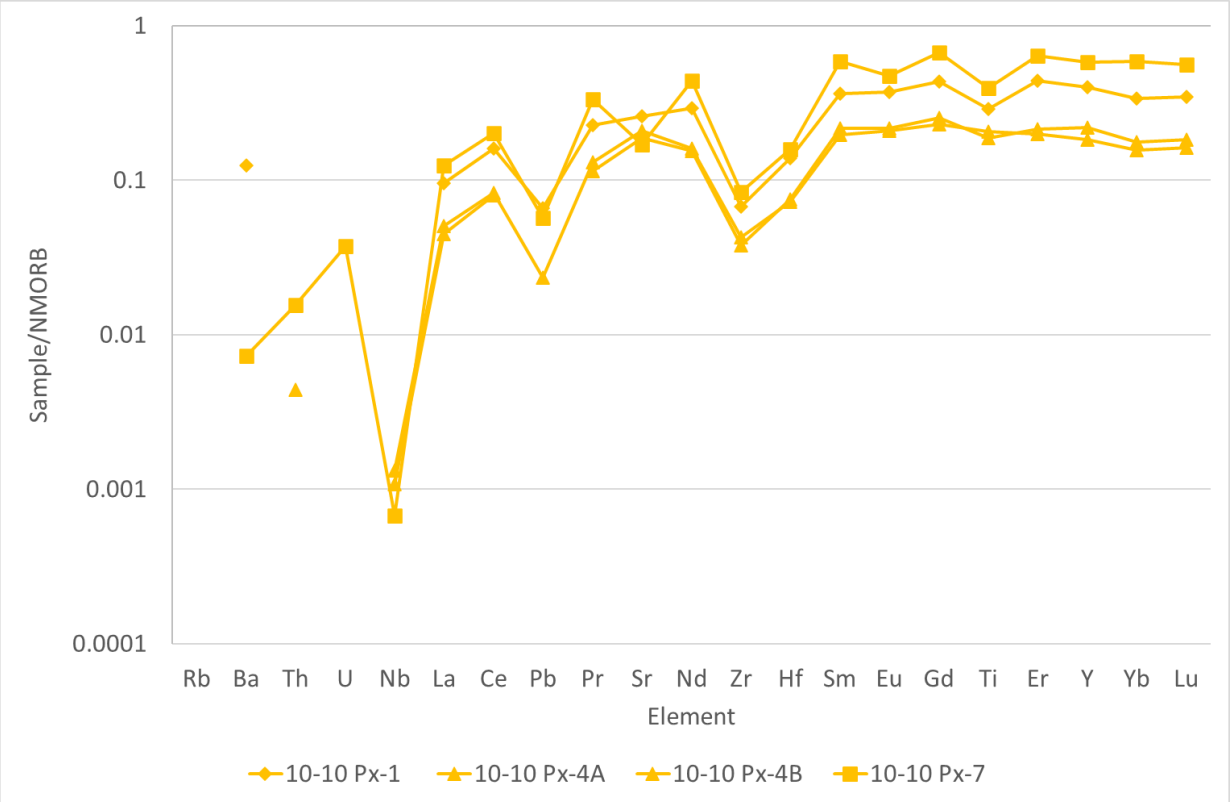

Figure 4-24: NMORB normalised trace element patterns from clinopyroxenes in sample TAN1213 10-10 NMORB values from Sun and McDonough (1989)

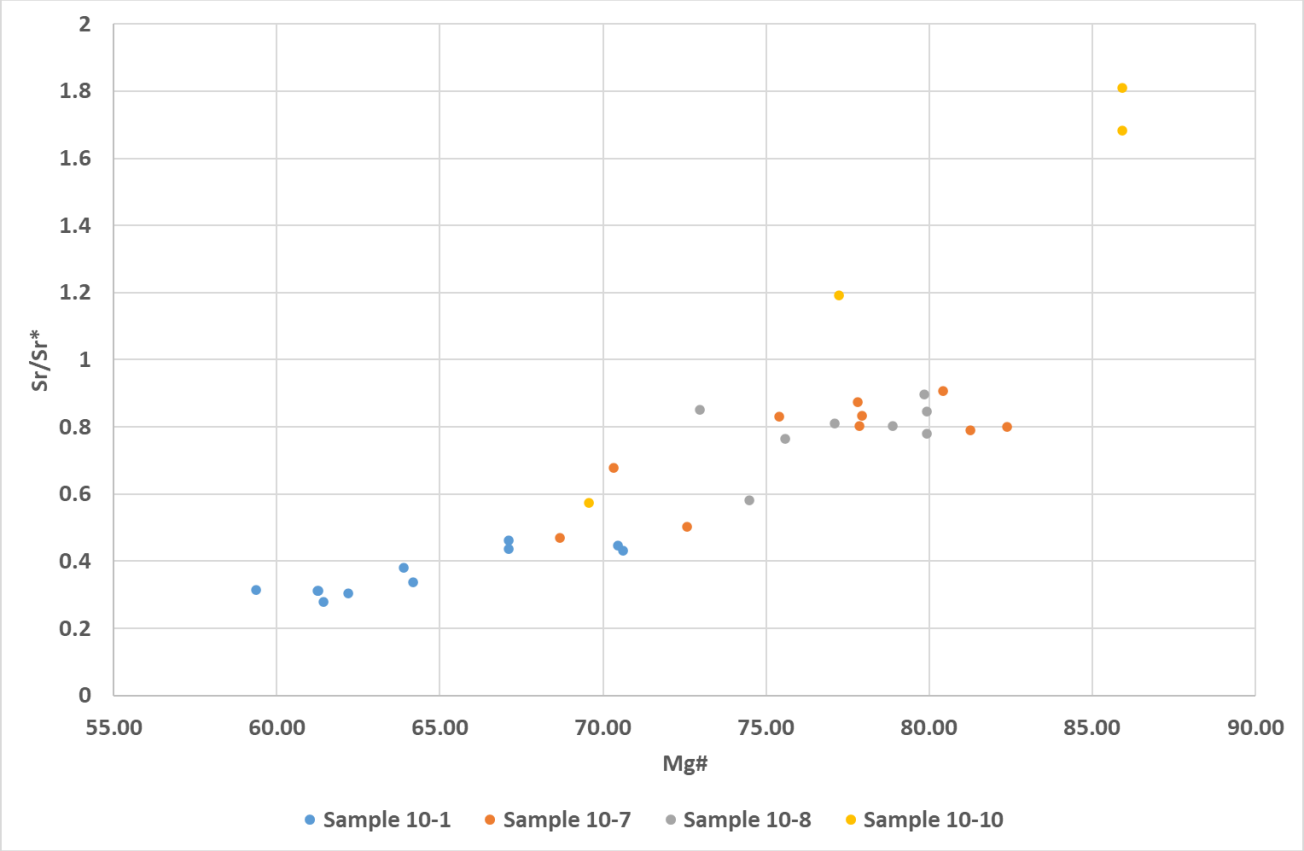

Figure 4-25: Sr/Sr vs. Mg# for clinopyroxenes from all samples*

Clinopyroxene chondrite normalised rare earth element (REE) patterns are all light-(L)REE depleted (Figures 4-26 to 4-29). Most clinopyroxene grains analysed have a negative Eu anomaly, the size of which varies from crystal to crystal (Figures 4-26 to 4-29). The Eu anomaly (Eu/Eu*) can be quantified using the equation:

$$\text{Eu/Eu*} = EuN/\sqrt{(SmN \times GdN)}$$

Where *N= the chondrite normalised element concertation.*

The clinopyroxene grains show a consistent trend of increasingly negative Eu anomalies with decreasing Mg# (Figure 4-30).

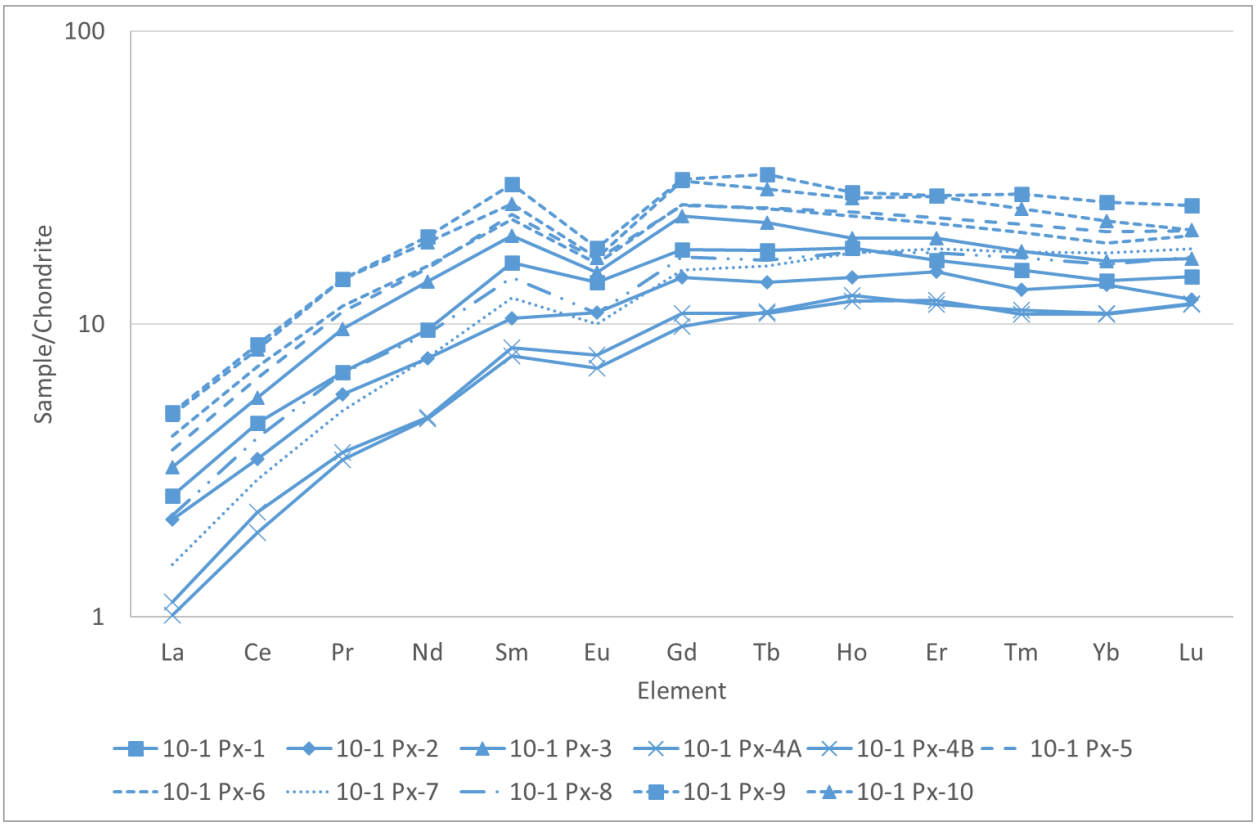

Figure 4-26: Chondrite normalised REE patterns from clinopyroxenes in sample TAN1213 10-1. Chondrite values from McDonough and Sun (1995)

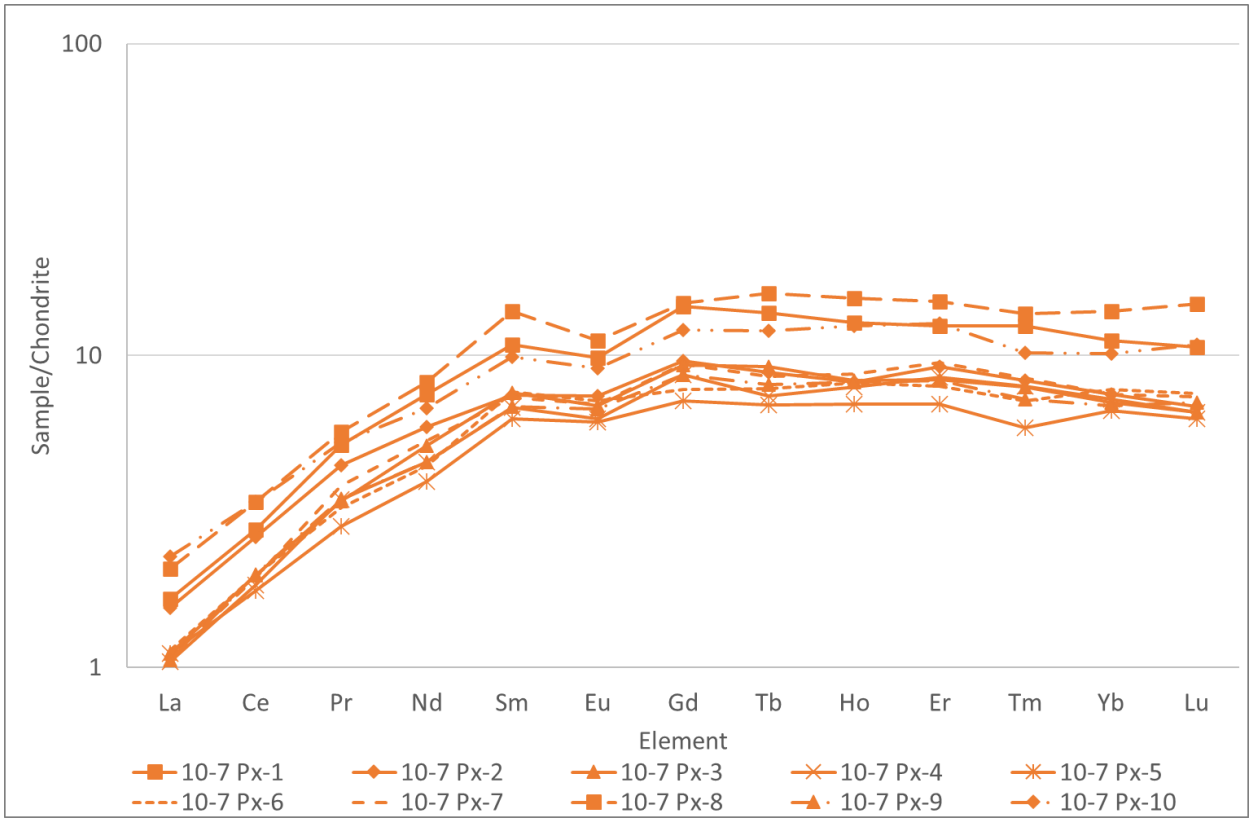

Figure 4-27: Chondrite normalised REE patterns from clinopyroxenes in sample TAN1213 10-7. Chondrite values from McDonough and Sun (1995)

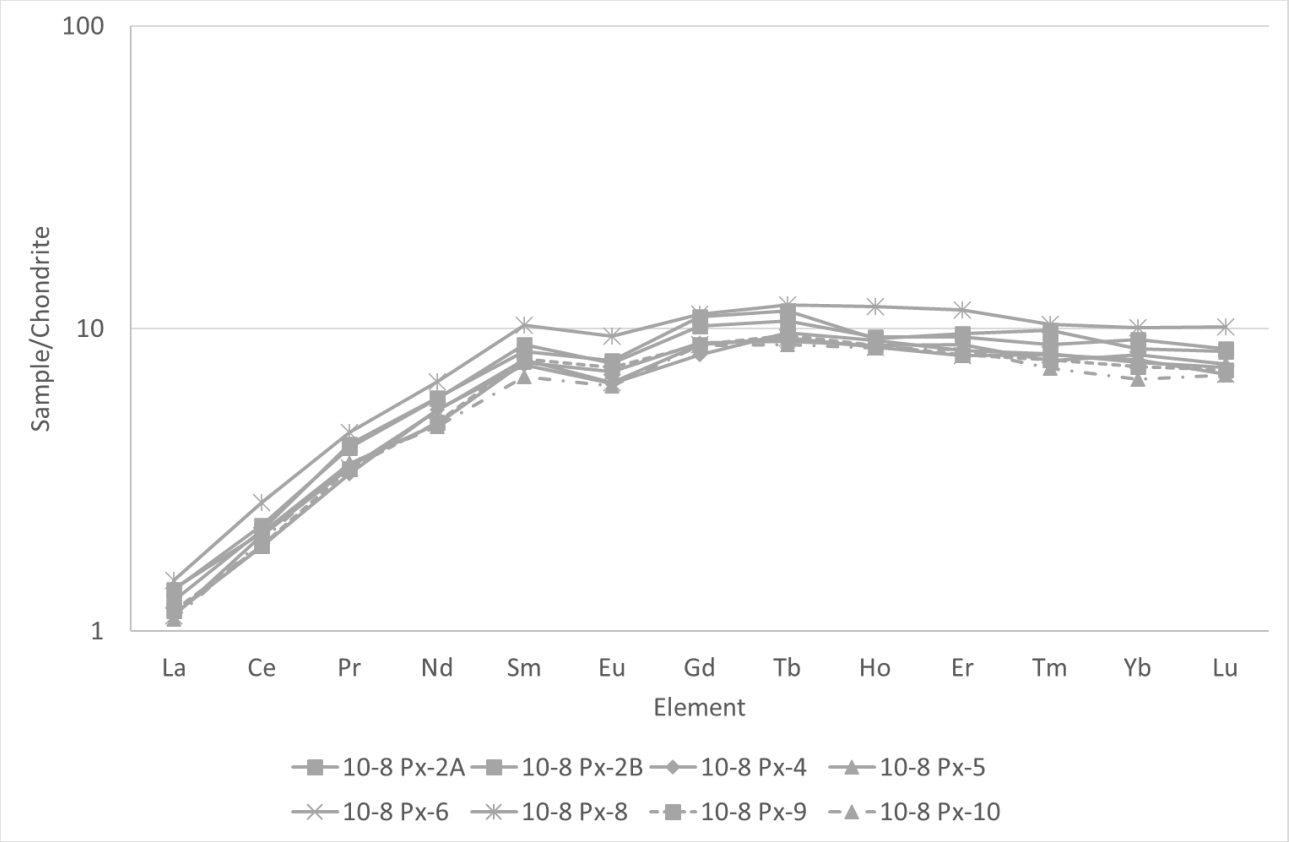

Figure 4-28: Chondrite normalised REE patterns from clinopyroxenes in sample TAN1213 10-8. Chondrite values from McDonough and Sun (1995).

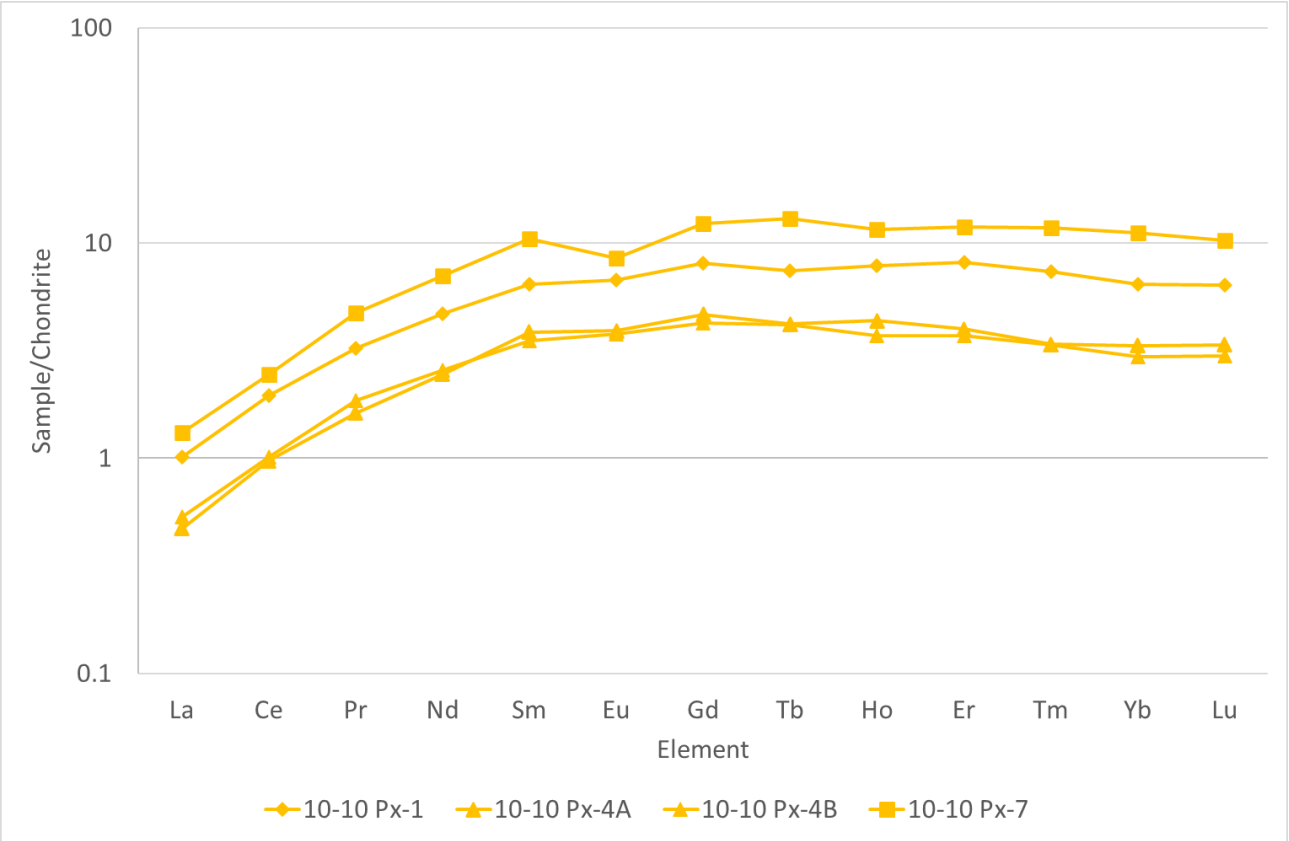

Figure 4-29: Chondrite normalised REE patterns from clinopyroxenes in sample TAN1213 10-10. Chondrite values from McDonough and Sun (1995)

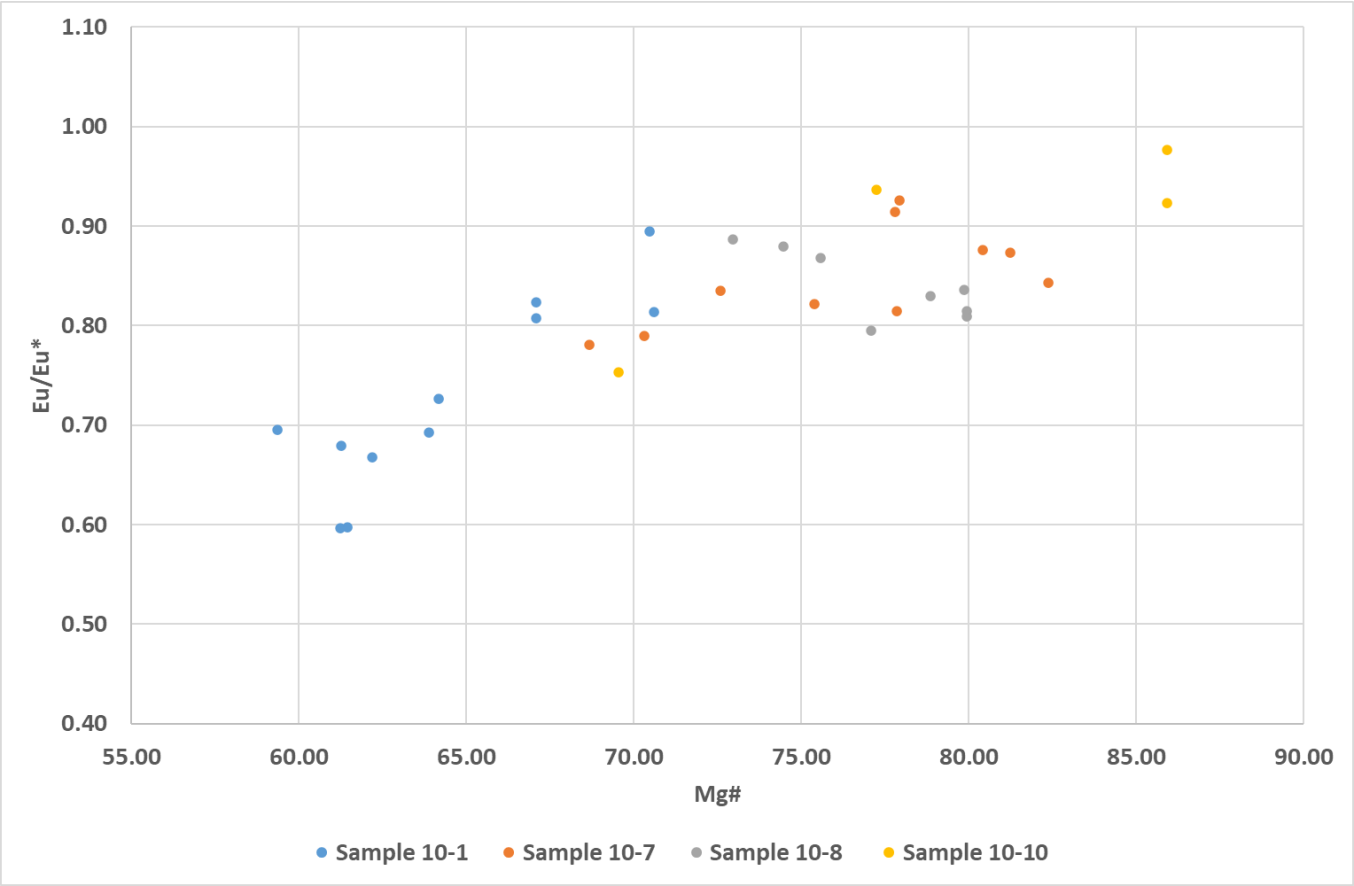

Figure 4-30: Eu/Eu* vs. Mg# for clinopyroxenes from all samples

4.4 Crystallisation Conditions

The ability to estimate the temperature, pressure, oxygen fugacity ($f O_2$), and H_2O contents at the time of crystallisation, is dependent on the minerals present in the samples. Unfortunately, the absence of ilmenite (two-oxide thermometry), orthopyroxene (two-pyroxene thermometers) and glass (pyroxene-liquid thermometers) in the sample suite limits the range of geothermobarometers that can be applied.

Temperatures were estimated using the magnetite geothermometer of Canil and Lacourse (2020) which requires Mg and Fe^{Total} from magnetite to estimate the temperature of the samples, rather than the traditional two Fe-Ti oxide thermo-oxybarometry (e.g., Ghiorso and Evans, 2008). Table 4-11 presents the minimum and maximum temperature estimates (±50°C) calculated for the samples of this study. Sample TAN1213 10-1 exhibits lower minimum and maximum temperatures than the other samples but there is overlap between magnetite temperatures of all samples.

Table 4-6: Temperature estimates for samples using magnetite.

Sample Name	**Temperatures (min-max, °C)**
TAN1213 10-1 (n=20)	499-671
TAN 1213 10-7 (n=6)	553-756
TAN1213 10-8 (n=4)	540-755
TAN1213 10-10 (n=6)	553-747

Sample TAN1213 10-7 contained rare amphibole, which can also be used to estimate some of the variables that are associated with crystallising conditions. The variables of temperature, H_2O content, pressure were calculated based on the method of Ridolfi et al., (2010) using the program WinAmptb (Yavuz and Döner, 2017). The variable estimates are presented in Table 4-12.

Table 4-7: Temperature, Pressure, Depth, and H2O content of amphibole samples

Amphibole	**Temperature °C***	**Pressure (MPa)***	**Amphibole Crystallisation Depth (km)***	**H_2O content (%)***
1 Rim	832	190	5.48	7.14
1.2 Core	861	197	5.71	7.14
2 Core	744	92	2.66	6.21
2.1 Rim	755	88	2.53	5.93
2.1 Rim	747	88	2.56	6.58
3 Core	798	120	3.46	6.46

The uncertainties for each variable are:Temperature (±22°C) Pressure and Depth (24%) and H_2O content (up to 15%) (Ridolfi et al., 2010).

Chapter 5 Discussion

The key research questions for this study involve constraining the petrogenesis of the samples and what they represent in respect to the overall KAHT magmatic system. The samples were obtained from a seafloor dredge and therefore they come from a spatially limited area, specific stratigraphic context is lacking. The following sections examine 1) the relationships between the samples, 2) the petrographic and mineralogical constraints on the crystallisation environment, and 3) evidence for their tectono-magmatic association and how they relate to previously studied eruptive material.

5.1 Petrographic and Mineralogical Constraints on Formation Conditions

Four representative samples in this study were selected to represent the range of textures that were present in the overall suite of 10 samples, where the primary difference is grainsize (Section 4.1). The absence of glass, vesicles, and the mesocumulate and orthocumulate texture (Section 4.1) of the samples are consistent with a plutonic origin, crystallising within the crust. The four samples are all gabbroic (Section 4.1) and are characterised by the mineral assemblage of plagioclase > clinopyroxene > magnetite with minor quartz, more sodic plagioclase, and K-feldspar. Orthopyroxene and ilmenite were not observed in any of the samples. Amphibole was only observed in sample TAN1213 10-7 which has the largest grainsizes of the samples at ≤2mm. The mesocumulate and orthocumulate texture of the samples are best exemplified in the three coarser grained samples (grainsizes between 1-≤2mm), and TAN1213 10-7 provides the best example of the texture (Section 4.1). The orthocumulate texture is less clear in the finer grained sample TAN1213 10-1 (grain size ≤1mm) but it is still present (Section 4.1.1 and Figures 4-2 to 4.4).

The four samples all exhibit similar mineral assemblages and textures, indicating that they all formed in a similar environment. The relatively large, euhedral crystals of plagioclase, clinopyroxene, and magnetite (Figures 4-2 to 4-15) likely represent early crystallising phases that grew in a slow-cooling environment such as within a magma chamber. As discussed in Chapter 1, mesocumulate and orthocumulate textures are interpreted to form in environments where the melt has cooled slowly (Wager et al., 1960). The intercumulus melt would thus have had limited interactions with the melt in the main

chamber and the only interaction that this later stage liquid had was with the large euhedral plagioclase crystals which can be seen by the presence of thin (<0.1 mm) Na-rich rims on some plagioclase (Section 4.1.2 and Figure 4-8).

Plagioclase textures (Section 4.2.1) can be used to evaluate if there were any change in the magmatic conditions under which the minerals grew and whether the crystals formed in equilibrium with the melt. The plagioclase crystals in the samples show no evidence of disequilibrium textures, such as sieve textures or oscillatory zoning, which suggests that the magmatic conditions varied little during formation and/or that the samples cooled sufficiently slowly to allow diffusion to homogenise any zoning in the cumulate plagioclase. A lack of disequilibrium textures further supports the interpretation that these samples formed in a closed environment, such as a magma chamber.

Pressure and temperature estimates are limited due to the restricted mineral assemblages present in the samples. Temperature estimates from magnetite have been determined from all four samples in the study suite. The thermometer used has uncertainties of ± 50°C and is calibrated for a temperature range of 700-1050°C (Canil and Lacourse, 2020). The coarser grained samples (TAN1213 10-7, 10-8, and 10-10) indicate magnetite formation temperatures that are indistinguishable given the uncertainties and range from within the calibrated temperature range to below this (~540-760°C). By contrast the finer grained sample, TAN1213 10-1, gives overlapping but consistently lower temperatures (~500-670°C). Amphiboles from sample 10-7 were also used to provide temperature estimates. The thermometer used was calibrated over a temperature range of 550-1120°C with uncertainties of ± 22°C (Ridolfi et al., 2010). The temperature range estimates of the amphiboles were ~745-860°C which overlaps with the higher temperatures from the magnetite from TAN1213 10-7 and the other coarser grained samples. Application of the magnetite thermometer to natural samples however, has shown that lower temperatures may be recorded in plutonic rocks due to slow cooling (Canil and Lacourse, 2020). Thus, the magnetite temperatures may be considered to be minimum temperatures and not directly comparable to the amphibole temperatures in these slow cooling plutonic samples. Given these limitations and considering the textural information, it is most likely that the coarser grained samples (TAN1213 10-7, 10-8, 10-10) crystallised at broadly similar

temperature conditions (~700-800°C), whereas the finer grained sample (TAN1213 10-1) represents a lower temperature melt that cooled more rapidly.

Pressure and the associated depth estimates were determined from the amphibole crystals that were present in sample TAN1213 10-7, this is the first limitation of these estimates as they only come from one sample in the study suite. The barometer used to estimate pressures was calibrated for pressures of <1200 MPa and has uncertainties of 24% for crystal-rich magmas (Ridolfi et al., 2010). Pressure estimates of the amphiboles range from 90-200 MPa which is equivalent to depths of ~3-6 km, based on lithospheric pressure (crustal density of 2.89 g/cm^3). The crustal thickness through the eastern KAHT has been estimated using seismic reflection profiles. The MANGO 1 and MANGO 2 seismic reflection lines which encompasses the southern Kermadec Arc (~34°S and ~37°S) indicate a crustal thickness of 6-7 km in the eastern back-arc (Bassett et al., 2016). The study sample were dredged from a location that lies between these two seismic reflection lines (Figure 5-1), the seismic reflection crustal thickness profile combined with the pressure/depth estimates from the amphibole chemistry indicates that the samples most likely come from the mid to lower crust.

The exposure of mid-lower crustal samples on the seafloor may have been facilitated by one of two distinct mechanisms: 1) tectonic emplacement by faulting, or 2) as xenoliths incorporated in eruptive material. Exposure of mid-lower crustal material would require large crustal to lithospheric-scale faults. The samples were dredged from the NW face of a sharp ridge in Basin E (Section 2.5 and Figure 2-4), this ridge is orientated NE-SW which follows the regional tectonic fabric of the eastern back-arc (Pullan, 2018, Wysoczanski et al., 2010) indicating a close spatial association of the samples and fault activity. Additionally, no evidence for a xenolithic origin was observed on the sample boulders, such as remnants of encasing eruptive material (e.g., basalt). The presence of the alteration rims on the whole rock samples (Section 2.5 and 4.1) is consistent with exposure of the blocks to seawater. It thus, seems most likely that the samples were emplaced tectonically.

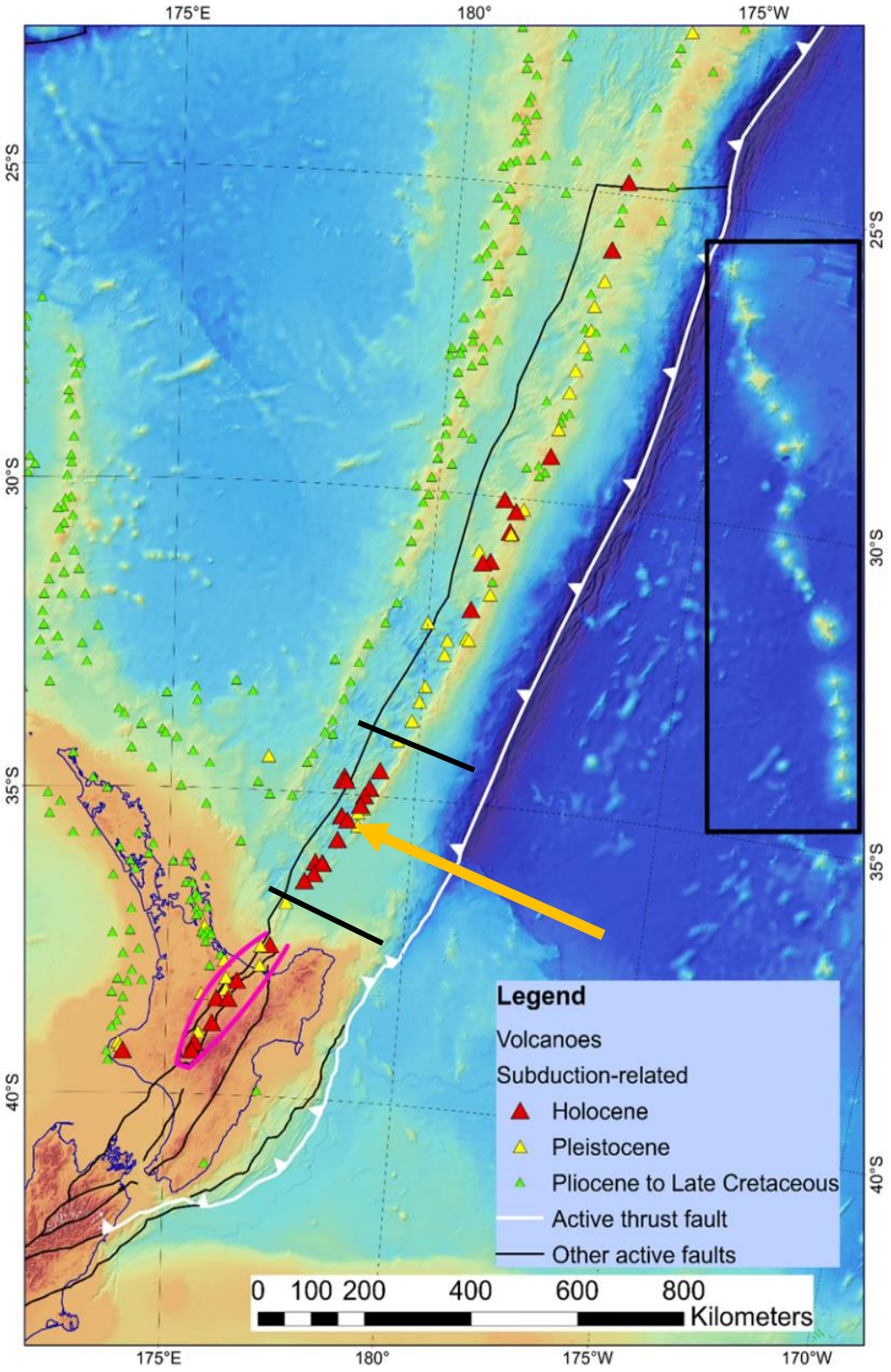

Figure 5-1: Map showing approximate locations of the MANGO 1&2 seismic lines (black lines) from Bassett et al., (2016) and the approximate location of the sample suite dredge location (yellow arrow). Base map and volcano locations modified from Mortimer, N (2020)

Interestingly the estimated depth ranges for the gabbro in this study are broadly similar to estimates of the magma chamber depths of the Rumble II East and West volcanoes, as determined by gravity data modelling (Timm et al., 2016), as well as magma chamber depths estimated from amphiboles phenocryst chemistry from Healy volcano, a silicic caldera (Barker, 2010). However, Rumble II East and West, and Healy are stratovolcanoes rather than the deeper basin from which the gabbro was sampled.

In summary, on the basis of textures, mineral assemblages, temperature, and pressure/depth estimates, the sample suite is considered to have formed as parts of a magma chamber(s) located in the mid to lower crust of the KAHT. Their geomorphic location and alteration suggest they were most likely emplaced on the seafloor tectonically during rifting. However, some questions remain as to the degree of faulting that would be required to expose the samples at the surface.

5.2 Mineral Chemistry and Magma Evolution

Mineral compositions provide insights into magma composition and petrogenesis of the samples. The similarity of the mineral assemblages and textures suggest they represent different parts of a related magmatic system. If so systematic, and coherent chemical variations across the four samples would be expected.

Trace element concentration measured in the clinopyroxene crystals (Section 4.3) reflects the trace element profile of the melt from which they crystallised as well as the crystallographic controls for both the clinopyroxene and various other minerals that grew alongside the clinopyroxene. They can thus be used to provide insights into melt evolution. Figure 5-2 shows selected trace element contents versus clinopyroxene Mg# as a proxy for melt evolution. The elements selected are compatible to moderately incompatible in clinopyroxene (Bougault and Hekinian, 1974, Hart and Dunn, 1993, Vannucci et al., 1998), and therefore have measurable concentrations in the crystals. The trace element contents vary systematically, with samples TAN1213 10-7, 10-8, and 10-10 overlapping (Mg# 70-86) and sample TAN1213 10-1 extending the same trends to lower Mg# (56-70) (Figure 5-2). The mineral major and trace element compositions are therefore consistent with the four samples originating from different parts of the same magmatic system with the more evolved sample, TAN1213 10-1, forming last.

The ternary plots of plagioclase and clinopyroxene (Section 4.2.1 and Section 4.2.2) show that there is an evolution of the minerals across the suite. The plagioclase compositions show an evolution from less evolved (Bytownite, all samples) to more evolved (Labradorite, all samples, and Andesine, TAN1213 10-1 and 10-10) (Section 4.2.1 and Figures 4-16 to 4-19). On an Or vs. An plot (Figure 5-3) the majority of plagioclase from all four samples follow the same trend, which would be consistent with the samples forming from a progressively evolving magma. The clinopyroxene ternary plot shows similar features to the plagioclase, in that, although the clinopyroxene crystals sit within the augite field, there is still variability both between crystals and between samples (Figure 4-20).

The effects of co-crystallising minerals on the trace element profiles of the clinopyroxene are most clearly seen in the Eu/Eu* (Eu anomaly) and Sr/Sr* (Sr anomaly) versus Mg# plots, as well as the chondrite normalised REE plots (Figures 4-21 to 4-30). In the Eu/Eu* and Sr/Sr* versus. Mg# plots it can be seen that as the crystals become more evolved the Eu and Sr anomalies become more negative (Figures 4-25 and 4-30), which indicates that there is co-crystallisation of another mineral phase in which Eu and Sr are more compatible. This can also be seen in the chondrite-normalised plots (Figures 4-21 to 4-29) which show that the more primitive samples show a minor to negligible Eu anomaly when compared to the more evolved samples. The co-crystallisation of plagioclase causes this effect as both elements, Eu and Sr, are more compatible in the plagioclase structure then in the clinopyroxene structure (McKenzie and O'nions, 1991). Over the course of the melt evolution the formation of plagioclase caused the Eu and Sr contents of the melt to become increasingly depleted, which in turn causes the more evolved clinopyroxene crystals to exhibit larger negative Eu and Sr anomalies. In hydrous arc magmas clinopyroxene begins to crystallise before plagioclase due to the suppression of plagioclase crystallisation as a result of the presence of water in the melt (Greene et al., 2006). Therefore, the more primitive (high-Mg#) clinopyroxenes will show a negligible Eu anomaly while more evolved clinopyroxenes will show a more pronounced Eu anomaly (Greene et al., 2006, Plank et al., 2004). This can be seen in the Eu/Eu* versus. Mg# plot (Section 4-3 and Figure 4-30) in which the Eu/Eu* of clinopyroxenes with high Mg# (70-86) are 0.85-1, which is not a substantial Eu anomaly, and indicates that these clinopyroxenes formed prior to significant plagioclase crystallisation.

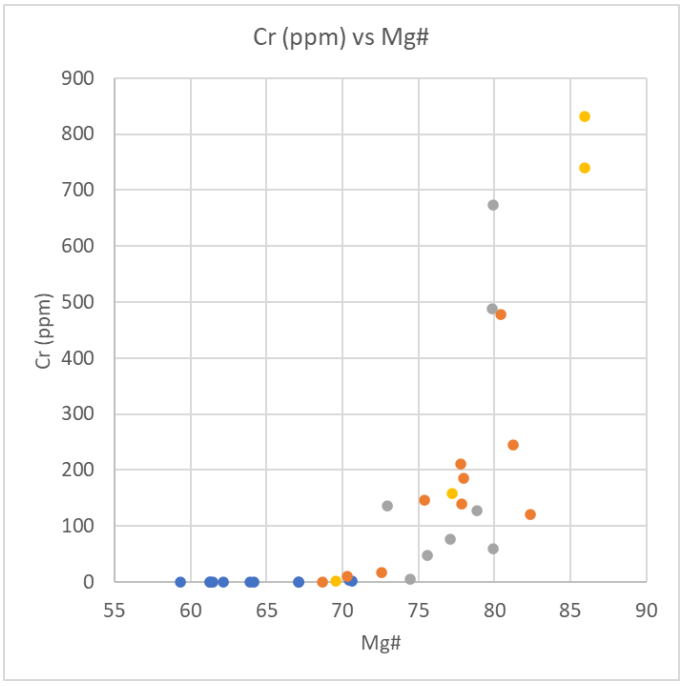
Cr (ppm) vs Mg#
Cr (ppm)
900
800
700
600
500
400
300
200
100
0
55
60
65
70
75
80
85
90
Mg#

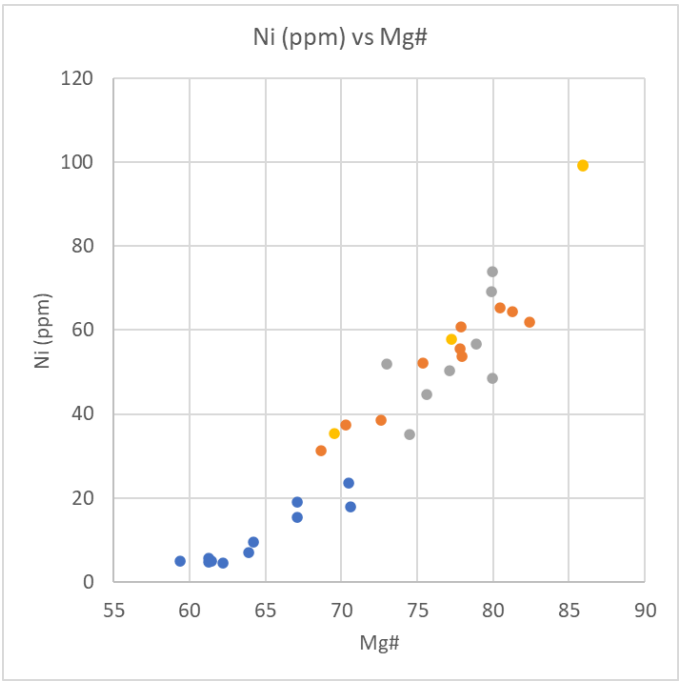
Ni (ppm) vs Mg#
Ni (ppm)
120
100
80
60
40
20
0
55
60
65
70
75
80
85
90
Mg#

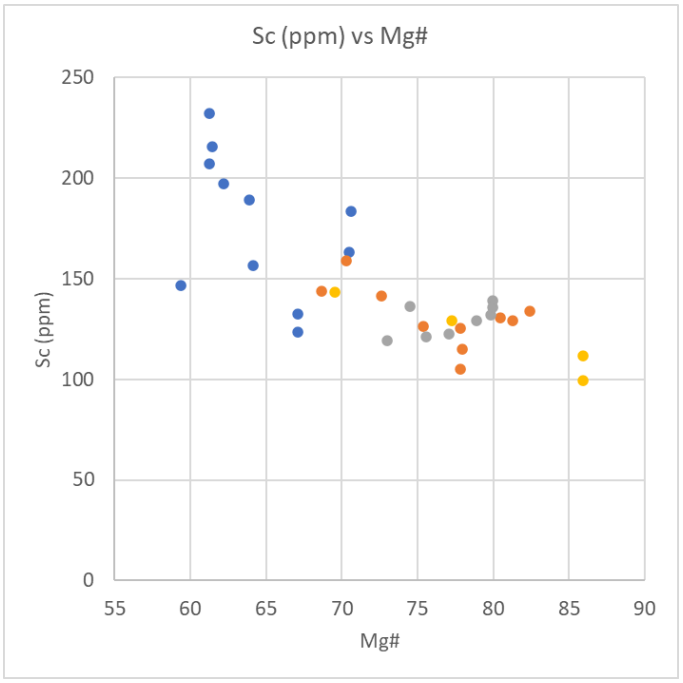
Sc (ppm) vs Mg#
Sc (ppm)
250
200
150
100
50
0
55
60
65
70
75
80
85
90
Mg#

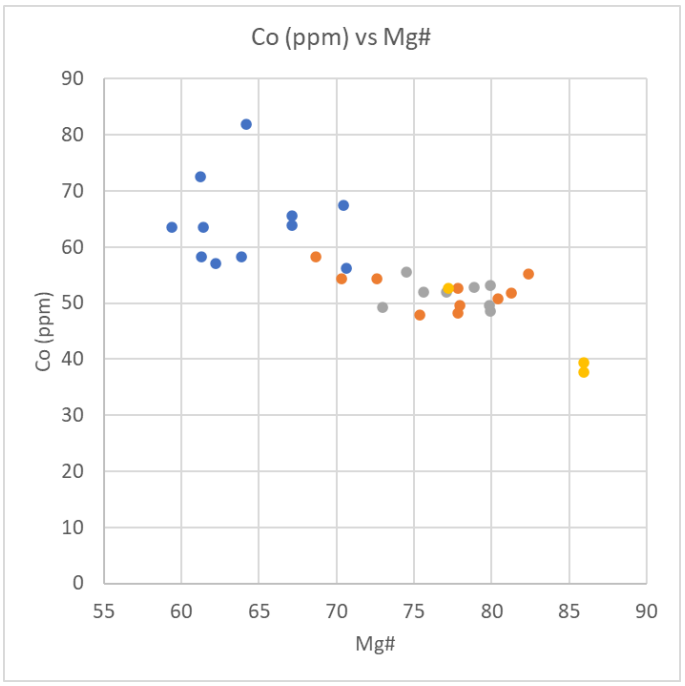
Co (ppm) vs Mg#
Co (ppm)
90
80
70
60
50
40
30
20
10
0
55
60
65
70
75
80
85
90
Mg#

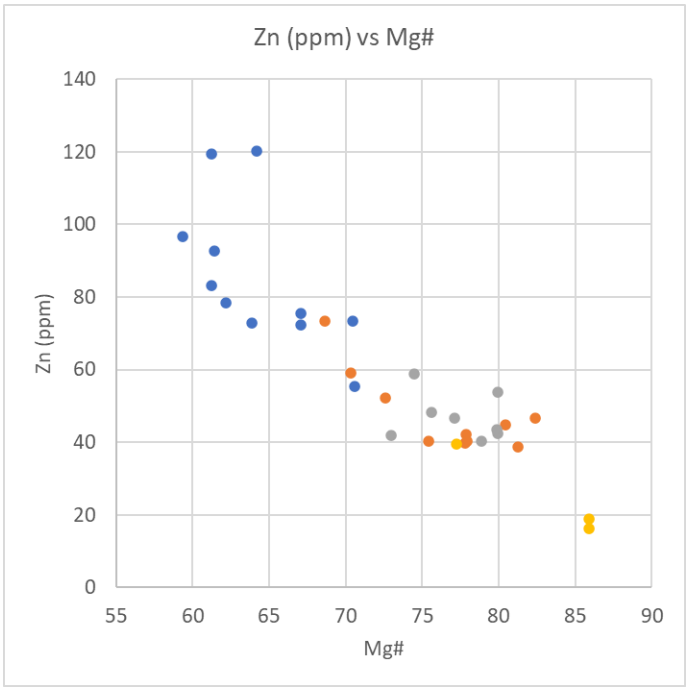

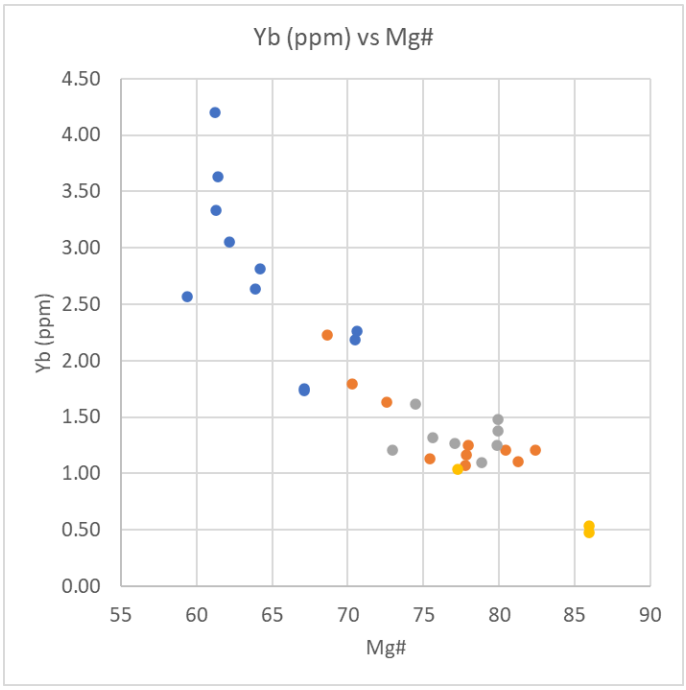

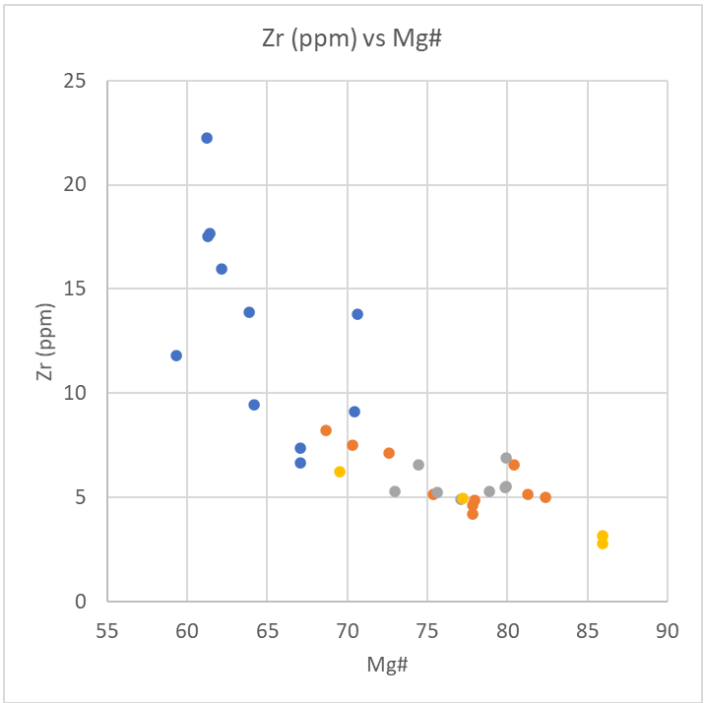

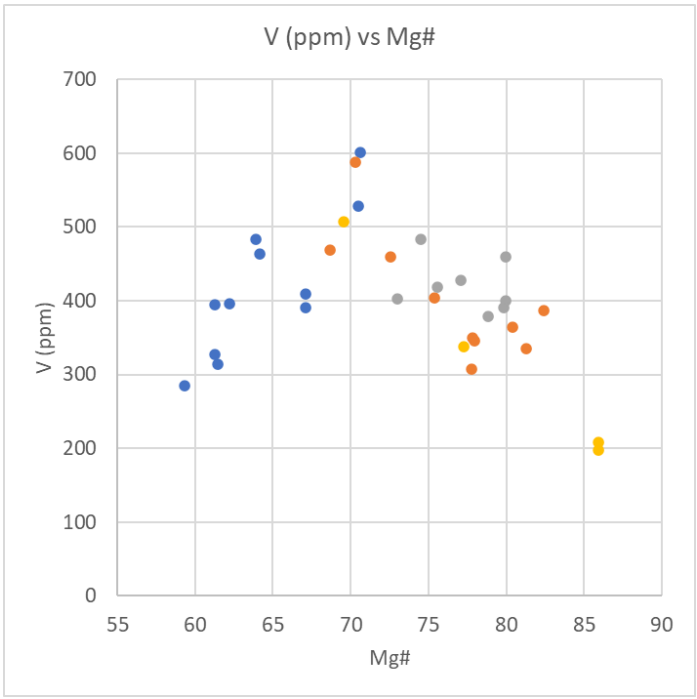

Figure 5-2: Select trace element concentrations vs Mg#.
Elements range from highly compatible in the system (Ni and Cr), slightly incompatible (Sc and Co) to moderately incompatible (Zn, Yb, and Zr). V starts incompatible but then changes to become compatible.
Mg#=(Mg/(Mg+Fe^{2+}))*100
Sample TAN1213 10-1(●)
Sample TAN1213 10-7 (●)
SampleTAN1213 10-8 (●)
Sample TAN1213 10-10 (●)

The variations in trace element behaviour can be broadly explained by the coeval crystallisation of the observed crystal assemblages, large, euhedral minerals: plagioclase, magnetite, and clinopyroxene. Nickel and Cr are compatible in a number of mafic minerals and oxides (Bougault and Hekinian, 1974) and their behaviour in the melt can be used to evaluate when such minerals may have formed in the samples (Figure 5-2). Both Ni and Cr are compatible in olivine (Bougault and Hekinian, 1974), however no evidence of olivine was observed in the samples, neither as a whole crystal, nor as remnant crystals e.g., altered into another mineral due to exposure to seawater. Both Ni and Cr are compatible in magnetite and clinopyroxene, but not plagioclase, and crystallisation of these observed minerals can explain the decreasing patterns in these elements' concentrations with decreasing Mg# (Figure 5-2).

Cobalt and Sc show slight increases in their concentrations with decreasing Mg# (Figure 5-2) which can be explained by both these elements being slightly incompatible in the minerals that are crystallising (magnetite and clinopyroxene). Zinc, Zr, and Yb, are all moderately incompatible in the crystallising minerals (clinopyroxene and magnetite), which can be seen in the consistent and strong increase in their concentrations with decreasing Mg# (Figure 5-1). Zirconium is compatible in zircon, and if zircon had started forming while the clinopyroxene crystals were growing, a decrease in the concentration of Zr with the decreasing Mg# would be expected, which is not seen. Vanadium shows an interesting pattern as it starts off following a trend of incompatibility, with an increase in concentration, in the minerals but at around Mg#=70 the trend changes to that of being compatible, concentration decreases. This could be explained by the increase in the amount of magnetite forming, in which V is compatible in the crystal lattice. This is supported by the observation of a significantly greater amount of magnetite present in sample TAN1213 10-1, which records the compatible V trend (Section 4-1-1).

5.3 Tectonomagmatic Associations

At the start of this study (Section 1-4) three potential tectonomagmatic associations were identified for these samples:

1) Associated with modern KAHT magmatism,
2) Associated with the now rifted Miocene (Colville) Arc crust, or
3) Associated with the pre-arc crust.

Plagioclase compositions for the cumulate suite (Section 4.2.1) are compared to plagioclase phenocrysts from eruptive products representing the modern KAHT (an arc-front volcano, back-arc volcanoes and associated ridges and basins), and from eruptive products representing the Miocene arc (Kermadec and Colville Ridges) (Figure 5-3). The Or content of plagioclase phenocrysts from different components of the modern KAHT and Miocene arcs, follow different trends with melt evolution (vs. An mol% content) (Figure 5-3). Notably, plagioclase analysed from the Colville and Kermadec Ridges show systematically higher Or at a given An content than modern KAHT phenocrysts (Figure 5-3).

The plagioclase analyses from cumulate samples most closely follow the trend of plagioclase phenocrysts from Raphuia Seamount and Rumble II West which are both modern back-arc volcanoes (Figure 5-4). Furthermore, aside from a few individual analyses, they have notably lower Or contents at comparable An content than phenocrysts associated with the Miocene ridges (Figure 5-4).

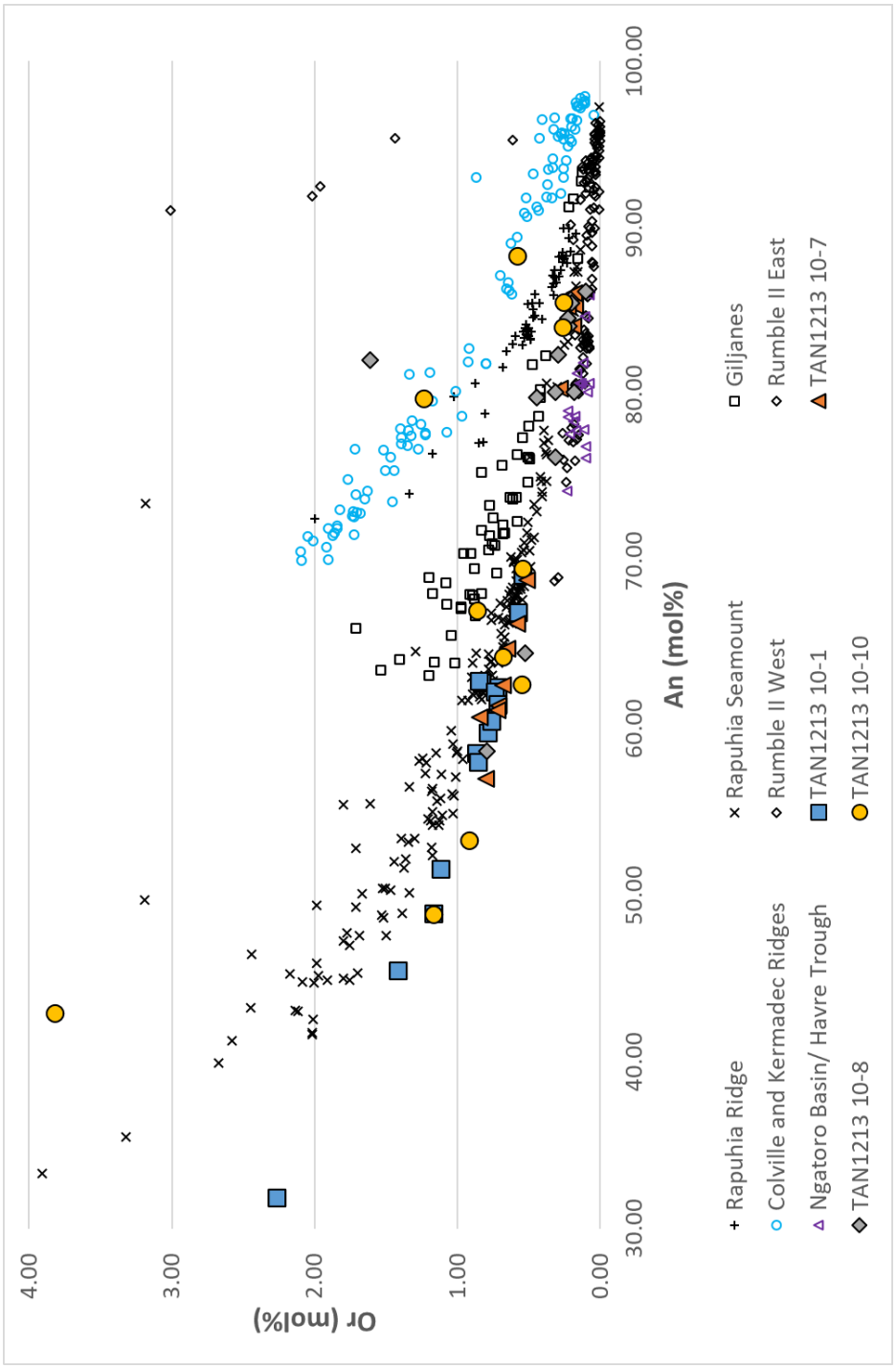

Figure 5-3: Plot sowing plagioclase compositions of samples in this study (filled, coloured shapes) compared to other previous samples from the region. Locations in Figure 5-4

Data from Giljanes, Rapuhia Ridge, and Rapuhia Seamount from (Zohrab, 2016), Colville and Kermadec Ridges (light blue circles) and Ngatoro Basin/Havre Trough (purple triangles) from (Wysoczanski, unpublished data), and Rumble II East and West from (Timm et al., 2016).

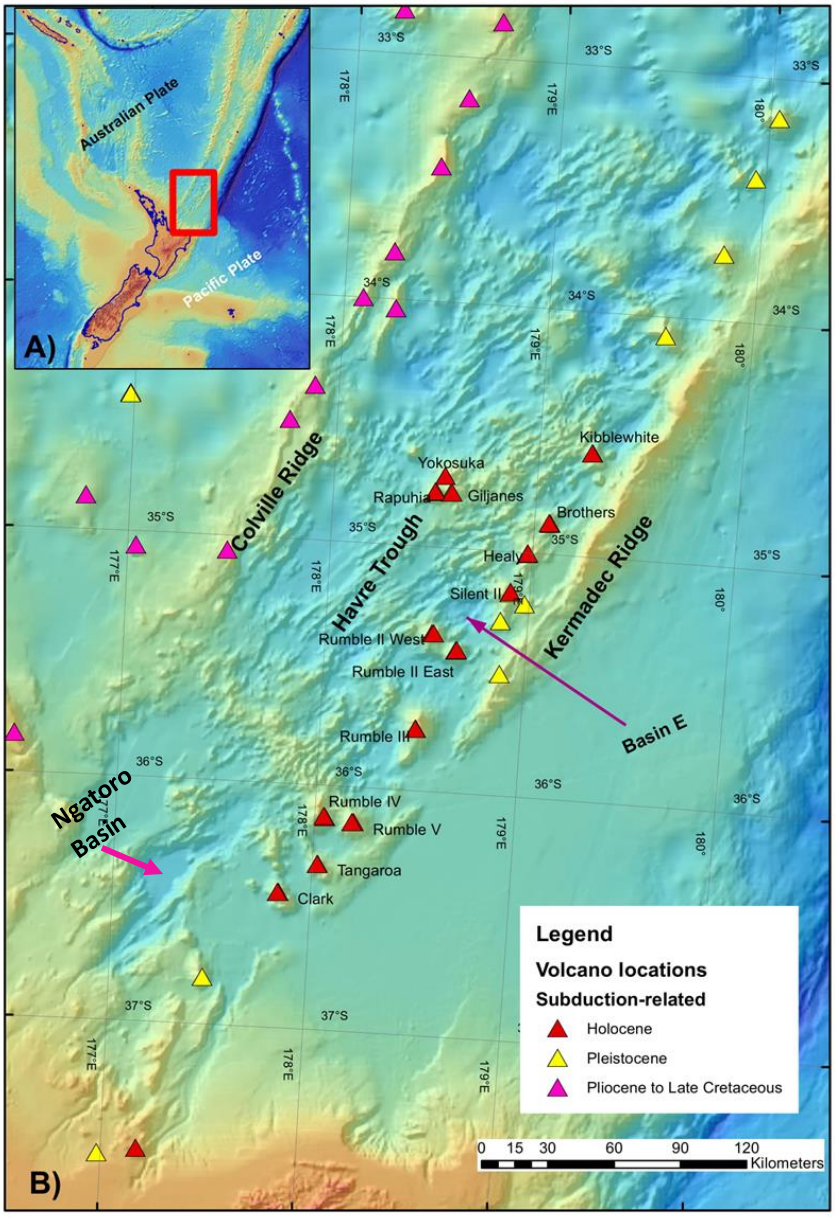

Figure 5-4: Map showing sample and volcano locations from Figure 5-3. Base map and volcano locations modified from Mortimer, N (2020).

Trace element patterns can help to identify tectonomagmatic association (e.g., Pearce and Peate, 1995, Pearce and Stern, 2006, Yamasaki et al., 2006) however, trace elements in clinopyroxenes are compromised by crystallographic controls. A classic subduction zone trace element profile (e.g., Pearce and Peate, 1995) shows relative enrichments in large ion lithophile elements (LILEs) such as Sr and Pb, and depletions in HFSE. However, Sr and Pb are compatible in plagioclase but not in clinopyroxene, and HFSE are also incompatible in clinopyroxene. These elements are therefore all at lower relative concentrations in the clinopyroxene than in associated melt phase, and the clinopyroxene

trace element pattern, therefore, cannot by directly compared with magma (melt) patterns. However, trace element patterns in clinopyroxenes can nonetheless be used as a diagnostic of tectonomagmatic association. Trace elements and especially LILEs in two suites of clinopyroxenes from gabbroic rocks of the Oman ophiolite were used to determine the magmatic setting of the rocks, with one suite formed at a mid-ocean ridge setting and the other suite formed in a supra-subduction zone setting (Yamasaki et al., 2006).

Trace element profiles, and in particular, the ratios of Nd/Yb, Sr/Y, and Nd/Zr in clinopyroxene can be used to differentiate clinopyroxene formed from melts in different tectonomagmatic settings, such as subduction zones or spreading ridges. Therefore, these ratios can help distinguish the tectonomagmatic association the cumulate samples most closely resemble (Table 5-1).

Table 5-1: Table of trace element ratios for clinopyroxenes

	Healy Volcano (KAHT)	Kanaga Island (Aleutians)	Mt Moffett (Aleutians)	Mid-Atlantic Ridge	Cumulate Samples (this study, KAHT)
Nd/Yb	1.63-2.87	1.75-3.41	3.91-10.5	1-1.41	1.24-2.48
Sr/Y	0.14-4.41	0.22-7.56	3.76-47.20	0.76-0.78	0.50-3.92
Nd/Zr	0.31-0.68	0.11-0.43	0.22-2.92	0.2-0.27	0.30-0.52
References	Barker (2010)	Yogodzinski and Kelemen (2007)	Yogodzinski and Kelemen (2007)	Coogan et al., (2000)	Appendix 2.

The trace element ratios show that the cumulate sample clinopyroxene are very similar to the clinopyroxene crystals from a subduction setting (Healy Volcano and Kanaga Island), which suggests that they come from very similar tectonic regimes. Healy Volcano and the cumulate samples are both from the KAHT; therefore, it is not surprising that they have similar trace element ratios but is consistent with the cumulate samples being related to the modern arc eruptive material. The Kanaga Island clinopyroxenes come from ultramafic to mafic cumulate xenoliths found in mafic sills and have been interpretated to

be similar to clinopyroxene phenocrysts found in modern Aleutian basalts (Yogodzinski and Kelemen, 2007). The Mt. Moffett clinopyroxenes from xenoliths hosted in pyroclastic deposits show quite a large variability in their trace elements, which has been attributed to these clinopyroxenes forming from a melt that was more hydrous and had a more strongly fractionated trace element pattern, possibly involved the melting of garnet (Yogodzinski and Kelemen, 2007). The Mid-Atlantic Ridge (MAR) clinopyroxenes are crystals found in primitive gabbro and are taken to represent typical MOR crystals. The MAR clinopyroxene exhibit very limited variability in their trace elements when compared to those from the subduction zones and overall have lower ratios.

Taken in combination, the plagioclase major element compositions and the clinopyroxene trace element data indicate that the cumulate samples most likely represent magmatism associated with the modern KAHT, rather than older rifted crust of the Miocene arc, or a possible oceanic crust (MORB) precursor. This also suggests that the deep back-arc basins of the Havre Trough consist of new material formed from BAB volcanism, with no evidence of pre-existing crust.

Chapter 6 Conclusions

6.1 Key Findings of this Study: A Petrogenetic Model

Ten samples identified as cumulates from on-board descriptions were retrieved from a single dredge along a NE-SW aligned ridge in Basin E, eastern Havre Trough (Wysoczanski et al., 2012b). These represented a rare opportunity to study deep crustal samples from a currently active subduction zone setting.

From this suite, four samples were selected as representative of the range of different grainsizes present. A combination of textural analysis, mineral assemblages, and mineral specific geochemical data have been obtained, and can be used to build a petrogenetic model for the sample suite.

1) All four of the samples exhibit comparable mineral assemblages of plagioclase > clinopyroxene > magnetite, with minor intercumulus quartz, amphibole, sodium rich plagioclase, and K-feldspar. The mesocumulate to orthocumulate textures indicate the samples crystallised at a depth that allowed them to cool relatively slowly and form the relatively large, euhedral cumulus crystals of plagioclase, clinopyroxene, and magnetite. These large, euhedral minerals formed and trapped variable amounts of melt between them, leading to the formation of the more evolved intercumulus material.
2) The three coarser grained samples (1-2 mm) exhibit similar temperature range estimates with the fourth, finer grained sample (<1mm) recording slightly lower temperature range estimates. The fine-grained sample is thus interpreted to have formed from a lower temperature, faster cooling melt to the three coarser grained samples.
3) Plagioclase and clinopyroxene mineral chemistry, major and trace element, form a continuum across all four samples however, consistent with them representing different components of the same magmatic system. The samples are therefore interpreted to represent different components of a related magmatic system: a mid-lower crustal magma chamber.
4) Key trace element ratios (e.g., Nd/Yb) in clinopyroxene are more consistent with the samples forming in a subduction zone environment than related to mid ocean ridge oceanic crust. Plagioclase major element compositions, specifically

An-Or relationships, are comparable to plagioclase phenocrysts from modern back-arc volcanoes, and the suite is therefore related to the modern KAHT back-arc magmatic system.

5) The magma chamber depth is estimated from amphibole crystal chemistry in one sample. The exposure of these mid-lower crustal depth rocks would have been facilitated by normal faulting associated with the rifting and opening of the Havre Trough.

In summary the sample suite is interpreted to represent different components of a mid-lower crustal magma chamber that formed as part of the modern KAHT magmatic system and have been exposed at the seafloor via fault activity associated with continuing extension of the Havre Trough back-arc basin.

6.2 Suggestion for Future Work

The conclusion that these samples are from a magma chamber that is part of the modern KAHT magmatic system can be tested by the following:

1) Whole rock geochemical data of the samples may further constrain the proposed link to the modern KAHT, although care will need to be taken to account for the mobilisation of elements prone to seawater alteration (e.g., alkalis and LILE).
2) Geochronological data for the samples would provide definitive evidence of whether the proposed association with the modern subduction system is correct. This may potentially be achieved through a number of age dating techniques including:
    i) $^{40}Ar/^{39}Ar$ dating, which would require finding plagioclase crystals that have a sufficiently high Or content.
    ii) The finding and dating of zircon if present in the samples. While the Zr vs Mg# plot indicates that zircons were not forming at the same time as the cumulate clinopyroxene, it does show that the melt became enriched in Zr and therefore there is a possibility of zircon forming as a late stage, intercumulus mineral. In addition, during LA-ICP-MS analysis of a clinopyroxene grain the beam went through the crystal and ablated

something with a strong Zr signal, which could indicate the presence of zircon in the samples.

Given the interpretation that the suite represents a sub-arc magma chamber, there is opportunity for further and more detailed study into the magmatic processes which could involve:

1) Expand the study to include all samples from the suite including whole rock geochemical data as well as trialling methods to produce thin sections for more detailed textural and mineral data.
2) Isotopic analysis (Sr, Pb, Nd, Hf), however due to the altered nature of the samples this could require mineral specific work and/or leaching to remove seawater alteration.

References

Ballance, P. F., Ablaev, A. G., Pushchin, I. K., Pletnev, S. P., Birylina, M. G., Itaya, T., Follas, H. A. & Gibson, G. W. 1999. Morphology and history of the Kermadec trench–arc–backarc basin–remnant arc system at 30 to 32 S: geophysical profile, microfossil and K–Ar data. *Marine Geology,* 159**,** 35-62.

Barker, S. 2010. *The petrology and genesis of silicic magmas in the Kermadec arc.* MSc Master's Thesis, Victoria University of Wellington.

Barker, S., Wilson, C., Baker, J., Millet, M.-A., Rotella, M., Wright, I. & Wysoczanski, R. 2013. Geochemistry and petrogenesis of silicic magmas in the intra-oceanic Kermadec arc. *Journal of Petrology,* 54**,** 351-391.

Bassett, D., Kopp, H., Sutherland, R., Henrys, S., Watts, A. B., Timm, C., Scherwath, M., Grevemeyer, I. & de Ronde, C. E. 2016. Crustal structure of the Kermadec arc from MANGO seismic refraction profiles. *Journal of Geophysical Research: Solid Earth,* 121**,** 7514-7546.

Bassett, D., Sutherland, R., Henrys, S., Stern, T., Scherwath, M., Benson, A., Toulmin, S. & Henderson, M. 2010. Three-dimensional velocity structure of the northern Hikurangi margin, Raukumara, New Zealand: Implications for the growth of continental crust by subduction erosion and tectonic underplating. *Geochemistry, Geophysics, Geosystems,* 11.

Bougault, H. & Hekinian, R. 1974. Rift valley in the Atlantic Ocean near 36 50′ N: Petrology and geochemistry of basaltic rocks. *Earth and Planetary Science Letters,* 24**,** 249-261.

Brenan, J., Neroda, E., Lundstrom, C., Shaw, H., Ryerson, F. & Phinney, D. 1998. Behaviour of boron, beryllium, and lithium during melting and crystallization: constraints from mineral-melt partitioning experiments. *Geochimica et Cosmochimica Acta,* 62**,** 2129-2141.

Canil, D. & Lacourse, T. 2020. Geothermometry using minor and trace elements in igneous and hydrothermal magnetite. *Chemical Geology***,** 119576.

Caress, D. W. 1991. Structural trends and back-arc extension in the Havre Trough. *Geophysical research letters,* 18**,** 853-856.

Carter, L., Carter, R., McCave, I. & Gamble, J. 1996. Regional sediment recycling in the abyssal Southwest Pacific Ocean. *Geology,* 24**,** 735-738.

de Ronde, C. E., Baker, E. T., Massoth, G. J., Lupton, J. E., Wright, I. C., Feely, R. A. & Greene, R. R. 2001. Intra-oceanic subduction-related hydrothermal venting, Kermadec volcanic arc, New Zealand. *Earth and Planetary Science Letters,* 193**,** 359-369.

de Ronde, C. E., Hannington, M., Stoffers, P., Wright, I., Ditchburn, R., Reyes, A., Baker, E., Massoth, G., Lupton, J. & Walker, S. 2005. Evolution of a submarine magmatic-hydrothermal system: Brothers volcano, southern Kermadec arc, New Zealand. *Economic Geology,* 100**,** 1097-1133.

DeMets, C., Gordon, R. G., Argus, D. F. & Stein, S. 1994. Effect of recent revisions to the geomagnetic reversal time scale on estimates of current plate motions. *Geophysical research letters,* 21**,** 2191-2194.

Emeleus, C. & Troll, V. R. 2014. The Rum Igneous Centre, Scotland. *Mineralogical Magazine,* 78**,** 805-839.

Flower, M., Russo, R., Tamaki, K. & Hoang, N. 2001. Mantle contamination and the Izu-Bonin-Mariana (IBM)'high-tide mark': evidence for mantle extrusion caused by Tethyan closure. *Tectonophysics,* 333**,** 9-34.

Gamble, J., Smith, I., McCulloch, M., Graham, I. & Kokelaar, B. 1993a. The geochemistry and petrogenesis of basalts from the Taupo Volcanic Zone and Kermadec Island Arc, SW Pacific. *Journal of volcanology and geothermal research,* 54**,** 265-290.

Gamble, J., Woodhead, J., Wright, I. & Smith, I. 1996. Basalt and sediment geochemistry and magma petrogenesis in a transect from oceanic island arc to rifted continental margin arc: the Kermadec—Hikurangi Margin, SW Pacific. *Journal of Petrology,* 37**,** 1523-1546.

Gamble, J. & Wright, I. 1995. The Southern Havre Trough geological structure and magma petrogenesis of an active backarc rift complex. *In:* TAYLOR, B. (ed.) *Backarc Basins.* Springer.
Gamble, J., Wright, I. & Baker, J. 1993b. Seafloor geology and petrology in the oceanic to continental transition zone of the Kermadec-Havre-Taupo Volcanic Zone arc system, New Zealand. *New Zealand Journal of Geology and Geophysics,* 36**,** 417-435.
Gamble, J., Wright, I., Woodhead, J. & McCulloch, M. 1994. Arc and back-arc geochemistry in the southern Kermadec arc-Ngatoro Basin and offshore Taupo Volcanic Zone, SW Pacific. *Geological Society, London, Special Publications,* 81**,** 193-212.
Gamble, J. A., Smith, I. E., Graham, I. J., Kokelaar, B. P., Cole, J. W., Houghton, B. F. & Wilson, C. J. 1990. The petrology, phase relations and tectonic setting of basalts from the Taupo Volcanic Zone, New Zealand and the Kermadec Island Arc-Havre Trough, SW Pacific. *Journal of Volcanology and Geothermal Research,* 43**,** 253-270.
Garfunkel, Z., Anderson, C. & Schubert, G. 1986. Mantle circulation and the lateral migration of subducted slabs. *Journal of Geophysical Research: Solid Earth,* 91**,** 7205-7223.
Ghiorso, M. S. & Evans, B. W. 2008. Thermodynamics of rhombohedral oxide solid solutions and a revision of the Fe-Ti two-oxide geothermometer and oxygen-barometer. *American Journal of Science,* 308**,** 957-1039.
Gill, J., Hoernle, K., Todd, E., Hauff, F., Werner, R., Timm, C., Garbe-Schönberg, D. & Gutjahr, M. 2020. Basalt geochemistry and mantle flow during early backarc basin evolution: Havre Trough and Kermadec Arc, southwest Pacific. *Geochemistry, Geophysics, Geosystems*.
Gill, J. B. 1981. *Orogenic andesites and plate tectonics,* Berlin, Springer-Verlag.
Greene, A. R., DeBari, S. M., Kelemen, P. B., Blusztajn, J. & Clift, P. D. 2006. A detailed geochemical study of island arc crust: the Talkeetna arc section, south–central Alaska. *Journal of Petrology,* 47**,** 1051-1093.
Haase, K. M., Worthington, T. J., Stoffers, P., Garbe-Schönberg, D. & Wright, I. 2002. Mantle dynamics, element recycling, and magma genesis beneath the Kermadec Arc-Havre Trough. *Geochemistry, Geophysics, Geosystems,* 3**,** 1-22.
Haraguchi, S., Ishii, T., Kimura, J.-I. & Ohara, Y. 2003. Formation of tonalite from basaltic magma at the Komahashi-Daini Seamount, northern Kyushu-Palau Ridge in the Philippine Sea, and growth of Izu-Ogasawara (Bonin)-Mariana arc crust. *Contributions to Mineralogy and Petrology,* 145**,** 151-168.
Hart, S. R. & Dunn, T. 1993. Experimental cpx/melt partitioning of 24 trace elements. *Contributions to Mineralogy and Petrology,* 113**,** 1-8.
Hawkesworth, C., Turner, S., McDermott, F., Peate, D. & Van Calsteren, P. 1997. U-Th isotopes in arc magmas: Implications for element transfer from the subducted crust. *Science,* 276**,** 551-555.
Hawthorne, F. C., Oberti, R., Harlow, G. E., Maresch, W. V., Martin, R. F., Schumacher, J. C. & Welch, M. D. 2012. Nomenclature of the amphibole supergroup. *American Mineralogist,* 97**,** 2031-2048.
Heuret, A. & Lallemand, S. 2005. Plate motions, slab dynamics and back-arc deformation. *Physics of the Earth and Planetary Interiors,* 149**,** 31-51.
Ingamells, C. 1980. Analyzed Minerals for Electron Microprobe Standards. *Geostandards Newsletter,* 2**,** 115-115.
Isacks, B. L. & Barazangi, M. 1977. Geometry of Benioff zones: Lateral segmentation and downwards bending of the subducted lithosphere. *In:* TALWANI, M. & PITMAN, W. (eds.) *Island Arcs, Deep Sea Trenches and Back-Arc Basins.*
Jarosewich, E., Nelen, J. & Norberg, J. A. 1980. Reference samples for electron microprobe analysis. *Geostandards Newsletter,* 4**,** 43-47.
Jochum, K. & Enzweiler, J. 2013. Reference materials in geochemical and environmental research. *Treatise on Geochemistry: Second Edition*.
Johnson, M. C. & Plank, T. 2000. Dehydration and melting experiments constrain the fate of subducted sediments. *Geochemistry, Geophysics, Geosystems,* 1.

Karig, D. E. 1972. Remnant arcs. *Geological Society of America Bulletin,* 83**,** 1057-1068.
Kawate, S. & Arima, M. 1998. Petrogenesis of the Tanzawa plutonic complex, central Japan: exposed felsic middle crust of the Izu–Bonin–Mariana arc. *Island Arc,* 7**,** 342-358.
Kearey, P., Klepeis, K. A. & Vine, F. J. 2009. *Global Tectonics*, John Wiley & Sons.
Klaver, M., Matveev, S., Berndt, J., Lissenberg, C. J. & Vroon, P. Z. 2017. A mineral and cumulate perspective to magma differentiation at Nisyros volcano, Aegean arc. *Contributions to Mineralogy and Petrology,* 172**,** 95.
Kumar, A., Marcolli, C. & Peter, T. 2019. Ice nucleation activity of silicates and aluminosilicates in pure water and aqueous solutions–Part 3: Aluminosilicates. *Atmospheric Chemistry and Physics,* 19**,** 6059-6084.
Leat, P. & Larter, R. 2003. Intra-oceanic subduction systems: introduction. *Geological Society, London, Special Publications,* 219**,** 1-17.
Locock, A. J. 2014. An Excel spreadsheet to classify chemical analyses of amphiboles following the IMA 2012 recommendations. *Computers & Geosciences,* 62**,** 1-11.
Malahoff, A., Feden, R. H. & Fleming, H. S. 1982. Magnetic anomalies and tectonic fabric of marginal basins north of New Zealand. *Journal of Geophysical Research: Solid Earth,* 87**,** 4109-4125.
Martinez, F. & Taylor, B. 2006. Modes of crustal accretion in back-arc basins: Inferences from the Lau Basin. *In:* CHRISTIE, D. M., FISHER, C. R., LEE, S.-M. & GIVENS, S. (eds.) *Backarc Spreading Systems: Geological, Biological, Chemical and Physical Interactions.* American Geophysical Union.
McCulloch, M. T. & Gamble, J. 1991. Geochemical and geodynamical constraints on subduction zone magmatism. *Earth and Planetary Science Letters,* 102**,** 358-374.
McDonough, W. F. & Sun, S.-S. 1995. The composition of the Earth. *Chemical Geology,* 120**,** 223-253.
McKenzie, D. & O'nions, R. 1991. Partial melt distributions from inversion of rare earth element concentrations. *Journal of Petrology,* 32**,** 1021-1091.
Morimoto, N. 1988. Nomenclature of pyroxenes. *Mineralogy and Petrology,* 39**,** 55-76.
Mortimer, N., Gans, P., Palin, J., Meffre, S., Herzer, R. & Skinner, D. 2010. Location and migration of Miocene–Quaternary volcanic arcs in the SW Pacific region. *Journal of Volcanology and Geothermal Research,* 190**,** 1-10.
Mortimer N, S. L. B., Black J. 2020. *Te Riu-a-Māui / Zealandia digital geoscience data compilation, GNS Science geological map 11*, 1:8 500 000. Lower Hutt, New Zealand: GNS Science.
Nakakuki, T. & Mura, E. 2013. Dynamics of slab rollback and induced back-arc basin formation. *Earth and Planetary Science Letters,* 361**,** 287-297.
Parson, L. & Wright, I. 1996. The Lau-Havre-Taupo back-arc basin: A southward-propagating, multi-stage evolution from rifting to spreading. *Tectonophysics,* 263**,** 1-22.
Pearce, J. A. & Peate, D. W. 1995. Tectonic implications of the composition of volcanic arc magmas. *Annual review of Earth and Planetary Sciences,* 23**,** 251-286.
Pearce, J. A. & Stern, R. J. 2006. Origin of back-arc basin magmas: trace element and isotope perspectives. *Geophysical Monograph-American Geophysical Union,* 166**,** 63.
Plank, T., Benjamin, E., Wade, J. & Grove, T. A new hygrometer based on the europium anomaly in clinopyroxene phenocrysts in arc volcanic rocks. AGU Fall Meeting Abstracts, 2004. V12A-05.
Pullan, V. 2018. *Geomorphology and Geochemistry of Back Arc Basins in the Havre Trough, Southwest Pacific.* MSc MSc Thesis, Victoria University of Wellington.
Reagan, M. K., Heaton, D. E., Schmitz, M. D., Pearce, J. A., Shervais, J. W. & Koppers, A. A. 2019. Forearc ages reveal extensive short-lived and rapid seafloor spreading following subduction initiation. *Earth and Planetary Science Letters,* 506**,** 520-529.
Ridolfi, F., Renzulli, A. & Puerini, M. 2010. Stability and chemical equilibrium of amphibole in calc-alkaline magmas: an overview, new thermobarometric formulations and application to subduction-related volcanoes. *Contributions to Mineralogy and Petrology,* 160**,** 45-66.

Ruellan, E., Delteil, J., Wright, I. & Matsumoto, T. 2003. From rifting to active spreading in the Lau Basin–Havre Trough backarc system (SW Pacific): Locking/unlocking induced by seamount chain subduction. *Geochemistry, Geophysics, Geosystems,* 4.

Sdrolias, M. & Müller, R. D. 2006. Controls on back-arc basin formation. *Geochemistry, Geophysics, Geosystems,* 7.

Smith, I. E. & Price, R. C. 2006. The Tonga–Kermadec arc and Havre–Lau back-arc system: their role in the development of tectonic and magmatic models for the western Pacific. *Journal of Volcanology and Geothermal Research,* 156**,** 315-331.

Smith, I. E., Stewart, R. B., Price, R. C. & Worthington, T. J. 2010. Are arc-type rocks the products of magma crystallisation? Observations from a simple oceanic arc volcano: Raoul Island, Kermadec Arc, SW Pacific. *Journal of Volcanology and Geothermal Research,* 190**,** 219-234.

Streckeisen, A. 1976. To each plutonic rock its proper name. *Earth Science Reviews,* 12**,** 1-33.

Sun, S.-S. & McDonough, W. F. 1989. Chemical and isotopic systematics of oceanic basalts: implications for mantle composition and processes. *Geological Society, London, Special Publications,* 42**,** 313-345.

Tatsumi, Y., Maruyama, S. & Nohda, S. 1990. Mechanism of backarc opening in the Japan Sea: role of asthenospheric injection. *Tectonophysics,* 181**,** 299-306.

Timm, C., Bassett, D., Graham, I. J., Leybourne, M. I., de Ronde, C. E., Woodhead, J., Layton-Matthews, D. & Watts, A. B. 2013. Louisville seamount subduction and its implication on mantle flow beneath the central Tonga–Kermadec arc. *Nature Communications,* 4**,** 1-9.

Timm, C., Davy, B., Haase, K., Hoernle, K. A., Graham, I. J., de Ronde, C. E., Woodhead, J., Bassett, D., Hauff, F. & Mortimer, N. 2014. Subduction of the oceanic Hikurangi Plateau and its impact on the Kermadec arc. *Nature Communications,* 5**,** 1-9.

Timm, C., de Ronde, C., Hoernle, K., Cousens, B., Wartho, J.-A., Tontini, F. C., Wysoczanski, R., Hauff, F. & Handler, M. 2019. New age and geochemical data from the southern Colville and Kermadec ridges, SW Pacific: insights into the recent geological history and petrogenesis of the Proto-Kermadec (Vitiaz) Arc. *Gondwana Research,* 72**,** 169-193.

Timm, C., Leybourne, M. I., Hoernle, K., Wysoczanski, R. J., Hauff, F., Handler, M., Caratori Tontini, F. & de Ronde, C. E. 2016. Trench-perpendicular geochemical variation between two adjacent Kermadec Arc volcanoes Rumble II East and West: the role of the subducted Hikurangi Plateau in element recycling in arc magmas. *Journal of Petrology,* 57**,** 1335-1360.

Todd, E., Gill, J., Wysoczanski, R., Handler, M. R., Wright, I. & Gamble, J. 2010. Sources of constructional cross-chain volcanism in the southern Havre Trough: New insights from HFSE and REE concentration and isotope systematics. *Geochemistry, Geophysics, Geosystems,* 11.

Todd, E., Gill, J., Wysoczanski, R. J., Hergt, J., Wright, I. C., Leybourne, M. I. & Mortimer, N. 2011. Hf isotopic evidence for small-scale heterogeneity in the mode of mantle wedge enrichment: Southern Havre Trough and South Fiji Basin back arcs. *Geochemistry, Geophysics, Geosystems,* 12.

Tontini, F. C., Bassett, D., de Ronde, C. E., Timm, C. & Wysoczanski, R. 2019. Early evolution of a young back-arc basin in the Havre Trough. *Nature Geoscience,* 12**,** 856-862.

Turnbull, R., Weaver, S., Tulloch, A., Cole, J., Handler, M. & Ireland, T. 2010. Field and geochemical constraints on mafic–felsic interactions, and processes in high-level arc magma chambers: an example from the Halfmoon Pluton, New Zealand. *Journal of Petrology,* 51**,** 1477-1505.

Turner, S., Hawkesworth, C., Rogers, N., Bartlett, J., Worthington, T., Hergt, J., Pearce, J. & Smith, I. 1997. 238U-230Th disequilibria, magma petrogenesis, and flux rates beneath the depleted Tonga-Kermadec island arc. *Geochimica et Cosmochimica Acta,* 61**,** 4855-4884.

Uyeda, S. & Kanamori, H. 1979. Back-arc opening and the mode of subduction. *Journal of Geophysical Research: Solid Earth,* 84**,** 1049-1061.

Vannucci, R., Bottazzi, P., Wulff-Pedersen, E. & Neumann, E.-R. 1998. Partitioning of REE, Y, Sr, Zr and Ti between clinopyroxene and silicate melts in the mantle under La Palma (Canary Islands):

implications for the nature of the metasomatic agents. *Earth and Planetary Science Letters,* 158**,** 39-51.
Wager, L., Brown, G. & Wadsworth, W. 1960. Types of igneous cumulates. *Journal of Petrology,* 1**,** 73-85.
Whitney, D. L. & Evans, B. W. 2010. Abbreviations for names of rock-forming minerals. *American Mineralogist,* 95**,** 185-187.
Wilson, C., Houghton, B., McWilliams, M., Lanphere, M., Weaver, S. & Briggs, R. 1995. Volcanic and structural evolution of Taupo Volcanic Zone, New Zealand: a review. *Journal of Volcanology and Geothermal Research,* 68**,** 1-28.
Wilson, M. 1989. *Igneous petrogenesis,* London, Unwin Hyman.
Wright, I. 1993. Pre-spread rifting and heterogeneous volcanism in the southern Havre Trough back-arc basin. *Marine geology,* 113**,** 179-200.
Wright, I., Parson, L. & Gamble, J. 1996. Evolution and interaction of migrating cross-arc volcanism and backarc rifting: An example from the southern Havre Trough (35 20'–37 S). *Journal of Geophysical Research: Solid Earth,* 101**,** 22071-22086.
Wright, I., Worthington, T. & Gamble, J. 2006. New multibeam mapping and geochemistry of the 30–35 S sector, and overview, of southern Kermadec arc volcanism. *Journal of Volcanology and Geothermal Research,* 149**,** 263-296.
Wright, I. C. 1997. Morphology and evolution of the remnant Colville and active Kermadec arc ridges south of 33 30' S. *Marine Geophysical Researches,* 19**,** 177-193.
Wysoczanski, R., Handler, M., Schipper, C., Leybourne, M., Creech, J., Rotella, M., Nichols, A., Wilson, C. & Stewart, R. 2012a. The tectonomagmatic source of ore metals and volatile elements in the southern Kermadec arc. *Economic Geology,* 107**,** 1539-1556.
Wysoczanski, R., Leonard, G., Gill, J., Wright, I., Calvert, A., McIntosh, W., Jicha, B., Gamble, J., Timm, C., Handler, M., Drewes-Todd, E. & Zohrab, A. 2019. Ar-Ar age constraints on the timing of Havre Trough opening and magmatism. *New Zealand Journal of Geology and Geophysics***,** 1-7.
Wysoczanski, R., Mountjoy, J., Barton, S., Black, J., Boschen, R., Kaiser, S., Khong, L., Mitchell, J., Pallentin, A. & Stewart, R. 2012b. NIRVANA–TAN1213 RV Tangaroa Research Voyage Report. NIWA Internal Report. New Zealand: NIWA Wellington.
Wysoczanski, R., Todd, E., Wright, I., Leybourne, M., Hergt, J., Adam, C. & Mackay, K. 2010. Backarc rifting, constructional volcanism and nascent disorganised spreading in the southern Havre Trough backarc rifts (SW Pacific). *Journal of Volcanology and Geothermal Research,* 190**,** 39-57.
Wysoczanski, R., Wright, I., Gamble, J. A., Hauri, E., Luhr, J., Eggins, S. & Handler, M. 2006. Volatile contents of Kermadec Arc–Havre Trough pillow glasses: Fingerprinting slab-derived aqueous fluids in the mantle sources of arc and back-arc lavas. *Journal of Volcanology and Geothermal Research,* 152**,** 51-73.
Yamasaki, T., Maeda, J. & Mizuta, T. 2006. Geochemical evidence in clinopyroxenes from gabbroic sequence for two distinct magmatisms in the Oman ophiolite. *Earth and Planetary Science Letters,* 251**,** 52-65.
Yavuz, F. & Döner, Z. 2017. WinAmptb: A Windows program for calcific amphibole thermobarometry. *Periodico di Mineralogia,* 86**,** 135-167.
Yogodzinski, G. & Kelemen, P. 2007. Trace elements in clinopyroxenes from Aleutian xenoliths: Implications for primitive subduction magmatism in an island arc. *Earth and Planetary Science Letters,* 256**,** 617-632.
Zohrab, A. 2016. *The petrology, geochemistry and geochronology of back-arc stratovolcanoes in the southern Kermadec Arc-Havre Trough, SW Pacific.* MSc Master's Thesis, Victoria University of Wellington.

Appendices

Appendix 1: Mineral Major Element Data

Appendix 2: Clinopyroxene Trace Element Data

Appendix 3: Analytical Standards and Uncertainties

Appendix 1 Mineral Major Element Data

Table A-1: Table of plagioclase major element compositions

TAN1213 10-1															
Oxides (wt%)	**Plagioclase-01**	**Plagioclase-02**	**Plagioclase-03**	**Plagioclase-04**	**Plagioclase-05**	**Plagioclase-06**	**Plagioclase-07**	**Plagioclase-08**	**Plagioclase-09**	**Plagioclase-10**	**Plagioclase-11**	**Plagioclase-12**	**Plagioclase-13**	**Plagioclase-14**	**Plagioclase-15**
SiO2	50.80	52.90	55.50	51.40	51.60	57.20	60.60	52.10	56.30	53.60	53.60	52.70	53.20	52.60	53.70
TiO2	0.01	0.03	0.01	0.04	0.03	0.00	0.02	0.03	0.02	0.02	0.03	0.03	0.02	0.04	0.02
Al2O3	30.50	29.20	27.60	27.50	30.10	26.60	24.20	28.50	27.20	28.80	28.90	29.10	29.00	29.40	28.70
FeO	0.98	0.81	0.89	2.64	1.11	0.68	0.64	2.07	0.69	0.84	0.87	1.16	0.86	1.05	0.75
MnO	0.00	0.01	0.01	0.00	0.00	0.02	0.00	0.01	0.00	0.00	0.02	0.01	0.00	0.03	0.00
MgO	0.12	0.08	0.05	1.05	0.10	0.01	0.00	0.72	0.03	0.06	0.10	0.22	0.10	0.08	0.08
CaO	14.00	12.60	10.40	11.70	13.50	9.15	6.32	12.10	9.70	11.70	12.10	12.50	12.20	12.40	11.70
Na2O	3.39	4.11	5.26	3.76	3.61	5.92	7.23	3.88	5.48	4.49	4.42	4.11	4.35	4.23	4.60
K2O	0.09	0.12	0.19	0.13	0.10	0.24	0.38	0.14	0.20	0.15	0.13	0.12	0.13	0.12	0.15
Cr2O3	0.00	0.00	0.00	0.00	0.00	0.01	0.00	0.00	0.00	0.00	0.00	0.01	0.00	0.00	0.02
Total	99.80	99.90	99.80	98.10	100.00	99.90	99.40	99.50	99.60	99.60	100.00	99.90	99.80	100.00	99.70
Cations															
Si	2.32	2.41	2.51	2.39	2.35	2.58	2.73	2.39	2.55	2.44	2.43	2.40	2.42	2.39	2.44
Ti	0.00	0.00	0.00	0.00	0.00	0.00	0.00	0.00	0.00	0.00	0.00	0.00	0.00	0.00	0.00
Al	1.64	1.57	1.48	1.51	1.62	1.41	1.29	1.54	1.45	1.55	1.54	1.56	1.55	1.58	1.54
Fe (Total)	0.04	0.03	0.03	0.10	0.04	0.03	0.02	0.08	0.03	0.03	0.03	0.04	0.03	0.04	0.03
Mn	0.00	0.00	0.00	0.00	0.00	0.00	0.00	0.00	0.00	0.00	0.00	0.00	0.00	0.00	0.00
Mg	0.01	0.01	0.00	0.07	0.01	0.00	0.00	0.05	0.00	0.00	0.01	0.02	0.01	0.01	0.01
Ca	0.69	0.62	0.50	0.58	0.66	0.44	0.31	0.60	0.47	0.57	0.59	0.61	0.60	0.61	0.57
Na	0.30	0.36	0.46	0.34	0.32	0.52	0.63	0.35	0.48	0.40	0.39	0.36	0.38	0.37	0.41
K	0.01	0.01	0.01	0.01	0.01	0.01	0.02	0.01	0.01	0.01	0.01	0.01	0.01	0.01	0.01
Total	5.00	5.00	5.00	5.00	5.00	5.00	5.00	5.00	5.00	5.00	5.00	5.00	5.00	5.00	5.00
An	69.10	62.40	51.50	62.70	66.90	45.40	31.80	62.80	48.90	58.50	59.70	62.20	60.40	61.40	57.90
Ab	30.30	36.80	47.40	36.50	32.50	53.20	65.90	36.40	49.90	40.60	39.50	37.10	38.90	37.90	41.20
Or	0.55	0.72	1.12	0.83	0.57	1.42	2.27	0.85	1.17	0.87	0.79	0.74	0.76	0.72	0.85

TAN1213 10-7													
Oxides (wt%)	**Plagioclase-01**	**Plagioclase-02**	**Plagioclase-03**	**Plagioclase-04**	**Plagioclase-05**	**Plagioclase-06**	**Plagioclase-07**	**Plagioclase-08**	**Plagioclase-09**	**Plagioclase-10**	**Plagioclase-11**	**Plagioclase-12**	**Plagioclase-13**
SiO2	46.70	47.10	52.80	48.20	52.70	51.60	50.90	51.80	52.60	46.60	54.00	46.80	52.40
TiO2	0.01	0.00	0.04	0.01	0.03	0.01	0.01	0.02	0.03	0.00	0.04	0.01	0.02
Al2O3	33.70	33.50	29.50	33.00	29.60	30.10	30.60	30.00	29.30	33.80	28.90	33.60	28.80
FeO	0.91	0.96	0.80	1.06	0.81	0.90	0.89	0.86	1.03	0.99	0.76	0.90	0.73
MnO	0.01	0.00	0.00	0.00	0.00	0.00	0.02	0.01	0.01	0.00	0.00	0.02	0.01
MgO	0.10	0.08	0.10	0.11	0.09	0.09	0.11	0.08	0.20	0.09	0.08	0.10	0.08
CaO	17.50	17.10	12.30	16.50	12.70	13.40	13.90	13.10	12.30	17.40	11.60	17.40	12.10
Na2O	1.64	1.77	4.32	2.19	4.11	3.70	3.41	3.86	4.19	1.54	4.75	1.63	4.18
K2O	0.03	0.03	0.14	0.05	0.12	0.10	0.09	0.11	0.12	0.03	0.14	0.04	0.12
Cr2O3	0.00	0.01	0.02	0.01	0.00	0.01	0.00	0.01	0.00	0.00	0.00	0.00	0.02
Total	101.00	101.00	100.00	101.00	100.00	99.90	99.90	99.80	99.70	100.00	100.00	100.00	98.40
Cations													
Si	2.13	2.15	2.40	2.19	2.39	2.35	2.32	2.36	2.40	2.13	2.44	2.14	2.42
Ti	0.00	0.00	0.00	0.00	0.00	0.00	0.00	0.00	0.00	0.00	0.00	0.00	0.00
Al	1.82	1.80	1.58	1.77	1.58	1.62	1.65	1.61	1.57	1.83	1.54	1.82	1.57
Fe (Total)	0.03	0.04	0.03	0.04	0.03	0.03	0.03	0.03	0.04	0.04	0.03	0.03	0.03
Mn	0.00	0.00	0.00	0.00	0.00	0.00	0.00	0.00	0.00	0.00	0.00	0.00	0.00
Mg	0.01	0.01	0.01	0.01	0.01	0.01	0.01	0.01	0.01	0.01	0.01	0.01	0.01
Ca	0.86	0.84	0.60	0.80	0.62	0.65	0.68	0.64	0.60	0.86	0.56	0.85	0.60
Na	0.15	0.16	0.38	0.19	0.36	0.33	0.30	0.34	0.37	0.14	0.42	0.15	0.37
K	0.00	0.00	0.01	0.00	0.01	0.01	0.01	0.01	0.01	0.00	0.01	0.00	0.01
Total	5.00	5.00	5.00	5.00	5.00	5.00	5.00	5.00	5.00	5.00	5.00	5.00	5.00
An	85.30	84.10	60.70	80.40	62.60	66.30	68.90	64.80	61.40	86.10	57.00	85.30	61.10
Ab	14.50	15.70	38.50	19.30	36.70	33.20	30.60	34.60	37.90	13.70	42.20	14.50	38.20
Or	0.18	0.19	0.84	0.29	0.68	0.58	0.51	0.65	0.71	0.18	0.80	0.23	0.72

TAN1213 10-8													
Oxides (wt%)	**Plagioclase-01**	**Plagioclase-02**	**Plagioclase-03**	**Plagioclase-04**	**Plagioclase-05**	**Plagioclase-06**	**Plagioclase-07**	**Plagioclase-08**	**Plagioclase-09**	**Plagioclase-10**	**Plagioclase-11**	**Plagioclase-12**	**Plagioclase-13**
SiO2	46.60	47.20	47.20	47.00	49.10	47.10	52.50	48.00	54.00	46.80	46.30	48.00	48.50
TiO2	0.02	0.00	0.13	0.00	0.02	0.00	0.03	0.00	0.04	0.02	0.00	0.01	0.02
Al2O3	33.90	33.40	30.10	33.80	31.90	33.70	30.10	32.90	29.00	33.90	31.30	32.30	32.70
FeO	0.78	0.91	3.82	0.94	0.90	0.93	0.95	1.11	0.85	0.84	2.08	1.39	0.90
MnO	0.00	0.00	0.04	0.01	0.00	0.00	0.01	0.00	0.00	0.01	0.02	0.01	0.00
MgO	0.12	0.12	1.29	0.12	0.12	0.10	0.10	0.11	0.07	0.13	0.60	0.21	0.14
CaO	17.50	17.00	15.30	17.40	15.50	17.30	13.00	16.40	11.80	17.50	15.80	15.90	16.20
Na2O	1.54	1.75	1.68	1.58	2.63	1.72	3.89	2.22	4.52	1.62	1.83	2.17	2.18
K2O	0.02	0.04	0.25	0.04	0.05	0.04	0.09	0.03	0.14	0.04	0.05	0.08	0.05
Cr2O3	0.00	0.02	0.02	0.01	0.01	0.00	0.00	0.00	0.00	0.00	0.01	0.00	0.00
Total	100.00	100.00	99.80	101.00	100.00	101.00	101.00	101.00	100.00	101.00	97.90	100.00	101.00
Cations													
Si	2.14	2.16	2.19	2.14	2.24	2.15	2.37	2.19	2.44	2.14	2.18	2.20	2.21
Ti	0.00	0.00	0.00	0.00	0.00	0.00	0.00	0.00	0.00	0.00	0.00	0.00	0.00
Al	1.83	1.80	1.64	1.82	1.72	1.81	1.61	1.77	1.54	1.82	1.73	1.75	1.76
Fe (Total)	0.03	0.03	0.15	0.04	0.03	0.04	0.04	0.04	0.03	0.03	0.08	0.05	0.03
Mn	0.00	0.00	0.00	0.00	0.00	0.00	0.00	0.00	0.00	0.00	0.00	0.00	0.00
Mg	0.01	0.01	0.09	0.01	0.01	0.01	0.01	0.01	0.00	0.01	0.04	0.01	0.01
Ca	0.86	0.83	0.76	0.85	0.76	0.84	0.63	0.80	0.57	0.85	0.79	0.78	0.79
Na	0.14	0.16	0.15	0.14	0.23	0.15	0.34	0.20	0.40	0.14	0.17	0.19	0.19
K	0.00	0.00	0.02	0.00	0.00	0.00	0.01	0.00	0.01	0.00	0.00	0.00	0.00
Total	5.00	5.00	5.00	5.00	5.00	5.00	5.00	5.00	5.00	5.00	5.00	5.00	5.00
An	86.20	84.10	82.10	85.70	76.30	84.60	64.50	80.20	58.70	85.50	82.40	79.80	80.10
Ab	13.70	15.70	16.30	14.10	23.40	15.20	35.00	19.70	40.50	14.30	17.30	19.70	19.60
Or	0.10	0.22	1.61	0.21	0.32	0.23	0.53	0.19	0.80	0.20	0.30	0.45	0.31

TAN1213 10-10												
Oxides (wt%)	**Plagioclase-01**	**Plagioclase-02**	**Plagioclase-03**	**Plagioclase-04**	**Plagioclase-05**	**Plagioclase-06**	**Plagioclase-07**	**Plagioclase-08**	**Plagioclase-09**	**Plagioclase-10**	**Plagioclase-11**	**Plagioclase-12**
SiO2	57.30	52.50	46.90	47.10	58.10	52.50	55.40	51.30	50.80	56.40	43.90	45.10
TiO2	0.02	0.02	0.00	0.01	0.03	0.03	0.02	0.02	0.03	0.01	0.01	0.00
Al2O3	22.80	29.90	33.90	33.80	25.70	30.00	28.40	31.20	29.50	27.60	29.30	33.50
FeO	3.46	0.89	0.90	0.96	1.14	0.82	0.73	1.22	2.08	0.62	0.90	0.80
MnO	0.03	0.02	0.03	0.00	0.01	0.01	0.00	0.02	0.00	0.00	0.04	0.02
MgO	1.75	0.09	0.08	0.08	0.26	0.07	0.06	0.09	0.70	0.04	0.09	0.09
CaO	6.07	13.00	17.60	17.20	8.55	12.70	10.90	14.10	13.00	9.85	14.60	17.50
Na2O	6.40	3.93	1.62	1.78	5.88	4.15	5.18	3.36	3.43	5.58	1.93	1.22
K2O	0.79	0.12	0.05	0.05	0.64	0.09	0.16	0.09	0.14	0.20	0.19	0.10
Cr2O3	0.00	0.00	0.01	0.03	0.01	0.02	0.00	0.00	0.00	0.00	0.00	0.00
Total	98.60	100.00	101.00	101.00	100.00	100.00	101.00	101.00	99.60	100.00	91.00	98.30
Cations												
Si	2.61	2.38	2.14	2.14	2.62	2.37	2.48	2.31	2.33	2.54	2.21	2.11
Ti	0.00	0.00	0.00	0.00	0.00	0.00	0.00	0.00	0.00	0.00	0.00	0.00
Al	1.23	1.60	1.82	1.81	1.36	1.60	1.50	1.66	1.59	1.46	1.75	1.85
Fe (Total)	0.13	0.03	0.03	0.04	0.04	0.03	0.03	0.05	0.08	0.02	0.04	0.03
Mn	0.00	0.00	0.00	0.00	0.00	0.00	0.00	0.00	0.00	0.00	0.00	0.00
Mg	0.12	0.01	0.01	0.01	0.02	0.00	0.00	0.01	0.05	0.00	0.01	0.01
Ca	0.30	0.63	0.86	0.84	0.41	0.62	0.52	0.68	0.64	0.48	0.79	0.88
Na	0.57	0.35	0.14	0.16	0.51	0.36	0.45	0.29	0.31	0.49	0.19	0.11
K	0.05	0.01	0.00	0.00	0.04	0.01	0.01	0.01	0.01	0.01	0.01	0.01
Total	5.00	5.00	5.00	5.00	5.00	5.00	5.00	5.00	5.00	5.00	5.00	5.00
An	32.60	64.20	85.50	84.00	42.90	62.60	53.30	69.50	67.00	48.80	79.70	88.30
Ab	62.30	35.10	14.30	15.70	53.30	36.90	45.80	29.90	32.10	50.00	19.00	11.10
Or	5.08	0.68	0.26	0.26	3.82	0.55	0.92	0.55	0.86	1.17	1.24	0.58

Table A-2: Plagioclase core and rim major element compositions

TAN1213 10-1										
Oxides (wt%)	**Core-01**	**Rim-01**	**Core-02**	**Rim-02**	**Core-03**	**Rim-03**	**Core-04**	**Rim-04**	**Core-05**	**Rim-05**
SiO2	52.60	54.30	55.90	56.90	54.10	54.40	52.80	53.20	52.00	54.60
TiO2	0.04	0.03	0.01	0.01	0.02	0.02	0.02	0.02	0.03	0.03
Al2O3	29.50	28.10	27.40	26.90	29.00	28.40	29.50	29.10	29.70	28.40
FeO	1.04	0.87	0.68	0.76	0.89	0.89	0.91	0.89	0.99	0.86
MnO	0.02	0.00	0.00	0.01	0.00	0.01	0.01	0.00	0.01	0.01
MgO	0.10	0.08	0.04	0.03	0.07	0.07	0.11	0.09	0.11	0.06
CaO	12.70	11.10	10.00	9.38	11.80	11.20	12.60	12.40	13.20	11.00
Na2O	4.10	4.93	5.46	5.83	4.50	4.95	4.11	4.35	3.88	4.92
K2O	0.12	0.14	0.21	0.22	0.13	0.16	0.11	0.15	0.09	0.15
Cr2O3	0.01	0.00	0.01	0.00	0.00	0.00	0.00	0.01	0.00	0.00
Total	100.00	99.50	99.70	100.00	101.00	100.00	100.00	100.00	100.00	100.00
Cations										
Si	2.39	2.47	2.53	2.56	2.44	2.46	2.40	2.41	2.37	2.47
Ti	0.00	0.00	0.00	0.00	0.00	0.00	0.00	0.00	0.00	0.00
Al	1.58	1.51	1.46	1.43	1.54	1.51	1.58	1.56	1.59	1.51
Fe (Total)	0.04	0.03	0.03	0.03	0.03	0.03	0.03	0.03	0.04	0.03
Mn	0.00	0.00	0.00	0.00	0.00	0.00	0.00	0.00	0.00	0.00
Mg	0.01	0.01	0.00	0.00	0.00	0.00	0.01	0.01	0.01	0.00
Ca	0.62	0.54	0.49	0.45	0.57	0.54	0.62	0.60	0.65	0.53
Na	0.36	0.44	0.48	0.51	0.39	0.43	0.36	0.38	0.34	0.43
K	0.01	0.01	0.01	0.01	0.01	0.01	0.01	0.01	0.01	0.01
Total	5.00	5.00	5.00	5.00	5.00	5.00	5.00	5.00	5.00	5.00
An	62.80	54.90	49.80	46.40	58.70	55.10	62.60	60.70	65.00	54.70
Ab	36.50	44.30	49.00	52.20	40.50	43.90	36.80	38.40	34.50	44.40
Or	0.71	0.85	1.24	1.32	0.79	0.95	0.66	0.86	0.52	0.91

TAN1213 10-7										
Oxides (wt%)	**Core-01**	**Rim-01**	**Core-02**	**Rim-02**	**Core-03**	**Rim-03**	**Core-04**	**Rim-04**	**Core-05**	**Rim-05**
SiO2	51.40	51.30	49.80	56.20	50.60	52.80	47.40	53.60	48.80	59.30
TiO2	0.02	0.04	0.02	0.03	0.03	0.03	0.01	0.03	0.01	0.02
Al2O3	30.50	30.60	21.00	27.40	31.20	29.70	32.80	29.00	32.30	25.40
FeO	1.02	1.03	5.99	0.71	0.88	1.00	1.34	1.03	0.90	0.55
MnO	0.00	0.01	0.06	0.00	0.00	0.00	0.00	0.01	0.00	0.00
MgO	0.10	0.08	2.77	0.07	0.15	0.09	0.36	0.06	0.14	0.02
CaO	13.70	13.60	7.44	9.73	14.60	12.70	16.60	11.60	15.90	7.44
Na2O	3.58	3.53	3.99	5.57	3.13	4.19	1.89	4.47	2.41	6.62
K2O	0.09	0.09	0.17	0.22	0.08	0.12	0.05	0.21	0.06	0.30
Cr2O3	0.01	0.00	0.00	0.00	0.01	0.02	0.00	0.01	0.02	0.01
Total	100.00	100.00	91.20	100.00	101.00	101.00	100.00	100.00	101.00	99.70
Cations										
Si	2.33	2.34	2.50	2.54	2.30	2.39	2.17	2.43	2.23	2.67
Ti	0.00	0.00	0.00	0.00	0.00	0.00	0.00	0.00	0.00	0.00
Al	1.63	1.64	1.24	1.46	1.67	1.58	1.77	1.55	1.73	1.35
Fe (Total)	0.04	0.04	0.25	0.03	0.03	0.04	0.05	0.04	0.03	0.02
Mn	0.00	0.00	0.00	0.00	0.00	0.00	0.00	0.00	0.00	0.00
Mg	0.01	0.01	0.21	0.00	0.01	0.01	0.02	0.00	0.01	0.00
Ca	0.67	0.66	0.40	0.47	0.71	0.61	0.81	0.57	0.78	0.36
Na	0.32	0.31	0.39	0.49	0.28	0.37	0.17	0.39	0.21	0.58
K	0.01	0.01	0.01	0.01	0.00	0.01	0.00	0.01	0.00	0.02
Total	5.00	5.00	5.00	5.00	5.00	5.00	5.00	5.00	5.00	5.00
An	67.60	67.70	50.10	48.50	71.70	62.10	82.60	58.30	78.20	37.60
Ab	31.90	31.70	48.60	50.20	27.90	37.20	17.10	40.50	21.40	60.50
Or	0.53	0.54	1.34	1.28	0.45	0.68	0.29	1.23	0.35	1.83

TAN1213 10-8	Core-01	Rim-01	Core-02	Rim-02	Core-03	Rim-03	Core-04	Rim-04	Core-05	Rim-05	Core-06	Rim-06
Oxides (wt%)												
SiO2	51.10	49.60	53.70	57.10	55.70	58.00	49.20	48.50	47.20	47.50	53.60	59.00
TiO2	0.03	0.02	0.02	0.02	0.02	0.02	0.02	0.00	0.00	0.01	0.03	0.03
Al2O3	30.40	31.60	29.00	26.60	28.00	26.40	32.10	32.50	33.60	33.40	29.30	26.00
FeO	0.89	0.83	0.69	0.72	0.68	0.62	0.92	0.87	0.96	1.02	0.84	0.71
MnO	0.02	0.02	0.00	0.01	0.00	0.02	0.02	0.00	0.00	0.00	0.00	0.00
MgO	0.10	0.13	0.08	0.06	0.06	0.05	0.13	0.17	0.11	0.09	0.08	0.02
CaO	13.60	15.20	12.00	9.10	10.50	8.64	15.70	16.10	17.00	16.90	12.10	7.93
Na2O	3.58	2.73	4.51	5.94	5.15	6.27	2.64	2.33	1.83	1.92	4.36	6.47
K2O	0.09	0.07	0.14	0.21	0.17	0.22	0.06	0.04	0.04	0.04	0.13	0.28
Cr2O3	0.00	0.00	0.00	0.00	0.00	0.00	0.01	0.00	0.02	0.00	0.00	0.00
Total	99.70	100.00	100.00	99.70	100.00	100.00	101.00	100.00	101.00	101.00	100.00	100.00
Cations												
Si	2.34	2.27	2.44	2.58	2.51	2.60	2.24	2.21	2.15	2.16	2.42	2.64
Ti	0.00	0.00	0.00	0.00	0.00	0.00	0.00	0.00	0.00	0.00	0.00	0.00
Al	1.64	1.70	1.55	1.42	1.49	1.40	1.72	1.75	1.80	1.80	1.56	1.37
Fe (Total)	0.03	0.03	0.03	0.03	0.03	0.02	0.04	0.03	0.04	0.04	0.03	0.03
Mn	0.00	0.00	0.00	0.00	0.00	0.00	0.00	0.00	0.00	0.00	0.00	0.00
Mg	0.01	0.01	0.01	0.00	0.00	0.00	0.01	0.01	0.01	0.01	0.01	0.00
Ca	0.66	0.75	0.58	0.44	0.51	0.42	0.76	0.79	0.83	0.82	0.59	0.38
Na	0.32	0.24	0.40	0.52	0.45	0.55	0.23	0.21	0.16	0.17	0.38	0.56
K	0.01	0.00	0.01	0.01	0.01	0.01	0.00	0.00	0.00	0.00	0.01	0.02
Total	5.00	5.00	5.00	5.00	5.00	5.00	5.00	5.00	5.00	5.00	5.00	5.00
An	67.30	75.20	58.90	45.30	52.50	42.70	76.40	79.10	83.60	82.80	60.10	39.70
Ab	32.10	24.40	40.20	53.50	46.50	56.00	23.30	20.70	16.20	17.00	39.10	58.70
Or	0.53	0.41	0.81	1.24	1.00	1.28	0.36	0.25	0.25	0.22	0.74	1.66

TAN1213 10-10							
Oxides (wt%)	**Core-01**	**Rim-01**	**Core-02**	**Rim-02**	**Core-03**	**Rim-03**	**Core-04**
SiO2	51.60	52.50	53.40	55.70	46.60	46.20	57.70
TiO2	0.04	0.05	0.02	0.02	0.01	0.00	0.00
Al2O3	30.20	30.00	29.40	27.70	34.00	34.40	26.60
FeO	1.06	1.13	0.97	0.84	0.87	0.97	0.52
MnO	0.01	0.02	0.00	0.00	0.00	0.02	0.01
MgO	0.12	0.09	0.06	0.03	0.09	0.10	0.03
CaO	13.60	13.00	12.10	10.30	17.60	18.00	8.59
Na2O	3.69	3.97	4.35	5.39	1.44	1.38	6.30
K2O	0.10	0.16	0.13	0.19	0.04	0.02	0.25
Cr2O3	0.00	0.00	0.00	0.00	0.00	0.00	0.00
Total	100.00	101.00	100.00	100.00	101.00	101.00	100.00
Cations							
Si	2.34	2.37	2.42	2.51	2.13	2.10	2.59
Ti	0.00	0.00	0.00	0.00	0.00	0.00	0.00
Al	1.62	1.59	1.57	1.47	1.83	1.85	1.41
Fe (Total)	0.04	0.04	0.04	0.03	0.03	0.04	0.02
Mn	0.00	0.00	0.00	0.00	0.00	0.00	0.00
Mg	0.01	0.01	0.00	0.00	0.01	0.01	0.00
Ca	0.66	0.63	0.59	0.50	0.86	0.88	0.41
Na	0.33	0.35	0.38	0.47	0.13	0.12	0.55
K	0.01	0.01	0.01	0.01	0.00	0.00	0.01
Total	5.00	5.00	5.00	5.00	5.00	5.00	5.00
An	66.60	63.90	60.10	50.70	86.90	87.70	42.30
Ab	32.80	35.20	39.20	48.20	12.90	12.20	56.20
Or	0.60	0.93	0.76	1.12	0.21	0.13	1.47

Table A-3: Clinopyroxene major element compositions

TAN1213 10-1										
Oxides (wt%)	**Pyroxene-01**	**Pyroxene-02**	**Pyroxene-03**	**Pyroxene-04**	**Pyroxene-05**	**Pyroxene-06**	**Pyroxene-07**	**Pyroxene-08**	**Pyroxene-09**	**Pyroxene-10**
SiO2	50.90	51.20	50.90	50.70	51.30	50.80	51.50	50.80	50.70	51.10
TiO2	0.61	0.38	0.42	0.60	0.40	0.53	0.36	0.48	0.50	0.46
Al2O3	2.41	1.67	1.69	3.19	1.61	2.13	1.65	1.74	1.65	2.05
Fe2O3	2.23	2.35	1.65	2.81	1.49	2.24	2.29	1.51	1.74	2.16
FeO	11.90	16.20	16.60	10.50	16.60	13.90	15.20	14.10	16.70	13.90
MnO	0.34	0.53	0.54	0.32	0.53	0.44	0.52	0.39	0.48	0.47
MgO	12.70	14.30	13.60	14.00	13.40	13.20	14.20	11.50	10.70	13.20
CaO	20.00	14.60	15.00	19.00	15.50	17.50	15.60	19.70	18.80	17.70
Na2O	0.21	0.17	0.15	0.24	0.17	0.21	0.20	0.19	0.18	0.22
K2O	0.00	0.00	0.01	0.00	0.01	0.01	0.00	0.00	0.00	0.00
Cr2O3	0.00	0.00	0.01	0.00	0.02	0.00	0.00	0.00	0.01	0.00
Total	101.00	101.00	101.00	101.00	101.00	101.00	102.00	100.00	101.00	101.00
Cations										
Si	1.91	1.93	1.93	1.88	1.94	1.91	1.93	1.93	1.93	1.92
Ti	0.02	0.01	0.01	0.02	0.01	0.01	0.01	0.01	0.01	0.01
Al	0.11	0.07	0.08	0.14	0.07	0.09	0.07	0.08	0.07	0.09
Fe3+	0.06	0.07	0.05	0.08	0.04	0.06	0.06	0.04	0.05	0.06
Fe2+	0.37	0.51	0.53	0.33	0.52	0.44	0.48	0.45	0.53	0.44
Mn	0.01	0.02	0.02	0.01	0.02	0.01	0.02	0.01	0.02	0.02
Mg	0.71	0.80	0.77	0.77	0.76	0.74	0.79	0.66	0.61	0.74
Ca	0.80	0.59	0.61	0.76	0.63	0.71	0.63	0.80	0.77	0.71
Na	0.02	0.01	0.01	0.02	0.01	0.02	0.01	0.01	0.01	0.02
Total	4.00	4.00	4.00	4.00	4.00	4.00	4.00	4.00	4.00	4.00
Wo	41.30	29.90	31.20	39.10	32.20	36.20	31.90	41.20	39.20	36.50
En	36.30	40.70	39.40	40.00	38.80	38.10	40.60	33.60	31.00	37.90
Fs	22.40	29.40	29.40	20.90	29.00	25.70	27.50	25.20	29.80	25.60
Mg#	65.20	60.80	59.00	70.00	58.80	62.60	62.30	59.10	52.90	62.40

TAN1213 10-7									
Oxides (wt%)	**Pyroxene-01**	**Pyroxene-02**	**Pyroxene-03**	**Pyroxene-04**	**Pyroxene-05**	**Pyroxene-06**	**Pyroxene-07**	**Pyroxene-08**	**Pyroxene-09**
SiO2	52.90	52.80	51.10	52.40	52.80	51.60	52.20	52.60	52.70
TiO2	0.27	0.32	0.40	0.31	0.34	0.44	0.37	0.33	0.33
Al2O3	2.12	2.37	1.61	2.24	2.30	2.32	2.11	2.21	2.00
Fe2O3	1.93	2.07	1.53	2.09	2.14	2.88	2.33	1.78	1.43
FeO	7.39	6.67	13.30	7.92	7.43	9.60	8.77	7.97	8.92
MnO	0.26	0.24	0.41	0.28	0.23	0.35	0.28	0.22	0.27
MgO	16.60	16.40	13.00	16.00	16.20	15.10	15.50	16.00	15.80
CaO	19.80	20.60	18.40	19.70	20.20	18.70	19.50	20.00	19.50
Na2O	0.19	0.20	0.21	0.18	0.21	0.29	0.22	0.19	0.20
K2O	0.00	0.01	0.00	0.00	0.00	0.01	0.00	0.00	0.00
Cr2O3	0.05	0.08	0.01	0.01	0.03	0.00	0.00	0.02	0.00
Total	102.00	102.00	100.00	101.00	102.00	101.00	101.00	101.00	101.00
Cations									
Si	1.93	1.92	1.94	1.92	1.92	1.91	1.92	1.93	1.94
Ti	0.01	0.01	0.01	0.01	0.01	0.01	0.01	0.01	0.01
Al	0.09	0.10	0.07	0.10	0.10	0.10	0.09	0.10	0.09
Fe3+	0.05	0.06	0.04	0.06	0.06	0.08	0.06	0.05	0.04
Fe2+	0.23	0.20	0.42	0.24	0.23	0.30	0.27	0.24	0.27
Mn	0.01	0.01	0.01	0.01	0.01	0.01	0.01	0.01	0.01
Mg	0.90	0.89	0.74	0.88	0.88	0.83	0.85	0.87	0.87
Ca	0.77	0.80	0.75	0.77	0.79	0.74	0.77	0.78	0.77
Na	0.01	0.01	0.02	0.01	0.01	0.02	0.02	0.01	0.01
Total	4.00	4.00	4.00	4.00	4.00	4.00	4.00	4.00	4.00
Wo	39.60	41.10	38.40	39.70	40.30	38.00	39.40	40.20	39.40
En	46.20	45.60	37.80	45.00	45.10	42.60	43.50	44.80	44.50
Fs	14.20	13.30	23.80	15.40	14.60	19.30	17.10	15.00	16.10
Mg#	79.80	81.20	63.40	78.10	79.40	73.40	75.70	78.00	75.80

TAN1213 10-8							
Oxides (wt%)	**Pyroxene-01**	**Pyroxene-02**	**Pyroxene-03**	**Pyroxene-04**	**Pyroxene-05**	**Pyroxene-06**	**Pyroxene-07**
SiO2	52.60	52.20	51.90	51.60	53.30	53.00	52.70
TiO2	0.34	0.39	0.39	0.41	0.27	0.28	0.35
Al2O3	2.17	1.93	2.09	2.70	1.89	1.88	2.00
Fe2O3	2.22	2.18	2.20	1.87	1.24	1.58	2.15
FeO	7.95	9.97	9.87	7.83	7.58	7.52	7.94
MnO	0.24	0.32	0.32	0.23	0.29	0.27	0.27
MgO	16.10	15.30	15.40	15.60	16.60	16.60	16.00
CaO	19.70	19.00	18.60	19.70	19.90	19.90	20.10
Na2O	0.22	0.21	0.22	0.21	0.19	0.18	0.19
K2O	0.00	0.00	0.00	0.00	0.00	0.00	0.01
Cr2O3	0.00	0.01	0.00	0.03	0.04	0.04	0.02
Total	102.00	101.00	101.00	100.00	101.00	101.00	102.00
Cations							
Si	1.92	1.92	1.92	1.91	1.94	1.94	1.92
Ti	0.01	0.01	0.01	0.01	0.01	0.01	0.01
Al	0.09	0.08	0.09	0.12	0.08	0.08	0.09
Fe3+	0.06	0.06	0.06	0.05	0.03	0.04	0.06
Fe2+	0.24	0.31	0.31	0.24	0.23	0.23	0.24
Mn	0.01	0.01	0.01	0.01	0.01	0.01	0.01
Mg	0.88	0.84	0.85	0.86	0.90	0.90	0.87
Ca	0.77	0.75	0.74	0.78	0.78	0.78	0.79
Na	0.02	0.02	0.02	0.02	0.01	0.01	0.01
Total	4.00	4.00	4.00	4.00	4.00	4.00	4.00
Wo	39.50	38.30	37.80	40.30	40.00	39.90	40.20
En	44.90	42.90	43.40	44.50	46.40	46.20	44.40
Fs	15.60	18.80	18.80	15.20	13.60	14.00	15.40
Mg#	78.10	72.90	73.30	77.90	79.40	79.50	78.00

TAN1213 10-10					
Oxides (wt%)	**Pyroxene-01**	**Pyroxene-02**	**Pyroxene-03**	**Pyroxene-04**	**Pyroxene-05**
SiO2	52.70	51.50	52.20	52.90	52.90
TiO2	0.33	0.46	0.35	0.32	0.32
Al2O3	1.97	2.42	1.67	1.98	2.33
Fe2O3	1.72	2.90	1.97	1.65	1.71
FeO	8.15	9.52	11.10	8.38	7.38
MnO	0.26	0.34	0.42	0.27	0.21
MgO	16.10	14.90	15.20	16.10	16.40
CaO	19.80	19.00	18.00	19.70	20.10
Na2O	0.21	0.26	0.22	0.19	0.22
K2O	0.00	0.01	0.00	0.01	0.00
Cr2O3	0.00	0.02	0.01	0.02	0.04
Total	101.00	101.00	101.00	102.00	102.00
Cations					
Si	1.93	1.90	1.93	1.93	1.92
Ti	0.01	0.01	0.01	0.01	0.01
Al	0.09	0.11	0.07	0.09	0.10
Fe3+	0.05	0.08	0.05	0.05	0.05
Fe2+	0.25	0.29	0.34	0.26	0.23
Mn	0.01	0.01	0.01	0.01	0.01
Mg	0.88	0.82	0.84	0.88	0.89
Ca	0.78	0.75	0.71	0.77	0.78
Na	0.01	0.02	0.02	0.01	0.02
Total	4.00	4.00	4.00	4.00	4.00
Wo	39.80	38.50	36.50	39.50	40.40
En	45.00	42.20	43.10	45.10	45.70
Fs	15.20	19.20	20.40	15.40	14.00
Mg#	77.60	73.40	70.70	77.20	79.60

Table A-4: Major element compositions of clinopyroxenes selected for LA-ICP-MS

TAN1213 10-1										
Oxides (wt%)	**Pyroxene-01LA**	**Pyroxene-02LA**	**Pyroxene-03LA**	**Pyroxene-04LA**	**Pyroxene-05LA**	**Pyroxene-06LA**	**Pyroxene-07LA**	**Pyroxene-08LA**	**Pyroxene-09LA**	**Pyroxene-10LA**
SiO2	50.80	50.80	51.20	51.70	51.10	51.00	50.60	50.80	50.80	50.70
TiO2	0.55	0.48	0.50	0.40	0.52	0.47	0.50	0.40	0.53	0.56
Al2O3	3.08	2.75	2.04	2.06	2.18	1.90	2.30	1.69	2.09	2.12
Fe2O3	3.02	1.57	2.12	1.84	1.78	2.28	2.43	3.34	2.23	2.35
FeO	10.20	10.50	12.70	13.70	14.10	13.60	13.90	16.40	13.80	13.40
MnO	0.30	0.30	0.36	0.39	0.41	0.37	0.42	0.51	0.38	0.38
MgO	13.90	14.20	12.70	15.80	12.60	12.70	14.20	13.60	12.40	12.10
CaO	19.30	18.70	19.50	14.90	18.40	18.60	15.70	14.30	18.70	19.00
Na2O	0.25	0.23	0.22	0.19	0.23	0.21	0.27	0.34	0.22	0.30
K2O	0.00	0.02	0.01	0.00	0.01	0.01	0.00	0.13	0.00	0.03
Cr2O3	0.02	0.00	0.00	0.01	0.00	0.00	0.01	0.01	0.00	0.00
Total	101.00	99.50	101.00	101.00	101.00	101.00	100.00	102.00	101.00	101.00
Cations										
Si	1.88	1.91	1.92	1.92	1.92	1.92	1.91	1.92	1.92	1.91
Ti	0.02	0.01	0.01	0.01	0.01	0.01	0.01	0.01	0.02	0.02
Al	0.14	0.12	0.09	0.09	0.10	0.08	0.10	0.08	0.09	0.09
Fe3+	0.08	0.04	0.06	0.05	0.05	0.06	0.07	0.09	0.06	0.07
Fe2+	0.32	0.33	0.40	0.43	0.44	0.43	0.44	0.52	0.44	0.42
Mn	0.01	0.01	0.01	0.01	0.01	0.01	0.01	0.02	0.01	0.01
Mg	0.77	0.80	0.71	0.88	0.71	0.71	0.80	0.77	0.70	0.68
Ca	0.77	0.76	0.78	0.59	0.74	0.75	0.63	0.58	0.76	0.77
Na	0.02	0.02	0.02	0.01	0.02	0.02	0.02	0.02	0.02	0.02
Total	4.00	4.00	4.00	4.00	4.00	4.00	4.00	4.00	4.00	4.00
Wo	39.50	39.20	40.10	30.40	38.10	38.50	32.70	29.60	38.80	39.60
En	39.80	41.40	36.50	45.10	36.50	36.40	41.10	39.10	35.70	35.20
Fs	20.70	19.40	23.40	24.50	25.40	25.20	26.20	31.30	25.50	25.20
Mg#	70.60	70.50	63.90	67.10	61.30	62.20	64.20	59.40	61.20	61.40

TAN1213 10-7										
Oxides (wt%)	**Pyroxene-01LA**	**Pyroxene-02LA**	**Pyroxene-03LA**	**Pyroxene-04LA**	**Pyroxene-05LA**	**Pyroxene-06LA**	**Pyroxene-07LA**	**Pyroxene-08LA**	**Pyroxene-09LA**	**Pyroxene-10LA**
SiO2	51.50	52.30	51.60	52.70	52.70	52.20	52.50	52.30	52.40	51.40
TiO2	0.36	0.27	0.36	0.28	0.29	0.24	0.25	0.39	0.27	0.42
Al2O3	2.01	2.10	2.52	1.82	1.75	2.18	2.37	1.75	2.03	2.31
Fe2O3	2.48	2.10	2.56	1.81	2.08	2.12	2.20	1.70	2.40	2.50
FeO	10.80	7.00	9.18	8.20	8.25	7.95	6.29	11.90	6.70	9.78
MnO	0.31	0.22	0.30	0.26	0.22	0.22	0.23	0.34	0.23	0.27
MgO	14.50	16.40	16.00	16.40	16.40	16.00	16.70	14.80	16.50	14.70
CaO	18.80	19.80	18.10	19.20	19.20	19.60	20.20	18.10	19.90	19.10
Na2O	0.20	0.21	0.19	0.19	0.19	0.20	0.19	0.21	0.21	0.23
K2O	0.00	0.00	0.01	0.01	0.02	0.00	0.00	0.00	0.00	0.01
Cr2O3	0.03	0.02	0.00	0.01	0.03	0.01	0.12	0.01	0.03	0.01
Total	101.00	100.00	101.00	101.00	101.00	101.00	101.00	102.00	101.00	101.00
Cations										
Si	1.92	1.93	1.91	1.93	1.93	1.92	1.92	1.93	1.92	1.91
Ti	0.01	0.01	0.01	0.01	0.01	0.01	0.01	0.01	0.01	0.01
Al	0.09	0.09	0.11	0.08	0.08	0.09	0.10	0.08	0.09	0.10
Fe3+	0.07	0.06	0.07	0.05	0.06	0.06	0.06	0.05	0.07	0.07
Fe2+	0.34	0.22	0.28	0.25	0.25	0.25	0.19	0.37	0.21	0.30
Mn	0.01	0.01	0.01	0.01	0.01	0.01	0.01	0.01	0.01	0.01
Mg	0.81	0.90	0.88	0.90	0.90	0.88	0.91	0.82	0.90	0.82
Ca	0.75	0.78	0.72	0.76	0.75	0.77	0.79	0.72	0.79	0.76
Na	0.01	0.02	0.01	0.01	0.01	0.01	0.01	0.02	0.01	0.02
Total	4.00	4.00	4.00	4.00	4.00	4.00	4.00	4.00	4.00	4.00
Wo	38.20	40.00	36.80	38.70	38.40	39.60	40.40	36.80	40.00	39.00
En	41.10	46.00	45.10	45.90	45.80	44.80	46.60	41.90	46.10	41.80
Fs	20.70	14.00	18.20	15.40	15.80	15.50	12.90	21.30	13.90	19.20
Mg#	70.30	80.40	75.40	77.90	77.80	77.90	82.40	68.70	81.30	72.60

TAN1213 10-8										
Oxides (wt%)	**Pyroxene-01LA**	**Pyroxene-02LA**	**Pyroxene-03LA**	**Pyroxene-04LA**	**Pyroxene-05LA**	**Pyroxene-06LA**	**Pyroxene-07LA**	**Pyroxene-08LA**	**Pyroxene-09LA**	**Pyroxene-10LA**
SiO2	51.50	52.10	51.50	52.50	51.60	52.00	51.50	51.30	50.50	52.10
TiO2	0.39	0.29	0.39	0.25	0.33	0.32	0.36	0.41	0.52	0.32
Al2O3	2.28	2.28	1.97	1.83	2.14	2.04	2.18	2.30	3.33	2.08
Fe2O3	2.22	2.26	2.43	1.94	2.32	2.49	2.36	2.72	2.63	2.09
FeO	8.83	7.17	10.40	7.29	8.80	8.16	9.28	9.02	9.44	7.52
MnO	0.25	0.22	0.33	0.26	0.27	0.28	0.29	0.25	0.25	0.23
MgO	15.00	16.20	14.80	16.40	15.50	15.60	15.10	15.00	14.50	15.90
CaO	19.50	19.70	18.50	19.70	19.00	19.60	19.00	19.20	19.00	19.90
Na2O	0.23	0.20	0.21	0.19	0.21	0.22	0.23	0.23	0.23	0.19
K2O	0.00	0.00	0.01	0.00	0.00	0.02	0.00	0.00	0.02	0.00
Cr2O3	0.00	0.07	0.00	0.04	0.00	0.01	0.00	0.01	0.00	0.04
Total	100.00	100.00	101.00	100.00	100.00	101.00	100.00	100.00	100.00	100.00
Cations										
Si	1.92	1.92	1.92	1.93	1.92	1.92	1.92	1.91	1.88	1.92
Ti	0.01	0.01	0.01	0.01	0.01	0.01	0.01	0.01	0.01	0.01
Al	0.10	0.10	0.09	0.08	0.09	0.09	0.10	0.10	0.15	0.09
Fe3+	0.06	0.06	0.07	0.05	0.06	0.07	0.07	0.08	0.07	0.06
Fe2+	0.28	0.22	0.33	0.23	0.27	0.25	0.29	0.28	0.29	0.23
Mn	0.01	0.01	0.01	0.01	0.01	0.01	0.01	0.01	0.01	0.01
Mg	0.83	0.89	0.83	0.90	0.86	0.86	0.84	0.83	0.80	0.88
Ca	0.78	0.78	0.74	0.78	0.76	0.78	0.76	0.77	0.76	0.79
Na	0.02	0.01	0.01	0.01	0.02	0.02	0.02	0.02	0.02	0.01
Total	4.00	4.00	4.00	4.00	4.00	4.00	4.00	4.00	4.00	4.00
Wo	39.90	39.90	37.80	39.80	38.80	39.60	38.90	39.30	39.30	40.20
En	42.80	45.60	42.20	46.00	43.90	43.90	43.00	42.50	41.60	44.90
Fs	17.30	14.50	20.10	14.20	17.30	16.40	18.20	18.30	19.00	14.80
Mg#	75.00	79.90	71.50	79.90	75.60	77.10	74.20	74.50	73.00	78.90

TAN1213 10-10						
Oxides (wt%)	**Pyroxene-01LA**	**Pyroxene-02LA**	**Pyroxene-04LA**	**Pyroxene-05LA**	**Pyroxene-07LA**	**Pyroxene-08LA**
SiO2	52.20	52.70	52.90	52.50	51.00	51.70
TiO2	0.31	0.27	0.19	0.26	0.46	0.36
Al2O3	2.28	1.97	2.66	2.01	2.32	1.59
Fe2O3	1.89	1.26	1.23	1.68	2.11	2.07
FeO	8.17	8.69	4.81	6.93	11.00	11.60
MnO	0.22	0.27	0.13	0.20	0.31	0.37
MgO	15.80	16.50	16.70	16.40	14.20	14.60
CaO	19.70	18.70	21.80	20.00	18.60	17.80
Na2O	0.21	0.19	0.18	0.20	0.22	0.28
K2O	0.00	0.01	0.01	0.02	0.01	0.03
Cr2O3	0.00	0.04	0.12	0.05	0.00	0.00
Total	101.00	101.00	101.00	100.00	100.00	101.00
Cations						
Si	1.92	1.94	1.93	1.93	1.91	1.94
Ti	0.01	0.01	0.01	0.01	0.01	0.01
Al	0.10	0.09	0.11	0.09	0.10	0.07
Fe3+	0.05	0.03	0.03	0.05	0.06	0.06
Fe2+	0.25	0.27	0.15	0.21	0.34	0.36
Mn	0.01	0.01	0.00	0.01	0.01	0.01
Mg	0.87	0.91	0.91	0.90	0.80	0.82
Ca	0.78	0.74	0.85	0.79	0.75	0.72
Na	0.02	0.01	0.01	0.01	0.02	0.02
Total	4.00	4.00	4.00	4.00	4.00	4.00
Wo	39.90	38.00	43.90	40.50	38.40	36.60
En	44.50	46.50	46.70	46.10	40.90	41.80
Fs	15.60	15.50	9.31	13.30	20.70	21.60
Mg#	77.20	77.00	85.90	80.60	69.60	69.00

Table A-5: Amphibole major element compositions.
Species ID from Locock (2014).

TAN1213 10-7						
Oxides (wt%)	**Amphibole-01 Rim**	**Amphibole-01 Core**	**Amphibole-02 Core**	**Amphibole-02 Rim**	**Amphibole-02 Rim**	**Amphibole-03**
Species	Hastingsite	Ti-rich Hastingsite	Hastingsite	Hastingsite	Hastingsite	Hastingsite
SiO2	38.60	38.20	41.30	41.60	41.60	40.10
TiO2	2.31	2.85	1.30	1.56	1.12	1.97
Al2O3	8.31	8.49	5.69	5.52	5.61	6.67
FeO	29.70	28.80	31.00	30.70	31.10	31.50
Fe2O3	4.62	4.91	3.32	2.69	4.40	3.64
MnO	0.38	0.38	0.48	0.40	0.49	0.54
MgO	0.78	1.20	1.36	1.83	1.39	0.88
CaO	9.91	9.33	8.93	9.34	8.43	8.85
Na2O	2.02	2.20	1.83	1.89	1.82	1.96
K2O	0.95	0.90	0.96	0.96	0.83	1.09
Cr2O3	0.01	0.02	0.00	0.01	0.00	0.01
H20+	1.84	1.84	1.85	1.85	1.85	1.83
Total	99.40	99.20	98.00	98.40	98.60	99.10

Table A-6: Major element compositions of Fe-Ti oxides

TAN1213 10-1										
Oxides (wt%)										
	Magnetite-01	Magnetite-02	Magnetite-03	Magnetite-04	Magnetite-05	Magnetite-06	Magnetite-07	Magnetite-08	Magnetite-09	Magnetite-10
TiO2	17.90	18.50	17.70	18.30	18.10	17.70	18.60	18.00	18.60	18.30
Al2O3	1.81	2.01	1.68	1.95	1.86	1.93	2.15	1.90	1.97	1.81
FeO	45.50	47.20	46.00	46.20	46.70	46.40	47.40	46.50	46.30	46.50
Fe2O3	28.20	27.30	28.90	27.80	28.00	28.40	26.90	28.00	27.30	27.40
MnO	1.70	0.61	0.83	1.55	0.75	0.47	0.62	0.81	1.70	0.85
MgO	0.10	0.16	0.12	0.12	0.12	0.16	0.12	0.11	0.12	0.19
Cr2O3	0.02	0.04	0.02	0.03	0.04	0.03	0.03	0.03	0.03	0.03
V2O3	2.42	2.50	2.35	2.43	2.46	2.38	2.49	2.51	2.48	2.47
Total	97.60	98.30	97.60	98.30	98.00	97.50	98.40	97.90	98.40	97.50
Cations										
Ti	0.52	0.53	0.51	0.52	0.52	0.51	0.53	0.52	0.53	0.53
Al	0.08	0.09	0.08	0.09	0.08	0.09	0.10	0.09	0.09	0.08
Fe+3	0.81	0.78	0.83	0.79	0.80	0.82	0.77	0.80	0.78	0.79
Fe+2	1.45	1.50	1.48	1.47	1.49	1.49	1.50	1.48	1.47	1.49
Mn	0.06	0.02	0.03	0.05	0.02	0.02	0.02	0.03	0.05	0.03
Mg	0.01	0.01	0.01	0.01	0.01	0.01	0.01	0.01	0.01	0.01
Cr	0.00	0.00	0.00	0.00	0.00	0.00	0.00	0.00	0.00	0.00
V	0.07	0.08	0.07	0.07	0.08	0.07	0.08	0.08	0.08	0.08
Total	3.00	3.00	3.00	3.00	3.00	3.00	3.00	3.00	3.00	3.00

TAN1213 10-1										
Oxides (wt%)										
	Magnetite-11	Magnetite-12	Magnetite-13	Magnetite-14	Magnetite-15	Magnetite-16	Magnetite-17	Magnetite-18	Magnetite-19	Magnetite-20
TiO2	18.10	17.50	18.00	17.80	17.70	17.70	17.90	18.10	18.00	17.80
Al2O3	1.80	1.99	2.06	1.85	2.04	1.78	1.96	1.78	1.67	1.80
FeO	45.80	45.30	46.00	45.80	46.50	46.10	46.10	46.20	46.50	46.80
Fe2O3	28.70	28.70	28.50	28.50	28.80	28.70	28.70	28.70	29.20	29.30
MnO	1.97	1.44	1.53	1.28	0.68	0.75	1.29	1.36	0.94	0.55
MgO	0.08	0.12	0.17	0.14	0.18	0.19	0.11	0.13	0.13	0.10
Cr2O3	0.04	0.03	0.03	0.03	0.05	0.04	0.02	0.00	0.00	0.04
V2O3	2.37	2.46	2.45	2.49	2.52	2.51	2.42	2.38	2.32	2.39
Total	98.80	97.60	98.80	97.90	98.50	97.80	98.40	98.60	98.70	98.70
Cations										
Ti	0.52	0.50	0.51	0.51	0.51	0.51	0.51	0.52	0.51	0.51
Al	0.08	0.09	0.09	0.08	0.09	0.08	0.09	0.08	0.07	0.08
Fe+3	0.82	0.83	0.81	0.82	0.82	0.83	0.82	0.82	0.83	0.84
Fe+2	1.45	1.45	1.45	1.46	1.47	1.47	1.46	1.46	1.47	1.48
Mn	0.06	0.05	0.05	0.04	0.02	0.02	0.04	0.04	0.03	0.02
Mg	0.00	0.01	0.01	0.01	0.01	0.01	0.01	0.01	0.01	0.01
Cr	0.00	0.00	0.00	0.00	0.00	0.00	0.00	0.00	0.00	0.00
V	0.07	0.08	0.07	0.08	0.08	0.08	0.07	0.07	0.07	0.07
Total	3.00	3.00	3.00	3.00	3.00	3.00	3.00	3.00	3.00	3.00

TAN1213 10-7						
Oxides (wt%)						
	Magnetite-01	Magnetite-02	Magnetite-03	Magnetite-04	Magnetite-05	Magnetite-06
TiO2	16.60	16.60	19.30	20.10	17.60	19.60
Al2O3	1.92	2.25	0.41	0.94	1.41	1.15
FeO	45.90	45.40	47.10	47.00	46.60	45.90
Fe2O3	32.70	32.50	27.50	26.50	30.60	25.40
MnO	0.36	0.38	1.05	2.53	0.38	2.23
MgO	0.43	0.83	0.22	0.19	0.33	0.36
Cr2O3	0.02	0.03	0.02	0.01	0.03	0.00
V2O3	2.15	2.41	2.37	2.46	2.38	2.59
Total	100.00	100.00	97.90	99.80	99.40	97.20
Cations						
Ti	0.47	0.46	0.56	0.57	0.50	0.57
Al	0.08	0.10	0.02	0.04	0.06	0.05
Fe+3	0.92	0.90	0.79	0.75	0.87	0.73
Fe+2	1.43	1.40	1.51	1.48	1.47	1.47
Mn	0.01	0.01	0.03	0.08	0.01	0.07
Mg	0.02	0.05	0.01	0.01	0.02	0.02
Cr	0.00	0.00	0.00	0.00	0.00	0.00
V	0.06	0.07	0.07	0.07	0.07	0.08
Total	3.00	3.00	3.00	3.00	3.00	3.00

TAN1213 10-8				
Oxides (wt%)				
	Magnetite-01	Magnetite-02	Magnetite-03	Magnetite-04
TiO2	18.20	18.70	19.60	19.70
Al2O3	1.80	1.91	1.85	1.57
FeO	47.00	47.70	47.90	49.00
Fe2O3	28.60	28.30	25.00	26.70
MnO	0.50	0.42	0.50	0.41
MgO	0.34	0.41	0.38	0.17
Cr2O3	0.04	0.01	0.03	0.02
V2O3	2.58	2.48	2.47	2.47
Total	99.00	99.80	97.80	100.00
Cations				
Ti	0.52	0.52	0.56	0.55
Al	0.08	0.08	0.08	0.07
Fe+3	0.81	0.79	0.72	0.75
Fe+2	1.48	1.49	1.52	1.53
Mn	0.02	0.01	0.02	0.01
Mg	0.02	0.02	0.02	0.01
Cr	0.00	0.00	0.00	0.00
V	0.08	0.07	0.08	0.07
Total	3.00	3.00	3.00	3.00

TAN1213 10-10						
Oxides (wt%)						
	Magnetite-01	Magnetite-02	Magnetite-03	Magnetite-04	Magnetite-05	Magnetite-06
TiO2	17.30	17.60	19.30	20.10	17.60	19.60
Al2O3	1.16	1.28	0.41	0.94	1.41	1.15
FeO	46.70	45.80	47.10	47.00	46.60	45.90
Fe2O3	32.30	29.80	27.50	26.50	30.60	25.40
MnO	0.39	0.75	1.05	2.53	0.38	2.23
MgO	0.29	0.32	0.22	0.19	0.33	0.36
Cr2O3	0.02	0.02	0.02	0.01	0.03	0.00
V2O3	2.35	2.36	2.37	2.46	2.38	2.59
Total	101.00	97.80	97.90	99.80	99.40	97.20
Cations						
Ti	0.49	0.51	0.56	0.57	0.50	0.57
Al	0.05	0.06	0.02	0.04	0.06	0.05
Fe+3	0.91	0.86	0.79	0.75	0.87	0.73
Fe+2	1.46	1.46	1.51	1.48	1.47	1.47
Mn	0.01	0.02	0.03	0.08	0.01	0.07
Mg	0.02	0.02	0.01	0.01	0.02	0.02
Cr	0.00	0.00	0.00	0.00	0.00	0.00
V	0.07	0.07	0.07	0.07	0.07	0.08
Total	3.00	3.00	3.00	3.00	3.00	3.00

Appendix 2 Clinopyroxene Trace Element Data

Table A-7: Clinopyroxene trace element concentrations.

TAN1213 10-1	Pyroxene-01LA	Pyroxene-02LA	Pyroxene-03LA	Pyroxene-04ALA	Pyroxene-04BLA	Pyroxene-05LA	Pyroxene-06LA	Pyroxene-07LA	Pyroxene-08LA	Pyroxene-09LA	Pyroxene-10LA
Li	2.86	2.71	1.94	1.68	1.94	2.45	2.18	2.45	2.69	3.70	3.30
Sc	183.00	163.00	189.00	133.00	124.00	207.00	197.00	156.00	147.00	232.00	216.00
Ti	3330.00	3030.00	3270.00	2510.00	2440.00	3240.00	3130.00	3090.00	2450.00	3400.00	3200.00
V	601.00	529.00	483.00	409.00	390.00	394.00	396.00	463.00	284.00	327.00	314.00
Cr	1.50	2.56	bdl	bdl	bdl	bdl	bdl	bdl	bdl	bdl	bdl
Co	56.30	67.50	58.30	65.60	63.80	58.40	57.10	81.90	63.60	72.60	63.50
Ni	17.90	23.60	7.15	19.10	15.50	4.81	4.57	9.48	5.10	5.77	5.01
Cu	1.60	0.82	0.44	0.46	0.53	1.11	1.22	0.64	14.20	124.00	1.70
Zn	55.50	73.50	72.90	75.50	72.30	83.30	78.50	120.00	96.80	120.00	92.70
Ga	6.59	5.60	5.53	4.43	4.77	5.73	5.48	5.17	4.30	6.56	5.40
Rb	bdl	bdl	bdl	bdl	bdl	0.04	0.07	bdl	0.07	0.18	0.09
Sr86						20.10	20.80	10.30	12.40		22.40
Sr88	18.50	14.80	21.70	9.04	9.33					26.10	
Y	26.20	20.70	28.60	16.80	17.60	31.70	30.40	23.20	22.00	41.20	36.40
Zr	13.80	9.11	13.90	6.66	7.38	17.50	16.00	9.47	11.80	22.20	17.70
Nb	0.01	0.01	0.01	0.00	0.00	0.01	0.01	0.00	0.02	0.01	0.01
Mo	bdl	bdl	0.01	0.02	0.02	0.01	0.01	0.01	0.02	bdl	0.01
Ba	0.07	0.06	0.03	0.09	0.13	0.11	0.40	0.07	1.97	0.96	0.74
La	0.61	0.51	0.77	0.24	0.27	0.88	0.98	0.36	0.53	1.18	1.16
Ce	2.82	2.12	3.44	1.19	1.40	4.00	4.38	1.81	2.51	5.22	5.02
Pr	0.63	0.54	0.89	0.32	0.34	1.02	1.07	0.47	0.63	1.32	1.32
Nd	4.37	3.49	6.38	2.17	2.20	7.05	7.19	3.51	4.22	9.10	8.66
Sm	2.39	1.55	2.97	1.15	1.23	3.50	3.37	1.82	2.14	4.44	3.82
Eu	0.78	0.61	0.83	0.47	0.44	0.91	0.92	0.60	0.59	0.98	1.00
Gd	3.58	2.87	4.64	1.96	2.16	5.04	5.08	3.05	3.37	6.21	6.14
Tb	0.64	0.50	0.80	0.40	0.39	0.90	0.89	0.57	0.60	1.17	1.04
Dy	4.65	3.71	5.40	2.76	2.89	6.67	6.50	4.44	4.34	7.71	9.41
Ho	0.99	0.79	1.07	0.68	0.66	1.32	1.28	0.96	0.96	1.54	1.47
Er	2.64	2.41	3.14	1.87	1.93	3.68	3.52	2.88	2.80	4.38	4.37
Tm	0.38	0.32	0.44	0.28	0.27	0.54	0.51	0.43	0.42	0.69	0.61
Yb	2.26	2.19	2.63	1.75	1.74	3.33	3.05	2.82	2.57	4.20	3.63
Lu	0.36	0.30	0.41	0.29	0.29	0.51	0.49	0.44	0.42	0.63	0.52
Hf	0.78	0.45	0.80	0.35	0.42	0.94	0.87	0.48	0.55	1.11	0.88
Ta	bdl	bdl	bdl	bdl	bdl	0.00	0.00	0.00	0.00	bdl	0.00
Pb	bdl	bdl	0.06	bdl	bdl	0.05	0.06	0.02	0.11	0.06	
Th	0.01	0.04	0.02	0.00	0.00	0.01	0.02	0.01	0.02	0.01	0.03
U	bdl	0.02	0.01	bdl	0.01	0.03	0.01	0.01	0.18	0.20	0.02

TAN1213 10-7	Pyroxene-01LA	Pyroxene-02LA	Pyroxene-03LA	Pyroxene-04LA	Pyroxene-05LA	Pyroxene-06BLA	Pyroxene-07LA	Pyroxene-08LA	Pyroxene-09LA	Pyroxene-10LA
Li	2.51	1.97	1.47	2.98	1.82	2.02	3.39	2.71	1.61	2.87
Sc	159.00	131.00	126.00	125.00	105.00	115.00	134.00	144.00	129.00	142.00
Ti	3130.00	2400.00	2270.00	2120.00	1750.00	1970.00	2360.00	2670.00	2130.00	2620.00
V	588.00	364.00	405.00	350.00	307.00	346.00	387.00	468.00	336.00	459.00
Cr	9.78	478.00	146.00	140.00	211.00	186.00	121.00	0.69	246.00	17.50
Co	54.30	50.90	47.90	52.70	48.20	49.60	55.20	58.30	51.90	54.30
Ni	37.40	65.40	52.20	60.90	55.50	53.80	62.00	31.30	64.30	38.50
Cu	4.61	0.94	1.70	4.48	2.13	2.96	5.40	2.83	2.02	5.94
Zn	59.10	44.90	40.40	42.30	39.70	40.40	46.70	73.50	38.80	52.30
Ga	5.14	4.21	4.04	3.66	3.53	4.13	3.91	4.70	3.97	4.94
Rb	0.04	0.07	bdl	bdl	0.08	bdl	0.08	bdl	bdl	0.17
Sr86	19.90	23.00	17.10	14.90	14.80	15.80	16.60	16.00	15.30	15.50
Sr88										
Y	17.80	12.30	11.80	11.10	10.60	11.90	12.10	22.30	11.30	17.70
Zr	7.51	6.56	5.12	4.61	4.20	4.88	5.02	8.22	5.14	7.15
Nb	0.00	0.09	0.00	0.00	0.00	0.00	0.00	0.00	0.00	0.00
Mo	0.01	0.02	0.01	0.01	0.02	0.01	0.02	0.02	0.01	0.03
Ba	0.03	4.90	bdl	0.05	0.40	0.04	0.13	0.06	0.05	0.54
La	0.39	0.37	0.26	0.25	0.26	0.27	0.26	0.49	0.25	0.54
Ce	1.70	1.61	1.21	1.13	1.08	1.21	1.19	2.08	1.22	2.09
Pr	0.48	0.41	0.32	0.32	0.26	0.30	0.35	0.53	0.32	0.49
Nd	3.43	2.69	2.35	2.08	1.80	2.02	2.44	3.74	2.09	3.10
Sm	1.60	1.11	1.13	1.01	0.93	1.13	1.08	2.05	1.02	1.46
Eu	0.54	0.44	0.38	0.39	0.31	0.37	0.41	0.56	0.40	0.53
Gd	2.85	1.91	1.85	1.73	1.43	1.55	1.87	2.93	1.73	2.41
Tb	0.49	0.32	0.33	0.27	0.25	0.28	0.31	0.57	0.29	0.43
Dy	4.50	2.86	2.65	2.05	1.90	2.16	2.32	4.10	2.02	3.06
Ho	0.70	0.45	0.45	0.43	0.38	0.45	0.48	0.84	0.45	0.68
Er	1.99	1.48	1.34	1.36	1.12	1.28	1.52	2.38	1.33	2.02
Tm	0.31	0.21	0.20	0.20	0.15	0.18	0.21	0.34	0.18	0.25
Yb	1.80	1.21	1.13	1.16	1.07	1.25	1.21	2.23	1.11	1.63
Lu	0.26	0.17	0.16	0.16	0.15	0.19	0.18	0.36	0.17	0.27
Hf	0.39	0.32	0.26	0.25	0.22	0.25	0.28	0.42	0.27	0.37
Ta	bdl	0.00	0.00	bdl	bdl	bdl	bdl	0.00	bdl	bdl
Pb				0.01	0.02	0.04	0.03	0.05	0.01	0.15
Th	0.01	0.01	0.00	0.00	0.01	0.04	bdl	0.01	0.01	0.03
U	0.02	0.01	0.00	0.00	0.01	0.01	0.00	0.00	0.01	0.00

TAN1213 10-8	Pyroxene-02ALA	Pyroxene-02BLA	Pyroxene-04LA	Pyroxene-05LA	Pyroxene-06LA	Pyroxene-08LA	Pyroxene-09LA	Pyroxene-10LA
Li	1.88			1.68	2.11	2.08	2.62	2.47
Sc	139.00	136.00	132.00	121.00	123.00	136.00	119.00	129.00
Ti	2450.00	2800.00	2480.00	2270.00	2450.00	2710.00	2340.00	2350.00
V	400.00	459.00	391.00	419.00	428.00	484.00	403.00	379.00
Cr	673.00	59.60	488.00	48.20	76.50	5.47	136.00	127.00
Co	48.60	53.20	49.60	52.00	52.00	55.60	49.30	52.90
Ni	73.90	48.50	69.20	44.80	50.40	35.10	52.00	56.60
Cu	2.36	4.04	4.59	3.86	4.85	4.72	5.09	4.14
Zn	42.30	53.70	43.40	48.40	46.50	58.90	42.00	40.40
Ga	4.43	4.64	4.32	4.32	4.04	4.50	4.10	4.03
Rb	0.06	bdl	bdl	0.04	bdl	0.05	bdl	bdl
Sr86	18.20			15.70	17.30	15.70	16.80	15.90
Sr88		19.40	18.50					
Y	13.10	13.70	12.10	12.90	12.10	17.00	12.20	11.90
Zr	6.88	5.53	5.46	5.24	4.92	6.57	5.28	5.27
Nb	0.01	0.00	0.00	0.00	bdl	0.00	0.00	0.00
Mo	0.02	0.02	0.01	0.02	0.01	0.01	0.02	0.01
Ba	1.42	bdl	0.09	0.12	bdl	0.02	0.02	0.09
La	0.33	0.30	0.27	0.33	0.27	0.35	0.28	0.26
Ce	1.37	1.32	1.17	1.29	1.27	1.63	1.17	1.22
Pr	0.38	0.38	0.31	0.33	0.32	0.42	0.32	0.34
Nd	2.69	2.70	2.46	2.20	2.45	3.05	2.24	2.17
Sm	1.31	1.25	1.12	1.14	1.16	1.52	1.17	1.02
Eu	0.45	0.46	0.40	0.40	0.39	0.51	0.39	0.42
Gd	2.03	2.18	1.63	1.78	1.76	2.22	1.76	1.75
Tb	0.38	0.41	0.35	0.33	0.34	0.43	0.34	0.32
Dy	2.44	2.48	2.38	2.31	2.27	3.07	2.26	2.06
Ho	0.51	0.50	0.50	0.48	0.47	0.64	0.48	0.47
Er	1.50	1.54	1.35	1.42	1.30	1.84	1.31	1.36
Tm	0.22	0.24	0.20	0.19	0.20	0.26	0.19	0.18
Yb	1.48	1.38	1.25	1.32	1.27	1.62	1.21	1.09
Lu	0.21	0.21	0.18	0.19	0.17	0.25	0.18	0.17
Hf	0.38	0.31	0.28	0.26	0.23	0.30	0.29	0.26
Ta	0.00	bdl	bdl	0.00	bdl	bdl	bdl	0.00
Pb	0.03	0.02	0.03	0.02	0.01	0.02	0.02	0.02
Th	0.01	bdl	bdl	0.00	bdl	bdl	0.00	bdl
U	0.00	bdl	bdl	0.00	bdl	0.00	bdl	bdl

TAN1213 10-10	Pyroxene-01LA	Pyroxene-04ALA	Pyroxene-04BLA	Pyroxene-07LA
Li		1.93	2.11	6.07
Sc	129.00	99.30	112.00	143.00
Ti				
V	338.00	208.00	198.00	508.00
Cr	159.00	832.00	740.00	2.43
Co	52.60	39.40	37.70	61.20
Ni	57.80	99.40	99.20	35.50
Cu	0.85	2.35	2.36	1.93
Zn	39.50	18.90	16.10	66.80
Ga	4.29	3.44	3.35	4.29
Rb	bdl	bdl	bdl	bdl
Sr86		16.80	18.80	15.30
Sr88	23.30			
Y	11.20	6.13	5.12	16.30
Zr	4.96	2.80	3.16	6.21
Nb	bdl	0.00	0.00	0.00
Mo	0.02	0.02	0.03	0.01
Ba	0.79	bdl	bdl	0.05
La	0.24	0.11	0.13	0.31
Ce	1.20	0.60	0.62	1.50
Pr	0.30	0.15	0.17	0.44
Nd	2.14	1.13	1.18	3.21
Sm	0.95	0.57	0.52	1.54
Eu	0.44	0.22	0.23	0.49
Gd	1.61	0.93	0.85	2.45
Tb	0.27	0.15	0.15	0.47
Dy	1.96	1.10	0.92	3.06
Ho	0.43	0.24	0.20	0.63
Er	1.31	0.64	0.59	1.91
Tm	0.18	0.08	0.08	0.29
Yb	1.04	0.54	0.48	1.80
Lu	0.16	0.08	0.07	0.25
Hf	0.28	0.16	0.15	0.33
Ta	bdl	bdl	bdl	bdl
Pb	0.02	bdl	0.01	0.02
Th	bdl	bdl	0.00	0.00
U	bdl	bdl	bdl	0.00

bdl=below detection limit. Sr86 was selected for large spot sizes and Sr88 was selected for small spot sizes due to the offset% from reference values of BCR-2G

Appendix 3 Analytical Standards and Uncertainties

Table A-8: Summary of EPMA data acquired for international standard Plagioclase NMNH115900, showing precision and accuracy of plagioclase major element analysis.

Plagioclase NMNH 115900	Mean (n=18)	Min	Max	2 SD	2 SD(%)	Reference	Offset(%)
SiO2	51.30	50.60	51.70	0.34	0.66	51.30	0
TiO2	0.03	0.02	0.05	0.01	30	0.05	-43
Al2O3	30.80	30.50	31.40	0.27	0.89	30.90	0
FeO	0.47	0.42	0.54	0.03	6.99	0.46	2
MnO	0.01	0.00	0.03	0.01	102	n/d	n/d
MgO	0.14	0.13	0.15	0.01	5.40	0.14	-1
CaO	13.60	13.40	14.20	0.26	1.93	13.60	0
Na2O	3.57	3.24	3.72	0.13	3.61	3.45	3
K2O	0.12	0.10	0.14	0.01	7.65	0.18	-32
Cr2O3	0.00	0.00	0.02	0.01	164	n/d	n/d
Total	100.00	99.60	100.00	0.26	0.26	100.00	0

Reference values are from Jarosweich et al. (1980).

Table A-9: Summary of EPMA data acquired for international mineral standard Kakanui Augite, showing the precision and accuracy of clinopyroxene major element analysis.

A)

Kakanui Augite	Mean (n=6)	Min	Max	2 SD	2 SD(%)	Reference	Offset(%)
SiO2	50.90	50.80	51.00	0.19	0.38	50.70	0.27
TiO2	0.77	0.75	0.78	0.02	2.64	0.74	4.14
Al2O3	8.72	8.66	8.79	0.09	0.98	8.73	-0.13
FeO	6.25	5.93	6.42	0.40	6.36	6.34	-1.48
MnO	0.14	0.11	0.15	0.03	23.10	0.13	7.31
MgO	16.70	16.60	16.80	0.13	0.80	16.70	0.18
CaO	15.90	15.90	16.00	0.11	0.67	15.80	0.74
Na2O	1.28	1.24	1.31	0.05	4.06	1.27	0.43
K2O	0.00	0.00	0.01	0.01	310	n/d	n/d
Cr2O3	0.15	0.14	0.17	0.03	17.70	0.15	2.11
Total	101.00	100.00	101.00	0.65	0.65	100.00	0.40

B)

Kakanui Augite	Mean (n=6)	Min	Max	2 SD	2 SD(%)	Reference	Offset(%)
SiO2	50.90	50.70	51.00	0.14	0.27	50.70	0.27
TiO2	0.74	0.69	0.76	0.03	3.66	0.74	-0.50
Al2O3	8.80	8.73	8.85	0.04	0.47	8.73	0.85
FeO	6.44	6.26	6.62	0.16	2.45	6.34	1.64
MnO	0.13	0.11	0.14	0.01	8.83	0.13	0.39
MgO	16.70	16.50	16.70	0.06	0.38	16.70	0.14
CaO	15.90	15.80	16.00	0.04	0.27	15.80	0.62
Na2O	1.29	1.25	1.35	0.04	2.73	1.27	1.31
K2O	0.01	0.00	0.02	0.01	88	n/d	n/d
Cr2O3	0.16	0.15	0.18	0.01	6.14	0.15	6.78
Total	101.00	101.00	101.00	0.21	0.21	100.00	0.64

Reference values are from Jarosewich et al. (1980). B) Standards for crystals selected for LA-ICP-MS analysis

Table A-10: Summary of EPMA data acquired for international standard Hornblende, showing the precision and accuracy of amphibole major element analysis.

Hornblende	Mean (n=4)	Min	Max	2 SD	2 SD (%)	Reference	%Offset
SiO2	39.60	39.40	39.60	0.19	0.48	39.50	0.06
TiO2	3.26	3.14	3.41	0.25	7.58	2.88	13.30
Al2O3	10.10	9.97	10.20	0.16	1.61	10.00	0.51
FeO	26.10	25.50	26.60	0.93	3.55	26.20	-0.37
MnO	0.44	0.42	0.44	0.02	4.06	0.41	6.16
MgO	4.33	4.28	4.37	0.07	1.59	4.38	-1.14
CaO	10.80	10.70	10.80	0.10	0.93	10.80	-0.33
Na2O	2.03	1.98	2.07	0.09	4.34	2.02	0.25
K2O	1.46	1.45	1.48	0.03	2.01	1.47	-0.53
Cr2O3	0.00	0.00	0.01	0.01	232.00	n/d	n/d
Total	97.90	97.50	98.40	0.77	0.79	97.80	0.12

Reference values are from Ingamells (1980).

Table A-12: Summary of EPMA data acquired for international standard Engels Amphibole, showing the precision and accuracy of amphibole major element analysis.

Engels Amphibole	Mean (n=4)	Min	Max	2 SD	2SD (%)	Reference	%Offset
SiO2	41.90	41.60	42.10	0.56	1.34	42.10	-0.62
TiO2	0.97	0.95	0.99	0.04	4.31	0.94	2.85
Al2O3	11.30	11.10	11.50	0.39	3.46	12.10	-6.34
FeO	19.90	19.80	20.00	0.19	0.97	19.10	4.50
MnO	0.61	0.59	0.63	0.04	6.74	0.63	-2.54
MgO	8.75	8.61	8.83	0.21	2.34	8.67	0.92
CaO	11.30	11.20	11.40	0.18	1.58	11.60	-1.96
Na2O	1.40	1.36	1.46	0.10	7.19	1.63	-14.00
K2O	0.87	0.83	0.92	0.09	10.20	0.91	-4.45
Cr2O3	0.01	0.00	0.03	0.02	216.00	n/d	n/d
Total	97.10	96.70	97.30	0.55	0.56	97.60	-0.58

Reference values are from Ingamells (1980).

Table A-11: Summary of EPMA data acquired for international standard Magnetite NMNH115900, showing the precision and accuracy of magnetite major element analysis.

Magnetite NMNH 115900	Mean (n=14)	Min	Max	2 SD	2 SD(%)	Reference	Offset (%)
TiO2	0.13	0.07	0.17	0.03	20.30	0.16	-19.90
Al2O3	0.01	0.00	0.03	0.01	64.50	n/d	n/d
FeO	90.40	87.60	91.90	1.03	1.14	90.90	-0.63
MnO	0.01	0.01	0.03	0.01	44.10	0.01	47.10
MgO	0.08	0.07	0.10	0.01	10.40	0.05	64.10
Cr2O3	0.20	0.14	0.26	0.04	20.80	0.25	-19.40
V2O3	0.23	0.20	0.25	0.01	5.73	n/d	n/d
Total	91.00	88.30	92.50	1.01	1.11	91.40	-0.40

Reference values are from Jarosewich et al. (1980).

Table A-13: List of measured and preferred values for trace element abundances of glass standard NIST612.

NIST612 (n=36)	**Small Spots 30 µm**						
	Average	Min	Max	2SD	2SD%	Reference	Offset
Li	36.4	31.7	43	5.34	14.7	40.2	-10
Sc	42.2	37.9	50.6	6.97	16.5	39.9	6
Ti	47.5	35.7	62	11.9	25.2	44	8
V	36.5	32.6	41.6	4.94	13.5	38.8	-6
Cr	35.4	32.2	39	4.11	11.6	36.4	-3
Mn	41.5	34.9	45.7	4.33	10.4	38.7	7
Co	32.1	30.6	34	1.77	5.51	35.5	-10
Ni	33.9	30.9	38.4	4.45	13.1	38.8	-13
Cu	35.8	31.3	41.2	5.81	16.2	37.8	-5
Zn	28.1	23.8	31.7	3.84	13.7	39.1	-28
Ga	35.4	33.6	36.7	1.54	4.34	36.9	-4
Rb	28.6	25.4	32.8	4.11	14.4	31.4	-9
Sr	77.4	68.2	86.1	11.4	14.7	78.4	-1
Y	43.8	41.7	46	2.07	4.74	38.3	14
Zr	41.1	36.8	49.4	6.11	14.9	37.9	9
Nb	39.6	35.2	45.1	5.73	14.5	38.9	2
Mo	32.6	31.9	33.3	0.779	2.39	37.4	-13
Cs	22	12.1	38.8	23	105	42.7	-49
Ba	38.3	34.1	42.2	5.09	13.3	39.3	-3
La	36.9	34.3	38.9	2.53	6.85	36	2
Ce	39.6	38.1	41.8	1.92	4.84	38.4	3
Pr	39.5	35.4	45.9	4.97	12.6	37.9	4
Nd	36.2	32.2	42.8	5.64	15.6	35.5	2
Sm	38.1	34.2	42.3	4.66	12.2	37.7	1
Eu	36.6	34.6	40.6	2.99	8.17	35.6	3
Gd	39	34.3	46.6	6.17	15.8	37.3	5
Tb	39.1	34.6	44.1	5.68	14.5	37.6	4
Dy	37.5	34.9	40.1	3.33	8.9	35.5	6
Ho	40.5	39.2	42.2	1.41	3.47	38.3	6
Er	40.5	36.8	47.1	4.83	11.9	38	6
Tm	40.3	35.6	47.6	6.21	15.4	36.8	9
Yb	40.2	36.6	44.1	5.04	12.5	39.2	3
Lu	39	37	40.8	2.04	5.22	37	5
Hf	38.2	35.9	41.9	2.87	7.51	36.7	4
Ta	40	35.8	47.5	5.5	13.7	37.6	7
W	36.3	31.9	43.3	5.44	15	38	-4
Pb	34.9	32.3	38.5	3.46	9.91	38.6	-10
Th	39.7	38.9	41	1.1	2.77	37.8	5
U	34.2	31.7	39.2	3.7	10.8	37.4	-8

NIST612 (n=36)	Large Spots 50 µm						
	Average	min	max	2SD	2SD%	Reference	Offset
Li	39.8	35.6	45.8	6.28	15.8	40.2	-1
Sc	43.8	38.9	49.2	6.07	13.9	39.9	10
Ti	49.2	42.2	57.3	8.28	16.8	44	12
V	38.3	33.2	43.1	5.77	15.1	38.8	-1
Cr	31.5	3.41	41.1	21	66.5	36.4	-13
Mn	35.9	7.75	41.7	18.7	52.1	38.7	-7
Co	33	32	35	1.65	5.01	35.5	-7
Ni	36.5	32.9	41.3	5.13	14.1	38.8	-6
Cu	38.4	33.7	42.3	5.44	14.2	37.8	2
Zn	31.4	27.8	36.2	4.16	13.3	39.1	-20
Ga	35.9	33.5	37.1	1.39	3.87	36.9	-3
Rb	31.3	28	35.9	4.96	15.8	31.4	0
Sr	79	68.7	87.9	11.9	15.1	78.4	1
Y	41.9	30.8	45	7.1	16.9	38.3	9
Zr	42.2	39.3	46.4	3.49	8.28	37.9	11
Nb	40.9	35.6	44.8	6.02	14.7	38.9	5
Mo	33.2	28.7	36.2	3.65	11	37.4	-11
Mo	32.9	31.3	34.1	1.12	3.4	37.4	-12
Cs	39.5	35	44.5	4.92	12.5	42.7	-8
Ba	39.2	34.7	43.2	5.03	12.8	39.3	0
La	33.4	9.39	38.3	15.6	46.8	36	-7
Ce	39.8	38.6	42.8	1.95	4.89	38.4	4
Pr	41.9	37.4	48.2	6.01	14.3	37.9	11
Nd	38.5	33.1	42.5	5.98	15.5	35.5	8
Sm	39.6	35.2	43.4	4.34	11	37.7	5
Eu	37.1	34.7	38.2	1.39	3.73	35.6	4
Gd	41.1	36.9	47.1	6.47	15.7	37.3	10
Tb	41.6	34.3	48	7.52	18.1	37.6	11
Dy	33.7	2.87	42.4	22.8	67.7	35.5	-5
Ho	40.6	38.9	42.8	1.58	3.88	38.3	6
Er	41.8	37.2	47.6	5.78	13.8	38	10
Tm	42.6	37	49.9	7.32	17.2	36.8	16
Yb	41.6	36.5	44.5	4.26	10.2	39.2	6
Lu	40	37.4	41.2	1.56	3.92	37	8
Hf	38.3	35.3	42.1	3.18	8.3	36.7	4
Ta	42.6	37.8	49.2	6.57	15.4	37.6	13
W	37.8	32.5	42	5.28	14	38	-1
Pb	31.2	3.58	38.1	20.2	64.6	38.6	-19
Th	39.6	38.6	40.7	1.02	2.58	37.8	5
U	35.9	32.2	41.1	4.54	12.6	37.4	-4

Reference values were obtained from Jochum and Enzweiler (2013).